

Computer simulation of the growth of ice structures under astronomical conditions

James A. Miller

Department of Physics, University of Strathclyde

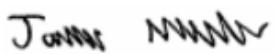
2016

A thesis submitted to the Department of Physics, University of Strathclyde,
for the qualification of Master of Philosophy



This thesis is the result of the author's original research. It has been composed by the author and has not been previously submitted for examination which has led to the award of a degree.

The copyright of this thesis belongs to the author under the terms of the United Kingdom Copyright Acts as qualified by University of Strathclyde Regulation 3.50. Due acknowledgement must always be made of the use of any material contained in, or derived from, this thesis.

Signed: 

Date: 10-02-2017

Abstract

As part of the diffuse interstellar medium, water molecules contribute extensively to the chemical properties of astronomical environments, both in the gaseous and adsorbed state. Along with carbon monoxide, water is expected to deposit on silicate dust grains in space, forming icy films which may provide a substrate for exotic, low-temperature surface chemistry and act as a reservoir for further deposited species. On account of the nature of its aggregation – vapour deposition over millions of years in environments as cold as 10K – the water ice is not expected to form a crystalline structure as under terrestrial conditions, but rather a metastable glass: ‘amorphous solid water’, ASW.

In this work we used molecular dynamics to model the deposition of water onto cold substrates of both silica (representing a bare grain surface) and cubic crystalline ice (representing an ice-covered grain migrating back from warmer regions), with the intention of understanding film growth and properties in circumstellar environments. The water was injected at different energies, onto substrates of different temperatures, to determine what effect the thermal conditions of the water / substrate interaction had on the ice films formed.

Significant differences were observed between those molecules deposited under the coldest (10K deposition on 10K substrate) and warmest (300K deposition on 130K substrate) regimes. Cold aggregation, as would be expected in the core of a dark molecular cloud, produced tall, filamentous structures with cavities. Meanwhile, warmer conditions produced dense, comparatively flat films.

Contents

Chapter 1 – Introduction	6
1.1 Overview	6
1.2 The interstellar medium	7
1.3 General reactions in the ISM	12
1.4 Solid state chemistry in a cloud	15
1.5 The crystalline structures of water	17
1.6 The amorphous structures of water	19
1.7 Mixed ice chemistry and water observation	26
1.8 Current understanding of astronomical water	36
1.9 Summary	37
Chapter 2 – Molecular dynamics	39
2.1 Overview	39
2.2 The basic premise of simulation	40
2.3 Short-range interparticle forces	41
2.4 Temperature control	42
2.5 Periodic boundary conditions and the minimum image convention	45
2.6 Long-range limitations of the minimum image convention	47
2.7 Water in simulation	48
2.8 TIP4P water models	53
2.9 Previous work in ASW simulation	54
2.10 Summary	56
Chapter 3 – Simulation methodology	57
3.1 Overview	57
3.2 Force limits	57
3.3 Choosing a water model	59
3.4 Creating the silica substrate	62
3.5 Creating the water substrate	64
3.6 Creating the incident water	68
3.7 Combining for deposition	70
3.8 Summary	73
Chapter 4 – Results	75
4.1 Overview	75
4.2 Methodologies and averages for static results	76
4.3 Methodologies and averages for dynamic results	81
4.4 Height and growth modes	84
4.5 Surface relaxation and occlusion	95
4.6 Surface hydrogen bonding	98
4.7 Volume and density	104

4.8	Deposition failures	114
4.9	Astrochemical implications	117
Chapter 5 – Conclusions							119
5.1	Overview	119
5.2	Further work	120
References							122
Appendices							130
A	Static structure results	130
B	Dynamic structure results	135

Chapter 1 - Introduction

1.1 – Overview

Water is believed to be the most abundant solid molecule in the universe ^[1]. Terrestrial water in lakes and oceans covers 71% of the Earth's surface and is estimated contribute 1.36 billion cubic kilometers to the planet's volume. Over half the mass of a human body is H₂O, and access to the chemical is vital for all known forms of life ^[2]. Knowing where water originates in the universe, therefore, is an integral part of understanding where and how life can arise. But water's ubiquity also means that its physical properties in space are vital to the study of star and planet formation. Hydrogen and oxygen are the first and third most common chemical elements in the universe (the second being helium, which does not form neutral molecules under interstellar conditions), and with an exothermic ΔH_f° -285 kJmol⁻¹^[3], their combination is detected throughout the cosmos as a fundamental component of both hot and cold interstellar clouds. ^{[4][5]}

Observational evidence from telescopic investigations indicates that water ice in space is not found in a crystalline form which we would be familiar with on Earth, but rather in a disordered, amorphous state. This is corroborated by laboratory experiments, depositing water in molecular quantities to form thin, ~100 monolayer films as we expect to find in space ^[6]. Computer simulations of water under astronomical conditions also inform us on the nature of this material.

In this thesis, Molecular Dynamics simulation techniques are used to study the structure and bonding of amorphous solid water formed by vapour deposition. The key aims of the work are to bring us a better understanding of the small-scale structure of this astronomical amorphous ice, and to determine how different surfaces and temperatures may affect the ices' growth mechanism.

The scope of this introductory chapter is to provide background and wider perspective to the role of water in astronomy, and the nature of water ice under these extreme interstellar conditions.

1.2 – The Interstellar Medium

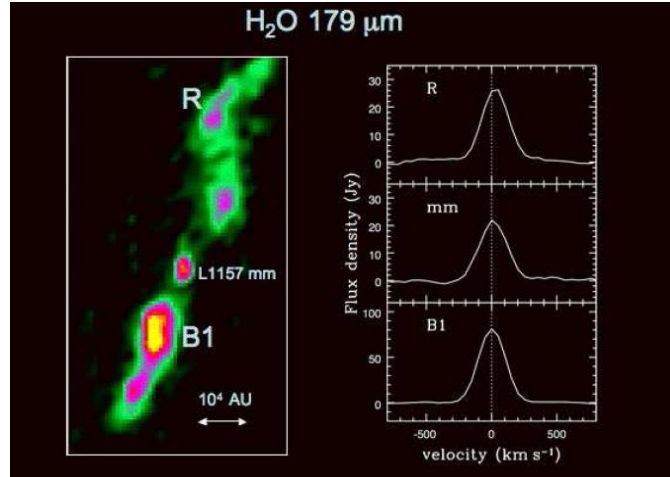


Figure 1.1: Herschel PACS data showing abundant gas-phase water around protostar L1157^[7], where shock fronts have sublimed solid ices. Pink and yellow areas represent the greatest concentration of water, around star-forming regions. Reproduced from van Dishoeck et al^[8].

Most of the baryonic matter in the universe as a whole is found within the interstellar medium (ISM): an extremely low-density, turbulent mixture of ions, gas, dust, supported by electric and magnetic fields. Indeed, the ISM is typically several orders of magnitude less dense than the best terrestrial vacuum chambers; with an average particle density of 10^6 m^{-3} , compared to $2.0 \times 10^{25} \text{ m}^{-3}$ for the air at sea level on Earth, making the astronomical ‘gas phase’ 20 quadrillion times more rarefied than a terrestrial gas phase. Within the ISM, about 99% of the mass is gas, while just 1% exists in the solid phase as dust and ice^[9]. The gas itself is composed overwhelmingly of atomic and molecular hydrogen (89%), plus 9% helium and 2% heavier gasses.^[10]



Figure 1.2: Molecular clouds in NGC281^[11]. The red areas represent “H1” regions; optically transparent volumes of space illuminated by the H- α , the first line of the Balmer series (radiation emitted when an electron de-excites from $n=3$ to $n=2$). The dark regions are clouds where the density of micron-sized dust grains is higher.

The density of the ISM is non-uniform; regions may become many orders of magnitude more diffuse or more dense than the average. Gravitational attraction or shock compression can encourage collapse to higher densities, while gas pressure in turn resists the contraction. Over millions of years, slow collapse in a clumpy region of the ISM forms visibly opaque objects known as dense molecular clouds (see *Figure 1.2*). Their opacity comes from the density of micron-sized dust grains within them, which is sufficient to scatter visible wavelengths. The clouds are also self-shielding against ultraviolet radiation, which is largely absorbed by the C \equiv O bond in carbon monoxide. Photodissociation region (PDR) edges on the outer surface of the cloud sees ultraviolet radiation break H₂ up into hot H^{*} radicals, while polycyclic aromatic hydrocarbon (PAH) species emit high energy photoelectrons to further heat the PDR gasses up to 100-300K. Conversely, the shielded cores are some of the coldest objects in the observable universe, reaching temperatures below 10K^[12]. Water ice cannot survive in the hot conditions outside the clouds, but inside, the higher densities and lower pressures are conducive to its formation.

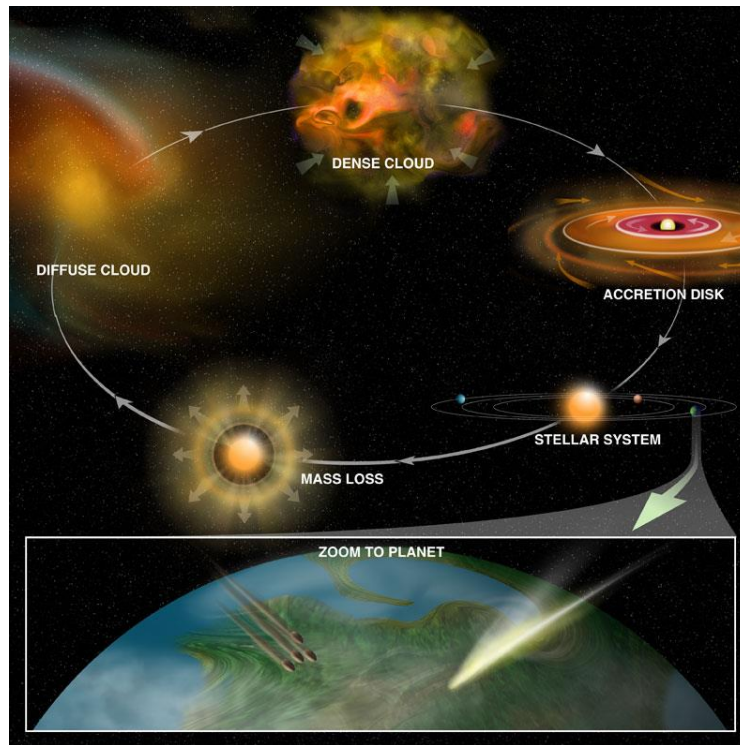


Figure 1.3: The life cycle of a star. Formed in the contraction of a diffuse, cold cloud, stars acquire an accretion disk which may give rise to a planetary system. As the star gets older and its supply of fusible nuclei diminishes, much of its mass is returned to the ISM, where it may form new star-forming clouds.^[13]

Gravitational contraction in these cold cores – known as Kelvin-Helmholtz collapse – may eventually lead to the formation of stars and protoplanetary systems. In a dense molecular core, water is expected to form first via chemical vapour deposition^[14] of oxygen and hydrogen radicals on dust grain surfaces (see also *Section 1.4, Equations 1.6 – 1.7*). As cloud collapse progresses, the core remains very cold, and water is expected to remain where it forms: on the grains, not diffusing back and forth between grain and gas phase. However, as the cloud continues to condense, stars begin to form. Material close to a young star can be heated by several processes: direct infra-red penetration from the star, bow shocks from polar jets, or ultraviolet irradiation at the edges of protostellar envelopes (see *Figure 1.4*).

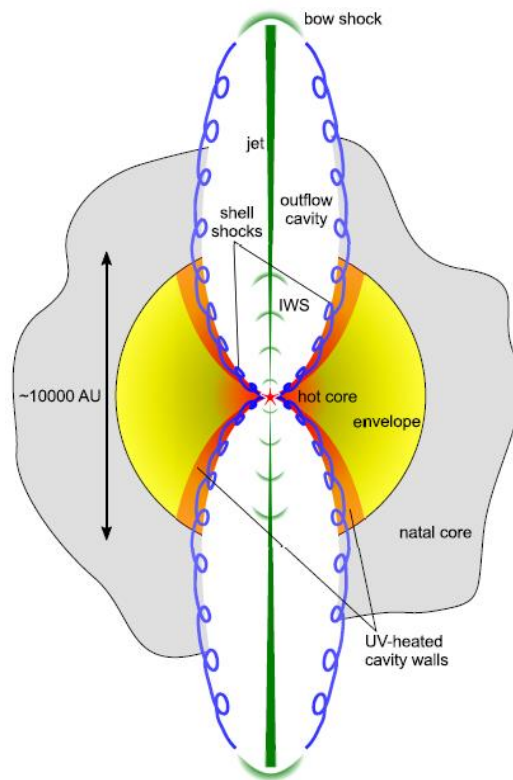


Figure 1.4: Interaction of a young star with its immediate environment. The mechanism which produces polar jets along stars' axis of rotation remains uncertain, but the hot expelled plasma induces shock fronts where it collides with the surrounding gas.

The rising temperature enables adsorbed water molecules to evaporate from the grains on which they initially formed ^[15]. If gas-phase water subsequently cycles back into a colder part of the cloud, it can re-condense – now by physical rather than chemical vapour deposition, which raises the possibility of water depositing on either bare grains, or onto partially-saturated grains already supporting ice. As the ISM evolves, and material is cycled back and forth between warm circumstellar environments and cold cloud regions over billions of years (see *Figure 1.3*), it is likely that ices formed by re-deposition in this way will come to dominate their local environment, which makes study of physically deposited ices particularly relevant to considerations of the thermal and chemical regulation of star-forming regions. Astronomical water of this type may also eventually find itself incorporated into a planet via cometary bombardment, which makes it relevant to the genesis of early life.

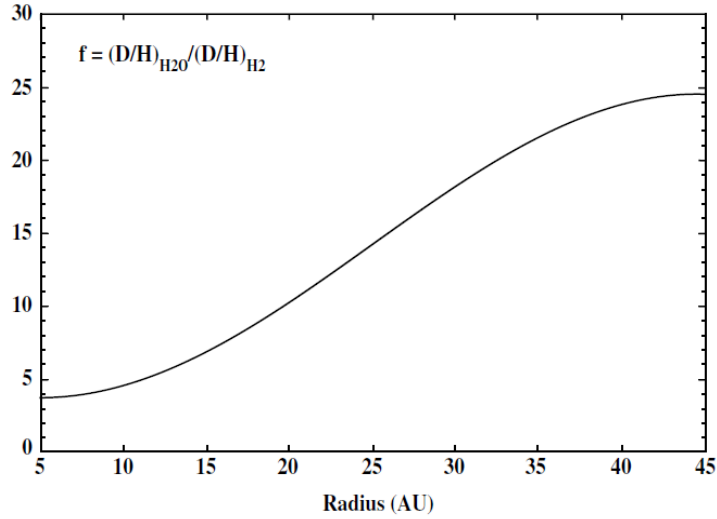


Figure 1.5: Deuterium enrichment in water against the baseline H_2/HD ratio as a function of distance from a star. Water ices formed further from the center of a stellar envelope are expected to incorporate more D. Reproduced from Horner et al. ^[16]

We can estimate the temperature at which an ice formed by deuterium fractionation ^[17]. The H/D ratio in interstellar ices can function as a kind of “cosmothermometer” to indicate the thermal history of a particular component. The deuteration ratio varies somewhat in different interstellar clouds, ranging from 3 to 15ppm. But if we know this baseline of the local environment, we can gauge whether an observed ice was formed in cold or warmer regions because of the reaction:



At low temperatures the equilibrium constant of this reaction favours deuteration of water ^[16]. Once water freezes out of the gas phase, its deuterium proportion is largely “locked in”, so ice deposited in very cold regions of a cloud tends to have higher deuterium content than other ices which have formed at higher temperatures. It is by using this diagnostic tool that it has been determined the Solar comets Hyakutake, Halley, and Hale-Bopp were formed in the Oort cloud or Kuiper Belt, rather than closer to the sun. ^{[18][117]}

1.3 – General Reactions in the ISM

More than 140 molecules have been detected in interstellar space or in circumstellar environments, most of them identified from their rotational emission spectra in “hot cores” – regions of star formation ^[19]. Because it is impractical to obtain samples of material from cold clouds in interstellar space – preventing experimentation *in situ* – we supplement remote sensing data from telescopic observation with *in vivo* and *in silico* experiments approximating the conditions of the interstellar medium, in order to gain an understanding of the chemical processes which can occur therein. For these, astrochemical models are used, which describe the low-temperature interactions of the low-mass species expected to be present. Such models are not atomistic Molecular Dynamics (see *Chapter 2*), but rather “chemical networks”: vast arrays of interdependent first-order rate equations, which can describe the abundances of thousands of chemicals, as well as photon and electron densities, and the interactions and reactions between them. Such networks typically start with atomic species combining into molecules, which then associate and react to form more complex species. Solving the rate equations numerically allows us to track the time-dependent composition of the ISM, although they require an encyclopedic understanding of the energies of reaction between each species. These values are often not known experimentally, and must be estimated from theoretical chemistry^[20].

Figure 1.6 shows an example of the evolving chemical compositions calculated for a fast-warming protostellar cloud. These chemical inventory methods work well in the gas phase, where an arbitrarily large cell raises the abundance of all species to a sufficient size that stochastic effects are notionally eliminated. However, coupling this to adsorbed-phase models of fast reactions on limited surface area grains can be problematic, as stochastic effects do come into play, invalidating simple “deterministic” rate equations. ^{[21] [22]}

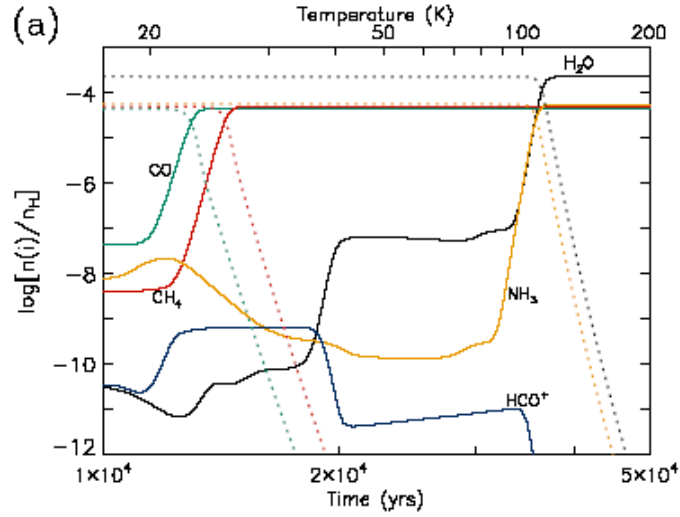


Figure 1.6: Chemical network tracking of species abundance as a cold cloud contracts and heats, plotted as a logarithmic function of the ratios of species number density relative to H number density. As mentioned in Section 1.2, water is the most abundant molecule at the end of the study, with CO , CH_4 , and NH_3 also being formed in abundance. Reproduced from [23].

The extremely cold conditions of the ISM mean that only certain gas phase reactions can be of astrochemical relevance (especially in dense cores). The reactions must be exothermic (as there is nowhere to take the energy *out* of for an endothermic process), and they must have essentially no activation barrier. There are only 5 relevant classes of reaction which fit these criteria: ^[10]

- Cation - molecule: $A^+ + B \rightarrow C^+ + D$ (1.2)
- Radiative association: $A + B \rightarrow C + h\nu$ (1.3)
- Dissociative recombination: $A^+ + e^- \rightarrow C + D$ (1.4)
- Radical recombination: $A\cdot + B\cdot \rightarrow C$ (1.5)
- Radical addition: $A\cdot + B \rightarrow C$ (1.6)

Cation – molecule: Positive ions in the ISM are generally generated by cosmic-ray bombardment: high energy nuclei which are capable of penetrating even into dense cores. The ionisation rate due to cosmic rays is expressed by the parameter ζ , which technically refers to the sum rate of H_2 heterolytic *and* homolytic fission by cosmic rays, with a typical value of 10^{-17} s^{-1} . Predictably, the dominant species produced by cosmic rays is H_2^+ , which swiftly goes on to react $H_2^+ + H_2 \rightarrow H_3^+ + H$, with H_3^+

being an important precursor for a host of subsequent reactions. Amongst other cation – molecule reactions, polar ions tend to react faster than apolar ones, and their rate constants have an inverse temperature dependence.

Radiative association: A generally inefficient pathway which proceeds only if there are no other exothermic options available. Radiative association occurs when two reactants collide and form a temporary complex. Usually, the complex will dissociate and return the reactants, but on occasion it may stabilise itself by the release of a photon and thereby allow the complex to persist. An astrochemically relevant reaction of this type is $\text{CH}_3^+ + \text{H}_2 \rightarrow \text{CH}_5^+ + h\nu$, which stabilises in this way roughly one out of every ten thousand collisions ^[24].

Dissociative recombination: Where the combination of a cation and an electron produces a host of neutral fragments. These tend to have rate constants between 100 and 1000 times larger than cation – molecule reactions, and are best studied in the lab using storage rings originally developed for nuclear physics experiments. The products are often unexpected; the well-known interstellar cation HN_2^+ dissociates mainly as $\text{HN}_2^+ + \text{e}^- \rightarrow \text{HN} + \text{N}$, with only 36% following the more chemically intuitive $\text{HN}_2^+ + \text{e}^- \rightarrow \text{N}_2 + \text{H}$ ^[25]. The concentration of N_2 is difficult to measure directly because, like hydrogen, it is an apolar homonuclear diatomic with no rotational spectrum, so knowledge of its abundance cannot be used to inform models of its astrochemical formation rates.

This is an important result, both for nitrogen production in the eventual diversification of organic chemistry, and because HN_2^+ is used as a tracer species to infer cloud temperature in particularly cold regions (see *Section 1.7*).

Radical reactions: Radicals can be produced in space by cosmic ray bombardment, and highly reactive ones can persist even on the surface of dust grains because there is insufficient energy for them to diffuse and find a reactant partner. But, when they *do* collide, reaction is fast even at low T. Examples include $\text{O} + \text{OH} \rightarrow \text{O}_2 + \text{H}$ and $\text{CN} + \text{C}_2\text{H}_2 \rightarrow \text{HCCCN} + \text{H}$. ^[26]

As a protostellar cloud heats up, it may be necessary to incorporate other reactions which do not adhere to the rigorous “exothermic-only” criteria of the cold cloud. The reaction $C^+ + H_2 \rightarrow CH^+ + H$, weakly endothermic at 0.4eV, is thought to account for the otherwise inexplicable abundance of CH^+ in hot cores ^[26].

Reactions 1.2 – 1.6 are all two-body reactions, because in the rarefied conditions of the ISM the probability of a three-body collision is negligible. However, many reactions which have been inferred as necessary to the ISM on account of observed molecular species and their abundances do require a third particle to carry away energy, and this is why surface-mediated reactions are vital to understanding the cloud chemistry, in spite of their low concentration.

1.4 – Solid state chemistry in a cloud

The fundamental astrochemical reaction of $H + H \rightarrow H_2$, producing the most common molecule of the ISM, dihydrogen, occurs not in the gas phase, but as surface chemistry on a solid substrate. The abundance of H_2 in interstellar space cannot be explained simply by long-timescale gas-phase combination of atomic hydrogen, because this reaction is spin-forbidden and would require three-body collisions to occur. Accordingly, H_2 formation is presumed to proceed on the surface of interstellar dust grains. These dust grains are non-volatile carbonaceous or silicate materials, most frequently amorphous olivine $(Fe,Mg)_2SiO_4$. Experiments have shown ^{[27][28]} that dihydrogen formation efficiency is relatively insensitive to the chemical composition of an olivine substrate, but *is* sensitive to its physical composition, with rougher surfaces increasing the rate of formation.

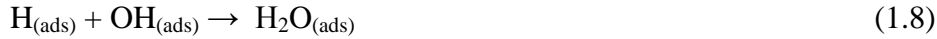
In the cool, dense regions of the ISM (about 10^{12} particles m^{-3}), $[H^\bullet]$ reaches sufficient values that dihydrogen formation becomes significant, eventually leading to $[H^\bullet]/[H_2] < 1$: dense enough that grain-mediated radical-radical combination reactions can occur at a significant rate. Although the formation of H_2 is exothermic (releasing 4.5eV), the desorption of a linear molecule generates rotational and vibrational degrees of freedom in which the energy can be accommodated, and so in fact *lowers* the kinetic temperature of the cloud further— encouraging subsequent ice formation.

Denser clouds also achieve better thermal coupling between the gas phase and the solid phase as the collision frequency increases. Over millions of years this energy reappportionment can play a crucial role in the progress of Kelvin-Helmholtz cloud contraction, to eventually form protostars from coalescing ISM ^[17].

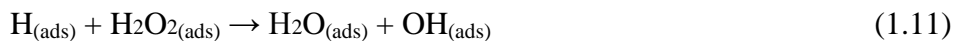
The gradual building of molecules from atoms (or smaller molecules) on the surface of dust grains can proceed by Eley-Rideal ($A_{(ads)} + B_{(g)} \rightarrow C$) or more commonly Langmuir-Hinshelwood ($A_{(ads)} + B_{(ads)} \rightarrow C$) mechanisms. Between 10 and 30K, atoms including H, D, C, O, and N have sufficient energy to diffuse across the surface of a dust grain but probably not *off* it; indeed, models generally assume the sticking probability on grains in the cold ISM is unity ^{[10] [29]}. From these atomic building blocks, simple molecules like H₂O, HCOOH, CH₄, NH₃, and CO₂ ^[30] can be formed. The composition of the ice mantle which slowly accretes therefore strongly reflects the local chemical and physical environment.

Various generation routes proposed for water include primarily hydrogenation reactions, such as ^{[31] [6]}:

Monatomic oxygen



Diatomic oxygen



Almost everywhere we look with telescopes, water is the dominant ice molecule, followed by CO and then other species at orders of magnitude lower concentrations. Experiments show ^[32] that the rate of reactions 1.8, 1.9, and 1.11 dominate, the precursors of water being much more efficient scavengers of adsorbed hydrogen than

other species like carbon monoxide. Because water remains the principal component of all astronomical ices, understanding it remains imperative to understanding astronomical grain processing in general.

1.5 – The crystalline structures of water

Before we move on to consider the specific nature of the ices that form in space, first we reprise what is known about water ice from terrestrial studies.

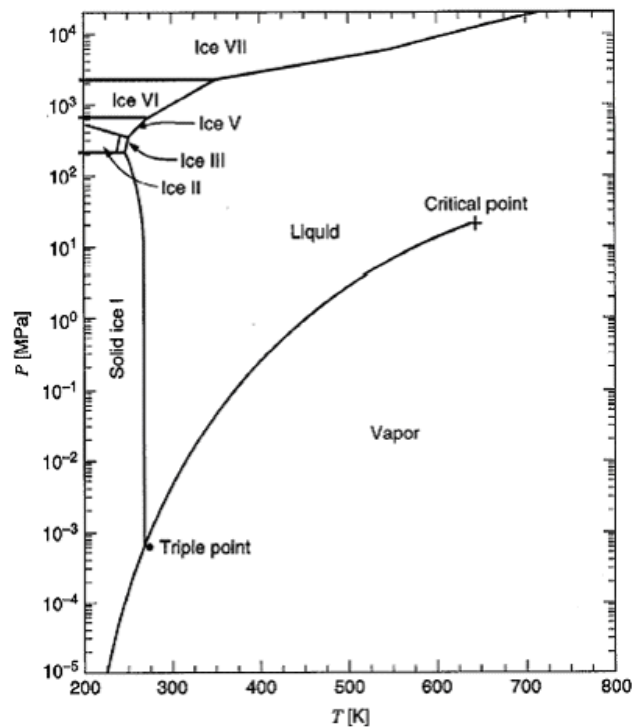


Figure 1.7: Partial phase diagram of water, reproduced from [33]

Water's phase diagram, displayed in Figure 1.7, shows a great many different stable and metastable phases, including at the very least nine stable and four metastable solid ices. On Earth, all naturally occurring ice is the hexagonal crystalline I_h , with the exception of small quantities of metastable I_c in the upper atmosphere. Terrestrial ices in the biosphere form through relatively slow cooling of bulk liquid water, with crystallite growth propagating from a seed nucleation site.

In liquid water under standard conditions, the two hydrogen atoms and two lone pairs adopt a pseudo-tetrahedral arrangement around the central oxygen atom, as might be anticipated from a facile VSEPR model. The bond angle in hexagonal ice shifts from

the 104.5° of liquid water to 109.5° - very close to a perfect tetrahedron - to minimise the energy of the bonding network; intramolecular strain is balanced by intermolecular relaxation. The strength of liquid water's hydrogen bonding is optimally about 23.3kJ/mol (i.e. $\sim 8k_B T$ at 273K); much stronger than the typical dispersive interaction ($\sim 1\text{kJ/mol}$) but much weaker than a covalent bond ($\sim 400\text{kJ/mol}$). Melting at 1 bar produces a 8.3% density increase, and the heat of fusion is 6.01kJ/mol – a figure which implies that most of the hydrogen bond network remains unbroken on melting. Liquid water's energetic stability (an enthalpy of vaporisation of 44 kJ/mol under standard conditions) arises from the formation of transient tetrahedral arrangements in which bond strength and directionality impose a low local density and cause a loss of configurational entropy. At low temperatures, then, H-bonding encourages an increase in volume which lowers both energy and entropy, while in most liquids, these properties are positively correlated. Water's volume decrease on melting – which is itself very unusual – actually continues in the liquid phase, between 0 and 4 Celsius, decreasing from $18.0182\text{ cm}^3\text{mol}^{-1}$ to a minimum of $18.0158\text{ cm}^3\text{mol}^{-1}$, and then back up to $18.798\text{ cm}^3\text{mol}^{-1}$ at the boiling point ^{[33][34][35][36]}.

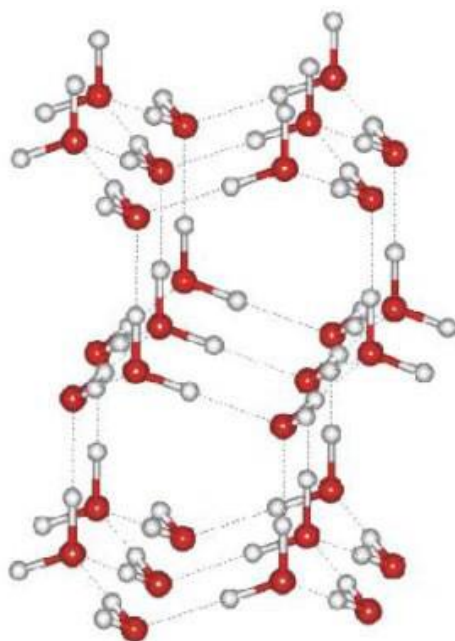


Figure 1.8: Tetrahedral bonding geometries in crystalline I_h . Red spheres represent oxygen atoms and white spheres represent hydrogen atoms.

The structure of familiar hexagonal ice, as shown in *Figure 1.8*, can be considered as ABAB planes of tessellating hexagonal rings linked at each vertex by hydrogen bonds (the cubic-close-packed analogue, I_c , is similar but stacks as ABC). Both these forms of ice have a very open structure, accounting for their low density. I_h water molecules adopt a diamond-like, four-co-ordinate structure, with each molecule participating in four hydrogen bonds (two donor and two acceptor). The many other stable ices in the phase diagram of water give different crystal structures to the solid, induced by high pressure. Ice II, for example, has a rhombohedral structure and can be created by compression of I_h at 300MPa; while ice III is a tetragonal lattice formed by heating ice II under pressure to 250K^[33]. The equilibrium phase diagram does not, however, encompass all of the structures which water can adopt – there are, in addition, metastable phases which do not represent the global energy minimum for the system under *any* conditions, but which nonetheless serve as local minima in phase space, as kinetically rather than thermodynamically stable bulk structures.

1.6 – The amorphous structures of water

Just as there are multiple phases of crystalline water ice, so too are distinct phases of metastable ice; water is polyamorphic, having more than one amorphous phase. In fact there are at least three different water polyamorphs, with additional, *potentially* distinct phases that have been synthesised, although the criteria of what actually constitutes a separate phase in ASW remains contentious. Furthermore, there has been some confusion in the literature with the nomenclature of these distinct phases; for the remainder of this thesis, we will follow the current convention, which is:

- **Amorphous solid water** (ASW) ice is material which we produce in the laboratory in molecular beam deposition experiments, and expect to see in space: a mixture of the next three polyamorphs.
- **Low-density amorphous** (LDA) ice is the predominant component of ASW; inefficiently packed water molecules in an aperiodic arrangement. The main component of ASWs produced by slow physical vapor deposition on a cold substrate ($>77K$).

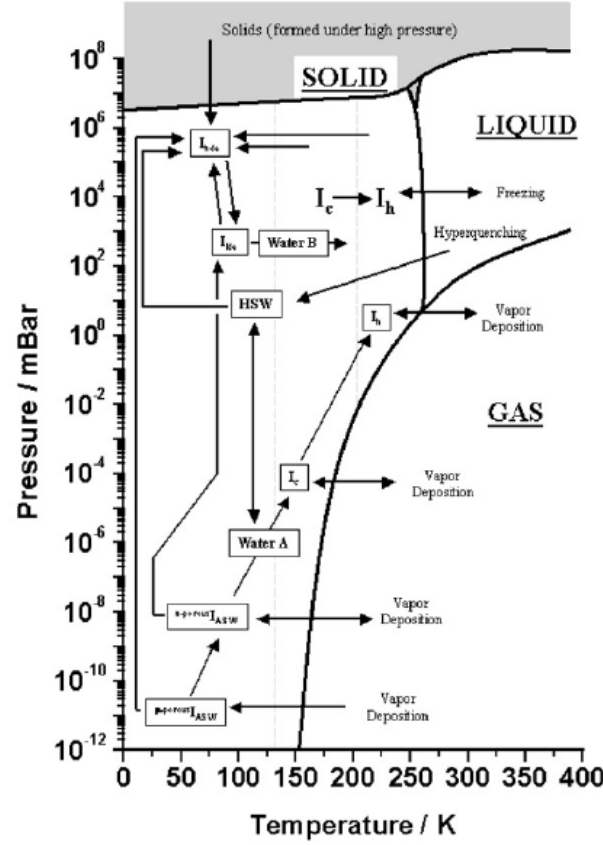


Figure 1.9: Figurative phase diagram at the low temperature / pressure corner of the ice landscape (see Figure 1.7). All the structures highlighted in boxes are not the lowest thermodynamic points for the temperature and pressure conditions, but rather metastable states which may have relaxation rates in excess of billions of years when undisturbed in the stellar medium. Reproduced from [37].

- **Hyperquenched glassy water (HGW)** is formed by cooling a fine mist of micrometer-sized water droplets at a rate of around 10^6 K/s (vitrification). Cooling has to be this fast to outpace the formation of nucleation crystals and then bulk crystalline structure. Although some differences have been reported, it is generally believed on the basis of neutron and X-ray diffraction that LDA and HGW are the same material.
- **High density amorphous ice (HDA)** can be produced by compression of either LDA or HGW at $T = 77\text{K}$ and $P = 0.6\text{GPa}$, or alternatively by compression of crystalline I_h or I_c at $T = 77\text{K}$ and $P > 1\text{GPa}$. HDA is metastable at $T = 77\text{K}$ and $P = 1$ bar, but heating up to 125K will cause it to

transform irreversibly into LDA. Computer simulations indicate that HDA could be produced by hyperquenching of high density *liquid* water, but the high-pressure vitrification which would be necessary to demonstrate this in the laboratory, is practically problematic.^[38]

- **Very high density amorphous** ice (VHDA), 7-8% denser than HDA and produced by heating HDA under pressure.^[39]

All these ices are able to form because, at low temperatures, the molecules lack sufficient energy to overcome the kinetic barrier to rearrangement into a thermodynamically favorable crystalline solid. While LDA, HGW, and HDA are accepted by a majority of researchers (the distinctions between them elucidated principally via density measurements and neutron or X-ray diffraction), there remain many points of contention; including that VHDA and HDA are the same structure^[40], or that additional forms can be generated via rapid freezing in the constricted environments of zeolite pores^[41].

Much of the theoretical justification for the polymorphism of ice arises from the predicted existence of multiple distinct phases of *liquid* water – “low-density liquid” (LDL) and “high-density liquid” (HDL) - for which LDA and HDA are the corresponding glasses. The presence of phase transitions between different glassy states of an isotropic liquid under supercooled conditions (that is, below the freezing point but quicker than the kinetics of crystallisation) is one of the proposed methods to avoid the Kauzmann catastrophe – where the extrapolated entropy of the glass would be less than that of the crystal. As water is supercooled, there may be singularity-like variations in its thermodynamic properties, indicative of a liquid-liquid phase transition with an associated liquid-liquid critical point (contrasting to the liquid-gas T_c at 647K), existing somewhere within the supercooled region.

Due to the inherent experimental difficulties in accessing these temperatures, simulations are the preferred method of investigation, although even they are limited not just by computing time but also by other pragmatic factors. In the NVT ensemble (i.e. a variable pressure system), for example, it is notoriously difficult to distinguish a sharp *discontinuous* change in density (representing a phase change) from a sharp *continuous* change (indicating nothing in particular). Also, the better (i.e. more

physically realistic) a simulation gets, the more it tends to run into the same practical problems as do experiments (that is, crystallisation). The formation of hexagonal ice can be suppressed by forcing the system to remain homogeneous even in metastable and unstable states (thus preventing nucleation), and while this significantly improves the ability to study liquid-liquid phase transitions, in restricting the allowed fluctuations of density one risks making the system un-physical.

Studies in [42] using ST2 (an early 5-site model of water; see *Section 2.8*) show a phase transition in the supercooled region; two phases, with densities of 0.91g/cm^3 and 0.97g/cm^3 , coexist in this region, with a triple point at 270K and 0 pressure where the liquid/liquid (glass/glass) and liquid/vapour first order phase transitions meet each other. However, the conditions under which the triple point is located are strongly dependent on the model used; for example, the glass liquid/glass transition in ST2 at 0 pressure occurs at 235K, while in another water model, TIP4P, it is located at 180K, and in TIP5P at 215K. This demonstrates the dangers of extrapolating properties from simulation models which have only been parameterised to work accurately at ambient temperatures.

Given that the amorphous ice forms are metastable states preserved only by kinetics rather than thermodynamics, the physical properties and molecular organisation of the substances are inextricably dependent upon the mechanics of their formation. While neutron diffraction studies indicate large *similarities*, ASW (either LDA, HDA, or VHDA) produced by compression of crystalline ice is not necessarily the same as that produced by hyperquenching (HGW) or by physical vapour deposition upon a cold substrate. Simulation studies ^{[43][118]} indicate that rather than (or even, in addition to) there being a series of discrete ASW phases corresponding to the glass of a crystalline ice phase, there may be a pseudo-continuum of intermediate structures between LDA and VHDA (0.91g/cm^3 to 1.30g/cm^3). In Parrinello et al. ^[40] there is reported a particularly noticeable “pre-transition” at 1.24g/cm^3 , suggesting that the transition from LDA to VHDA occurs in a multi-step-wise process following local minima in the free-energy landscape. The steps might be most physically corresponded to the increase in oxygen co-ordination numbers as interstitial sites in the first co-ordination

sphere become occupied due to increasing pressure.

Zhang and Buch conducted a computational study ^[44] into the vapor aggregation of water into gas-phase clusters. Here, an incoming molecule bonds to the pre-existing ice-film surface via a hydrogen bond; usually the O of an incoming molecule bonding to the H of a surface molecule (the inverse, $H_{(g)} \rightarrow O_{(s)}$, occurred only about half as frequently). The single-hydrogen-bonded form rarely persisted beyond a few picoseconds; molecules relax into a two-bonded “OH” configuration; that is, with two hydrogen-bonds to the surface, one via its oxygen and one via one of its hydrogens. Alternative configurations, “OO” (using both oxygen lone pairs) or “HH” (using both hydrogens) were rarely seen. This results in a 2-co-ordinate surface molecule, with two dangling H-bond sites. “OO” is expected to be rare because it requires the surface to present to the incoming water molecule two dangling hydrogens in close proximity, which is disfavored by Coulombic interactions (likewise for proximate Os in “HH” binding).

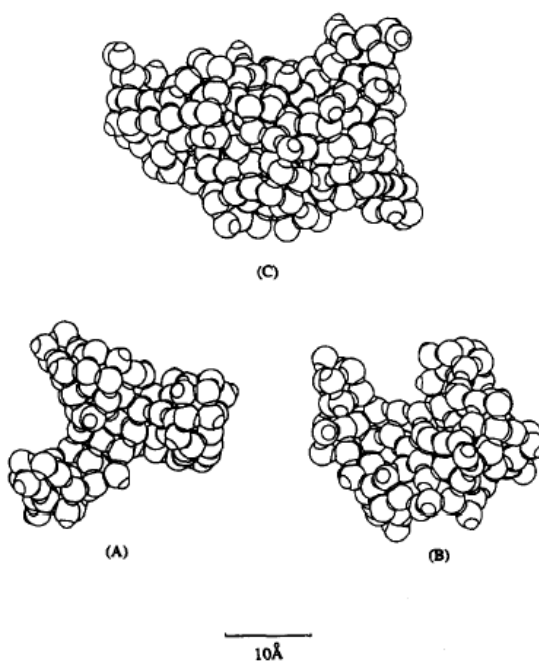


FIG. 1. The three calculated clusters (A) 112 water molecules, $T \sim 10$ K, (b) 160 water molecules, $T \sim 10$ K, and (C) 296 water molecules, $T \sim 70$ K.

Figure 1.10: Gas-phase ice clusters formed in simulation, from different numbers of water molecules at different temperatures. Note that there is no long-range order; the structures are ASW. Reproduced from [44].

Three and four co-ordinate molecules were usually formed by the sticking of additional incoming molecules on top of two co-ordinate surface molecules, burying them in the amorphous ice structure. In three co-ordinate molecules, the OHH connectivity was more frequently seen than OOH, on account of incoming molecules' preference for bonding to surface Hs.

Occasionally, ice molecules with fivefold co-ordination were seen in [44], with three hydrogens 'bonded' to one oxygen. Although a fifth co-ordinate bond cannot be not true hydrogen bonds, the low surface mobility of the cold H₂Os means that on occasion, the only site available for a dangling hydrogen was an already 2-bonded oxygen which is sufficiently exposed to attract further attachments.

The mean number of hydrogen bonds per molecule in ASW was calculated at about 3.5. Although molecules in the bulk of the ice preferred 4-co-ordination, 3-co-ordinate waters did remain trapped in the ice, and many molecules are *not* in the bulk, being still accessible on the surface. For astrochemical ices, this suggests high surface area to volume ratios can be expected.

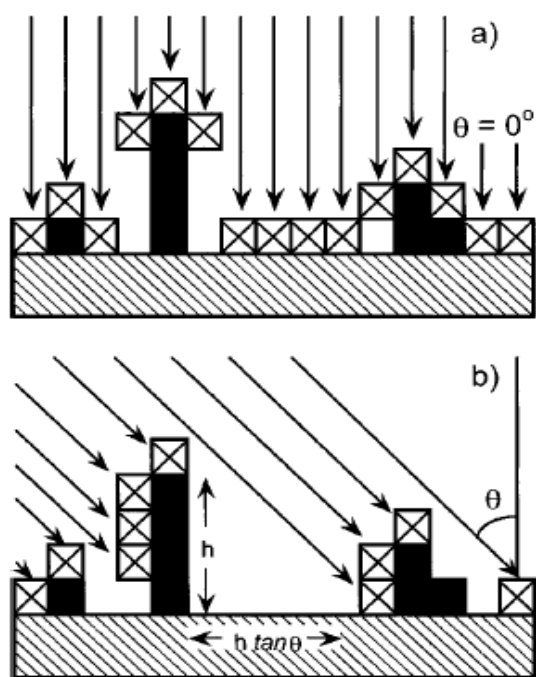


Figure 1.11: Incident angle control in ASW. Reproduced from [45].

The angle of incidence is believed to be an important factor in determining the overall porosity of the ASW when surface diffusion is slow compared to the rate at which new molecules arrive. Kimmel et al report ^[45] that molecules incident normal to the surface generally create a dense, uniform ice film, but molecules incident near-parallel to the surface create a much more porous ice, adhering to the sides of columnar structures and producing a nanoscopic landscape of peaks and “shadows” where the intervening structures prevent H₂O deposition (see *Figure 1.11*).

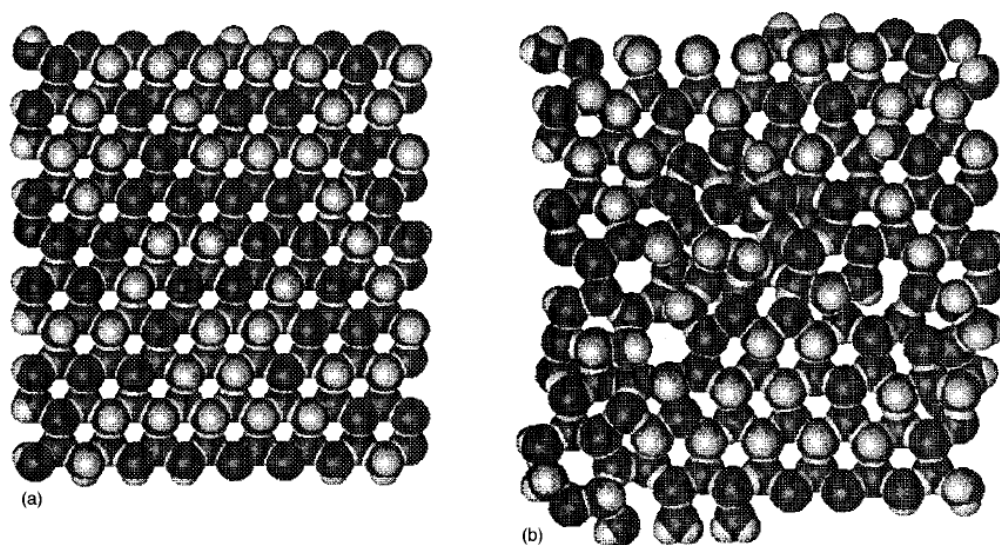


Figure 1.12: Surface rearrangement of simulated crystalline ice on annealing. The ordered structure which serves as an energy minimum for the bulk is unlikely to be as advantageous for the surface on account of dangling bonds. A profound and irregular re-ordering is observed. Dark spheres represent O atoms and bright spheres represent H atoms. Reproduced from [46].

Further investigations into the structure of a cold ice surface were conducted by Devlin et al. ^[46], to study the rearrangement under annealing (see *Figure 1.12*). In a Molecular Dynamics simulation of 6 water bilayers at 27K, annealing to 197K and then re-quenching saw primarily the top layer re-order to increase the average coordination number of its molecules, at the expense of the original tetrahedral bonding structure. The simulated spectra calculated from these MD runs showed broad agreement with experimental spectra from water annealed in the same way.

The simulations in general suggest to us that solid water generated at very low temperatures will adopt a non-crystalline morphology, with an irregular surface; and even crystalline ice surfaces will rearrange to irregular structures if annealed. While annealing disorders the surface, by contrast it *orders* the bulk, smoothing out micropores and inducing a gradual transition from ASW to cubic ice by 130K (see *Figure 1.9*).

Specifically for the ices that are relevant to our protostellar interests, the zero-gravity environs might be expected to exert a significant influence over the mesoscopic structure of astronomical ices compared to those that can be grown in a laboratory on Earth. No weight-induced compaction occurs, and pore sizes in astronomical ices are able to grow larger than they would in a 1g environment. In space, convection is suppressed as Rayleigh-Bénard density differences don't migrate downwards under gravity; leading weaker surface-tension-based (Bénard-Marangoni) effects as the main mediators of convection. Minimising convection means layer discrimination becomes easier for solids, and so microgravity ices which form *crystals* are expected to have fewer defects than those grown under terrestrial (but otherwise identical temperature and pressure) conditions ^[37]. Escribano *et al* ^[47] reports that deposited ice films can have substantially different mesoscale morphologies depending on the precise temperature conditions of their deposition and subsequent thermal history; 'cauliflower', 'matchstick', 'dendritic', and 'sponge-like' forms all being identified in their investigations.

1.7 – Mixed ice chemistry and water observation

Our discussion on the nature of solid state chemistry in space in *Section 1.4* suggested that H₂O is generated by chemical vapour deposition on silicate dust grains, and so the study of CVD water would seem to be the sensible approach for determining the physical and chemical composition of a protostellar environment. However, simulations by Visser *et al.* ^[48] indicates that the water ice in the stellar accretion disk - accounting for 30% of the total oxygen inventory of the natal core, and the dominating source of planet-forming material – is not pristine CVD water, but rather *physically* vapour deposited water. As the icy grains enter the nascent protoplanetary

disk, they heat up and their original CVD layers are totally evaporated by the heat of the star. However, as the protoplanetary disk evolves and incorporates more material, it expands to conserve angular momentum. Grains and gas-phase water may then find themselves carried over the disk's “snow line”, where the distance from the star means temperatures are cool enough for re-condensation. It is *this* water which is relevant to understanding the chemistry of the disk, and so it is this water that we focus on.

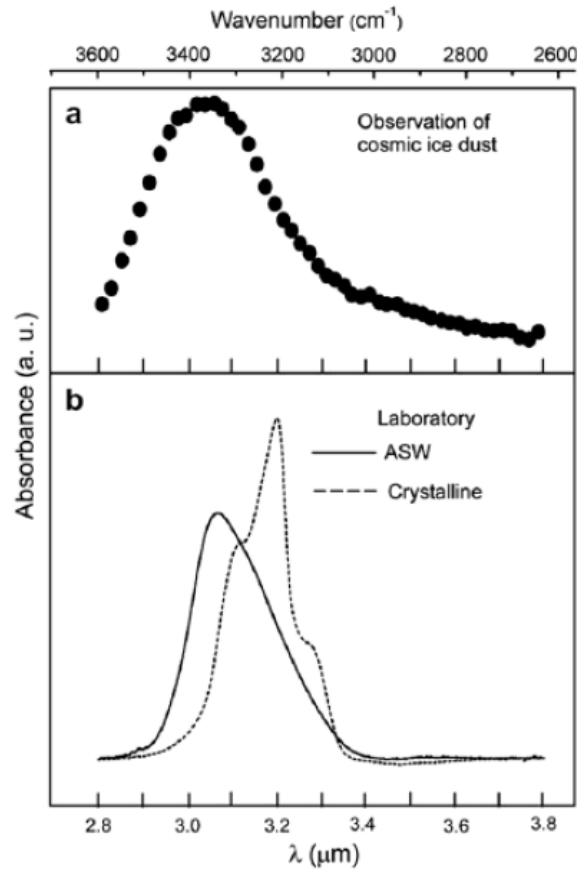


Figure 1.13: The band profile for water from telescopic observations indicates an amorphous structure, but such observations cannot provide conclusive information on the details of the ice arrangement regarding either physical or mixed chemical composition. ^[49]

When ice-bearing clouds are identified by adsorption spectroscopy, H₂O has a characteristic band at 3.07 μm corresponding to the O-H stretching mode, with an additional peak at 6.0 μm from the bending mode. Ices can be distinguished from molecular gases spectroscopically both by the broad features of the adsorption spectrum between 25 and 1000 μm, arising from lattice mode vibrations; and by the

lack of any fine structure in the spectra which would arise from rotational excitation. The spectra can also be indicative of the purity of the ice; for example, the O-H stretching peak shifts by 20cm^{-1} and broadens by a factor of 2 when CO_2 is mixed in with the water ice ^[50], and there are a plethora of other effects which can show the presence of other components. The broadness of the observed peak in *Figure 1.13*, and the lack of any fine structure associated with crystalline ice, indicates that the astronomical water is amorphous. However, we cannot derive any information about *which* polymorph it is, its density, or other relevant properties from telescopic spectroscopy alone, which leads us back to lab experiments.

Thin surface films of ice can be generated in vacuum chambers by ballistic deposition from molecular beams - which can be collimated to control the energy and positioned to control the angle of deposition – or by effusive methods where water gas is introduced to the chamber by leak valves (*Section 1.8*). Fraser *et al.* give a detailed description of the experimental setup in [51]. Ices constructed in this way – similar to the expected mechanism in cold clouds – produce full surface coverage ice films with no long-range order. The ices are, significantly, porous – which, if replicated in an astronomical context, suggests certain properties when water ices are combined with other significant solid state molecules, notably CO.

The current prevailing model for the mixing of water and CO ices begins with the adsorption of CO on top of an existing porous water ice surface, as illustrated by *Figure 1.14*. Carbon monoxide remains in the gas phase at lower temperatures than water, so freezes out in a layer above H_2O .

Capture of gaseous CO by a purely H_2O ice layer was simulated in two Al-Halabi papers ^{[52][53]} (depiction in *Figure 1.15*). For non-rotating CO molecules impacting a 90K ASW surface at a normal angle and 116K translational energy, the sticking probability was found to be essentially 1; that is, there is no rebound. Calculations show that CO interacts with the water molecules most strongly via a OC – HO arrangement of δ^- - carbon with a dangling hydrogen bond, supplemented by further interactions with saturated (bonded) OH groups. These dipolar bonds are believed to

account for observed infrared bands at 2139 cm^{-1} and 2152 cm^{-1} respectively, which corroborates that CO does indeed form combination ices on top of water. A similar study of CO adsorption by Manca et al. [54] came to the same conclusion based on volumetric and spectroscopic data: carbon monoxide associates most strongly with a dangling ice OH bond.

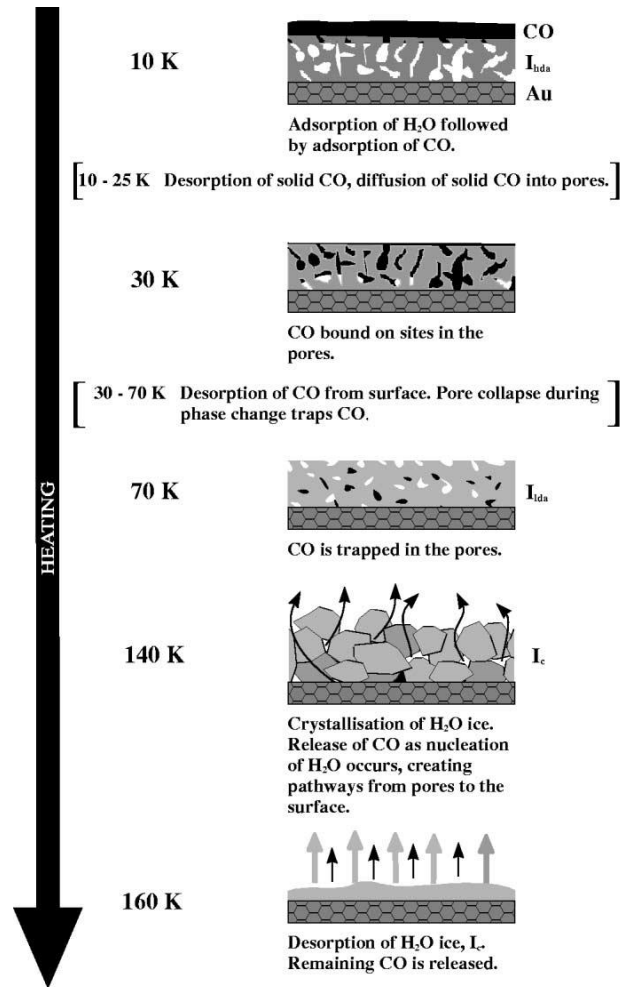


Figure 1.14: Proposed thermal processing of water / CO ice. Deposited CO becomes trapped within pores in the water ice, and is only released to the gas phase when ASW undergoes a phase change at 140K. Reproduced from [55]

Carbon monoxide which deposits on top of the porous H_2O ice may diffuse across the surface of the ice, and into pores in the water structure. According to experimental studies by Palumbo, the limiting minimum temperature is 26K for CO migration across the irregular ice surface [56]. Subsequently, as grain temperature increases, the pores begin to constrict as H_2O rearranges (see *Section 1.4*), and CO can become

physically trapped, preventing it from subliming even above its desorption temperature. Eventually, when the ice goes through a phase change at 140K, structural rearrangement and cracking produces channels by which the CO can migrate out and into the gas phase. Further heating to water's desorption temperature will see the whole ice layer stripped from the grain, as shown in *Figure 1.14*.

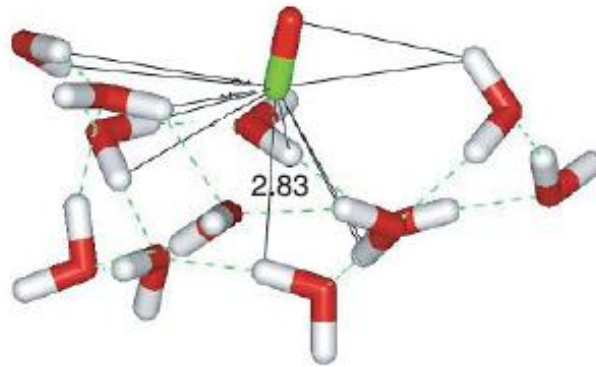


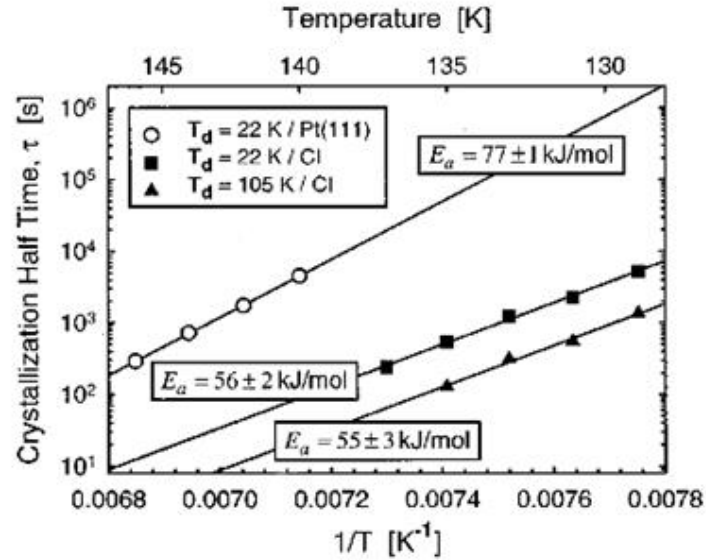
Figure 1.15: Carbon monoxide on disordered ice. Reproduced from [53]

This model – one of CO captured in pores, depleting it from the gas phase even at temperatures where it should have desorbed – is the only one which adequately explains observed carbon monoxide intensities with respect to temperature around protostellar cores. It suggests that the amorphous solid waters produced in lab experiments are, at least in general, analogous to the ASW formed in space, as they reproduce the porosity necessary to explain CO's observed behaviour^[57].

The substrate on which the water molecules are deposited may exert a secondary influence on the structure formed. We can consider the adsorption of molecules onto a bare silicate dust grain, but also continuing the deposition of an existing ice film.

Jenniskens and Blake report^[58] that the morphology of the grain surface is important to template the morphology of the ice which forms in a pseudo-epitaxial manner. ASW phase changes to I_h when heated to 140-160K at zero pressure (see *Figure 1.16*); but if the substrate on which the ASW is deposited is itself I_h , the crystallization occurs orders of magnitude faster than it does on a Pt [1,1,1] surface. Changing from ASW to I_h means the volume of the solid decreases significantly,

which would give rise to stresses and inevitably cracks in an icy body as it heats up during the course its trajectory in a protoplanetary disk.



Arrhenius plot of the crystallization half time, $\tau_{1/2}$, of ASW films deposited on Pt(111) at $T_d = 22$ K (open circles) and on crystalline ice (CI) substrate at 22 K (closed squares) and at 105 K (closed triangles). The slopes yield an apparent activation energy for ASW crystallization of 77 ± 1 kJ/mol on Pt(111) substrate and 56 ± 2 kJ/mol ($T_d = 22$ K) or 55 ± 3 kJ/mol ($T_d = 105$ K) on a CI substrate.

Figure 1.16: Survival times of ASW on heating. Those ices which were deposited on an existing I_h surface required less energy to crystallise than those which were deposited on platinum surfaces. Reproduced from [58]

Besides water, other species can be detected as integral components of an emerging protostellar envelope, as shown in *Figure 1.17*. Silicate signatures are found in the spectra of clouds too, confirming the presence of dust grains via the Si-O stretching mode at $9.0\mu\text{m}$ and the O-Si-O bend at $18.0\mu\text{m}$; CO is also seen in abundance, with the C=O stretch at $4.67\mu\text{m}$ (which can be resolved into hydrogenated and non-hydrogenated peaks). More trace species include $^{12}\text{CO}_2$, $^{13}\text{CO}_2$, OCS, CH_3OH , H_2CO , and CH_4 , with evidence for minor nitrogen-containing species like NH_3 and OCN. If clouds find themselves subjected to high UV fluxes, photodissociative-recombinative species like H_2O_2 are expected to form; although the observational evidence is poor,

laboratory tests do detect peroxide under ultraviolet photon irradiation of ASW. ^[59]

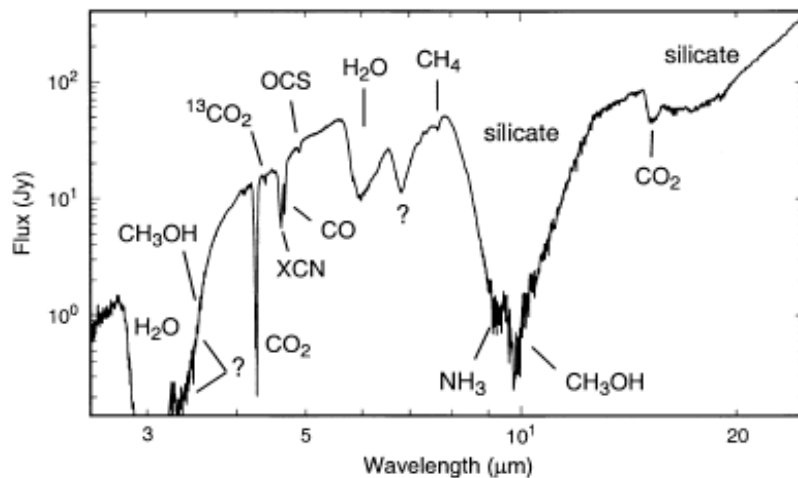


Figure 1.17: Species assignment for spectra from served embedded protostar W33A, showing broad signatures from H₂O and silicate grains, as well as common astrochemical species like methane and CO. Reproduced from [60]

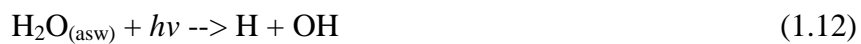
Stellar nurseries producing low, medium, or high-mass stars can evolve different astrochemical abundances in their circumstellar envelope due to their different temperature/time gradients. High-mass stars enter the main sequence faster, with a steeper heat gradient. This reduces the concentrations of grain-surface species requiring intermediate formation temperatures (up to 50K), because cold conditions do not persist for as long. Low mass stars see a greater abundance of ethers and carboxylic acids compared to their parent molecules methanol and formaldehyde, attributed to the fact that they spend longer in this temperature regime, although the excess is attenuated by the fact that they then spend more time at pre-sublimation temperatures (70-80K) which gives longer time for grain-surface hydrogenation of C=O groups.

High-mass stellar environments see a greater abundance of exotic species formed by high-temperature radical-radical recombination on account of the fact that they reach the necessary T faster. Molecules of this sort include (NH₂)₂CO (urea) and (CH₂OH)₂ (ethylene glycol); overwhelmingly formed from primary radicals (the few secondary radicals that exist tending to be insufficiently mobile to do anything but hydrogenate) ^[23].

A long-standing problem in gas-grain modeling is that simulations predict overabundances of methane and under-abundances of carbon dioxide compared to observation; the scarcity of CO₂ going on to contribute towards under-abundances of formic acid (HCOOH) and its derivatives. It is suspected that this may be due to underestimates of the initial temperatures of cold cloud collapse, or incorrect modeling of the surface chemistry ^{[12][59][61]}. This emphasises again the potential utility of our investigations onto the ubiquitous water films: only by understanding the structure of the grain surface can we make adequate predictions about their retention or catalytic properties for other species in the astrochemical mix.

Ices can be photodissociated by UV rays, typically inducing homolytic fission of an X-H bond to produce an evaporating hydrogen atom and a larger, grain-bound molecular radical. However, in the cold ~10K temperatures at the core of dense clouds, “large” radicals are not particularly mobile over a grain surface, lacking the energy for diffusion. Accordingly, hot temperatures around stellar cores are crucial for the formation of more complex species, allowing radicals to move and combine to form yet larger molecules. Methanol and formaldehyde are found to be particularly important molecules in astrochemical networks, as they provide most of the basic radicals that can produce organic species, as well as having rich non-radical ion-molecule reaction chemistries which serve as important starting routes to produce higher mass molecules.

Aside from the production of radicals to generate complex organic molecules, radiolytic processes in ASW are also important for understanding the evolution of ices in an astronomical context, as elucidated in a comprehensive Molecular Dynamics study by Andersson et al ^[62]. The absorption band of ice for the transition $A^1 B_1 \rightarrow X^1 A_1$ absorbs strongly over 130-165nm (part of the UV spectrum), and photodissociation of H₂O can take place in the ice:



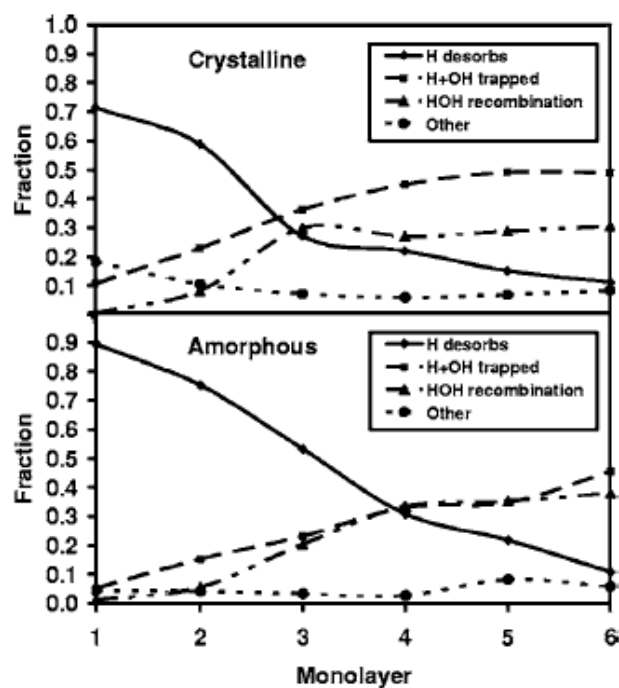


Figure 1.18: Photo-fragmentation fates in ice, showing the different escape probabilities of photo-fragments between amorphous and crystalline samples. Reproduced from [62]

Simulation of the fates of the photo-fragments from this dissociation process (see Figure 1.18) indicate that the major fate of molecules in the surface layers is to expel a H atom into the gas phase, with the OH radical remaining trapped in the ice. To see OH desorb and H remain trapped occurs in only about 2% of cases for the top amorphous monolayer (and effectively never for deeper layers); although OH escape overall (on its own or accompanied by H) is much more probable in crystalline ice, with about 9% of first-monolayer I_h photodissociations expelling OH.

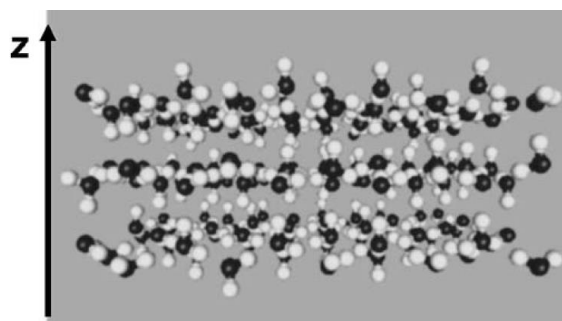


Figure 1.19: Crystalline ice's stacked bilayer structure discretises the escape probability of photo-fragments. Reproduced from [62]

Crystalline ice has a kind of step function in fragment escape probability, reflecting the bilayer structure of I_h (see *Figure 1.19*), whereas the probability decreases in amorphous ice more linearly.

Recombination of trapped fragments in irradiated ice is least effective in the upper layers because competing processes (desorption or separation) occur with higher efficiency here, and also because there is less opportunity for vibrational de-excitation without a full cage of surrounding molecules to soak up the energy. Other studies ^[63] suggest the rate of H loss is largely independent of temperature.

Since the OH photoproducts are usually trapped on the surface of the ASW while the H fragments are not, this means the OH radical termination step generally has to be combination to form H_2O_2 . This can itself be re-photodissociated into 2OH fragments, which in turn provides a secondary avenue for OH production:



Bombardment of ASW by low-energy electrons as opposed to high-energy photons is reported as being able to liberate H_2 . Above energies of about 6eV, gas evolution is expected to occur after dissociative electron attachment (DA):



There is evidence for this reaction in the gas phase, and it is expected to be enhanced in condensed phases due to the greater density of collision partners and better exothermicity arising from solvation. This and other means of depleting hydrogen within solid ice is expected to deplete its content in interstellar ASW, which has ramifications for the rates of cold hydrogenation chemistry which are expected to occur on its surface. Again, understanding the structure of the ice will improve our ability to predict likely rates of retention or emission of photochemical products, thereby informing the chemical networks which rely on knowing their concentrations.

Section 1.8 – Current understanding of astronomical water

From *Sections 1.4, 1.6, and 1.7*, we can collect an overview of the current understanding of astronomical ASW:

Laboratory Experiments

Lab-grown ices under pseudo-astronomical deposition regimes demand high vacuum and low temperatures. Water or other relevant molecules are introduced to a chamber by gas lines, and the resultant ices constructed by physical vapour deposition ^[51]. Porous HDA / LDA structures are produced, which fit well with current observations and theory regarding the gas and solid phase abundances of H₂O / CO.

The obvious advantage of laboratory techniques is that the ices are available for analysis and subsequent work, usually temperature programmed desorption ^{[63][119]}. However, there are limitations which arise from the methodology. Firstly, the rates of deposition, notionally on the order of 10^{-10} mol s⁻¹ ^[64], are still orders of magnitude in excess of those expected in space, where the exceptionally low particle densities mean collision frequencies are measured per hour rather than per nanosecond. Secondly, there is a low-temperature limit on the effective temperature of the incident water molecules. In order to introduce water *into* the vacuum chamber it needs to be sufficiently warm so as not to condense inside the gas line. Gibson *et al.* ^[65] recorded a minimum practical gas temperature of 273K for precisely this reason.

Observations

Ice in space can be analysed *in situ* with telescopes through ro-vibrational spectroscopy, the characteristic signatures of which suggest that most water ice in the universe is both amorphous and dirty – mixed in with numerous other components, most prevalently carbon monoxide. ^[59]

However, many unanswered questions remain about the chemical identities of minor ice components (see *Section 1.7*), as well the reasons behind the absence of expected spectral lines ^[66] and the presence of *unexpected* lines ^[67]. Remote observation can

also tell us little about the mechanisms of chemical process in ices, nor the dynamic evolution of cloud composition – because the timescales are much too long.

Simulation

Many of the practical problems of both lab experimentation and observation can be evaded with simulation studies. Chemical networks have been used to model the long-term make-ups of cold clouds and their molecular inventories, supporting the premise that water can form on dust grains (*Section 1.4*) and then evaporate into the gas phase, releasing an inventory of captured components (*Section 1.7*). Meanwhile, molecular dynamics studies can probe short-term processes, like the adsorption of surface species or the behaviour of radiolysed fragments.

The obvious problem with simulation is that a result is only as good as its model. Specific values for important simulation parameters are often not known, and must either be estimated from analogous species or inferred by trial and error (see *Section 2.8*).

1.9 – Summary

The interstellar medium – despite being the most prevalent material in the universe – is also one of the least understood, on account of its remoteness, low density, and exceptionally slow dynamics. It is believed that the majority of the ISM is hydrogen gas, with a small proportion of dusty grains. Chemical reactions are mostly restricted to barrier-less processes on account of the dearth of kinetic energy between the constituents; but in spite of this, over 140 distinct species have been telescopically identified. Surface chemistry may take place when water ice freezes out onto dusty grains in a glassy form, and the ballistic deposition is expected to form peaks and rain shadows, creating an uneven layer of high surface area. Other molecules may become trapped in cavities and pores as thin layers build up over time.

When the ice layer heats up on moving to a different part of a nebula, the ice structure may undergo cracking or phase change, thereby releasing the stored molecules (perhaps cryo-volcanicly) and changing the local composition of the medium.

What we presently know about the interstellar medium is clearly an incomplete picture. Persistent mysteries like the Diffuse Interstellar Band ^[67] and the potential presence of polyaromatic hydrocarbons ^[68] point to a rich – if slow-moving – dynamic chemistry, but even for simple molecules like water, the evidence is far from clear. By what routes does water form chemically, and by what routes do its structures form physically? What is the nature (if any) of its equilibrium between the adsorbed and gas phases, and how does temperature affect this? Which molecules co-deposit, and which molecules form on water ice surfaces? What is the physical structure of the water, and how does it change over time?

It is non-trivial to match laboratory data to telescopic data in order to answer these questions, because the scales and densities involved are beyond the range of terrestrial experimentation. This is what makes simulation an attractive prospect, as a means of probing the problems which the physical laboratory cannot.

Chapter 2 – Molecular Dynamics

2.1 – Overview

The aim of this project is to understand the structure of amorphous solid water as deposited on dust grains in space. As mentioned in *Section 1.7*, observational studies of cold clouds cannot resolve the physical structure of water ice in situ beyond telling us that it is amorphous. At the same time, experimental studies lack the ideal temperature and rate controls to accurately reproduce astronomical deposition. This leads us to simulation.

There are various different varieties of simulation which have been developed for physical chemistry studies. Since we expect the hydrogen bonding characteristics of the ice to strongly affect the layers' structure, our technique should be one which adequately resolves the molecules' polar intermolecular attractions.

Molecular Dynamics is a computational technique which models particles as point objects, which interact with each other under a force model we specify. Given an arbitrary arrangement of particles in space, we can calculate the forces induced on each particle by each other particle as a function of their mutual displacement. Considering the sum total of forces on a given particle, we use Newton's laws of motion to calculate the induced acceleration it experiences, and therefore the trajectory along which it would travel in space.

This conceptually simple process swiftly becomes very computationally intensive as the number of simulated particles in the system increases, so Molecular Dynamics employs a number of mechanisms to keep the required processor power to a manageable level. Some of these methods are explored in this chapter (*Section 2.5*, *Section 2.6*), as well as details on the specifics of the force models required for water simulation (*Section 2.7*, *Section 2.8*). We explore these general characteristics of molecular simulation before going into detail about the specifics of methodology developed for astrochemical deposition, which is in *Chapter 3*.

Throughout this work the Molecular Dynamics package used is DL_POLY ^[69]., mostly ver.3.0 with a minority of simulations run in ver.2.0.

2.2 – The basic premise of simulation

In order that a computer simulation be useful to us in terms of displaying chemical information which may be difficult to determine directly through experiment, it must:

- a) accurately model the physics of particle motion and interaction, and
- b) run sufficiently swiftly that results are achieved within a reasonable timeframe.

Unfortunately, these two considerations are diametrically opposed. The computational cost of performing classical molecular dynamics (MD) in straightforward cases scales as N^2 (specifically, $\frac{1}{2}N[N-1]$), where N is the number of atoms in the model; that is, a system with four times as many particles requires sixteen times as long to simulate. Various methods are capable of reducing this factor (though with corresponding loss of accuracy), tending almost towards linear scaling. However, these classical molecular dynamics methods are limited in that they fail to consider electronic degrees of freedom of the atoms involved. Quantum mechanical modeling methods such as density functional theory do explicitly take electronic motion into account, and consequently produce more sensitive results, especially where covalent bonding is an important part of the system in question. The problem with these more accurate methods is that they frequently scale as N^3 or worse, restricting their applicability to smaller numbers of atoms and shorter timescales than purely classical models.

The premise of MD is that, under the Born-Oppenheimer approximation, we can separate the time-independent Schrödinger equation into distinct nuclear and electronic wavefunctions. As such, the instantaneous state of a modeled system can be described simply in terms of the positions and momenta of the constituent particles. The simulation progresses over a number of discretised time increments called timesteps, which are typically within the region of femtoseconds (1×10^{-15} s). There are several good reasons for restricting the timestep to this scale; it is faster than the vibrational frequency of intramolecular bonds (so allows us to model their oscillation properly) ^[70], and keeps higher-order expansions of particle accelerations

at negligible magnitudes ^[71]. At the start of a timestep, the forces upon each particle due to its instantaneous position are calculated, and used to solve Newton's laws of motion so as to determine the position and velocity of each particle at the end of the timestep. The atoms are moved to these positions, and the process repeats for as many timesteps as specified. This is computationally much less intensive than a full quantum treatment, and appropriate for the purposes of our system.

One of the most fundamental limits of Molecular Dynamics for our purposes is that of scale. As the computational cost of simulating N particles is usually greater than linear in N, the simulation of large system sizes is expensive. We cannot, for example, even approach modeling an entire micron-sized silicate grain at atomic resolution. Nor can these methods directly simulate the million-year timescales of grain deposition. In this work, we limit ourselves to $\sim 900\text{nm}^2$ of grain surface and $\sim 500\text{ns}$ effective runtimes, and must for now simply extrapolate Molecular Dynamics observations to the relevant distance and time scales.

2.3 – Short-range interparticle forces

The scale limitations on Molecular Dynamics arise principally from the computational cost of the force integration: calculating an induced velocity from the sum of the forces on each atom. The interparticle force relation used in this thesis is an electrostatic relation combined with a special 12-6 case of the Mie potential known as the Lennard-Jones potential:

$$U_{ij}(r_{ij}) = \frac{q_i q_j e^2}{r_{ij}} + 4\epsilon_{ij} \left[\left(\frac{\sigma_{ij}}{r_{ij}} \right)^{12} - \left(\frac{\sigma_{ij}}{r_{ij}} \right)^6 \right] \quad (2.1)$$

This potential is represented graphically in *Figure 2.1*.

The first term in *Equation 2.1* is the coulomb interaction, attractive or repulsive depending on the relevant partial charges. The 12-exponent is the short-range repulsive interaction (when the negatively-charged electron clouds on the particles begin to interfere with each other); the 6-exponent term accounts for attractive dipole – dipole interactions (or “London dispersion” forces) which arise from the feedback between the anisotropic instantaneous distributions of electrons around the atoms. The parameters ϵ and σ represent the maximum depth of the energy potential well,

and the equilibrium particle separation respectively (see *Figure 2.1*). These are empirical quantities determined by experiment where possible, and specific to the particular particle-particle pair interaction being considered; see *Section 3.4* for the specific values of the parameters used.

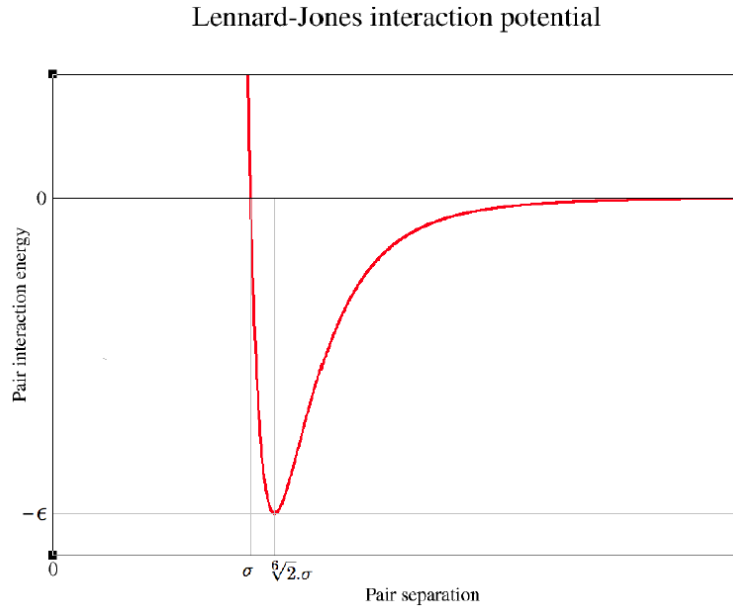


Figure 2.1: The Lennard-Jones interaction potential.

The Lennard-Jones equation, while a greatly simplified representation of the potential energy, still finds wide applications because of its simplicity and easy computation. The steep gradient of the repulsive 12-exponent as r decreases makes it a ‘hard sphere potential’ or Rigid Ion Model (RIM). A more accurate (and expensive) treatment would be to model explicitly the polarization and compression of the electron cloud on each particle in response to its instantaneous environment; MD simulations which do so are Polarisable Ion Models (PIM). The former is used throughout this work, as PIM’s extra complexity is not expected to translate into markedly more accurate results; see *Section 2.7*.

2.4 – Temperature control

Deposition events of gas on dust will liberate heat as the incident kinetic energy of the approaching particle disperses into the substrate. In order to dissipate this energy,

and maintain the system at the conditions we are interested in, we require some means of controlling the temperature.

Molecular Dynamics simulations can quote the temperature of their system exactly by calculating the instantaneous kinetic energy. In a system of N particles with coordinates $\mathbf{q} = (\mathbf{q}_1, \mathbf{q}_2, \mathbf{q}_3, \dots, \mathbf{q}_N)$, and momenta $\mathbf{p} = (\mathbf{p}_1, \mathbf{p}_2, \mathbf{p}_3, \dots, \mathbf{p}_N)$ the Lagrangian function (kinetic minus potential energy) can be expressed as:

$$L(\mathbf{q}, \dot{\mathbf{q}}) = \sum_{i=1}^N 0.5 m_i \dot{\mathbf{q}}_i^2 - U(\mathbf{q}) \quad (2.2)$$

where the sum gives the system's kinetic energy and $U(\mathbf{q})$ is the total potential energy of the system. The Hamiltonian function, $H(\mathbf{q}, \mathbf{p})$, is then given by:

$$H(\mathbf{q}, \mathbf{p}) = \sum_{i=1}^N \mathbf{p}_i \dot{\mathbf{q}}_i - L(\mathbf{q}, \dot{\mathbf{q}}) \quad (2.3)$$

The Hamiltonian equations of motion are described by:

$$\frac{\partial H}{\partial \mathbf{p}} = \dot{\mathbf{q}} \quad (2.4)$$

$$\dot{\mathbf{q}} = \frac{\mathbf{p}}{\mathbf{m}} \quad (2.5)$$

$$\frac{\partial H}{\partial \mathbf{q}} = \nabla_q L = \dot{\mathbf{p}} \quad (2.6)$$

$$\dot{\mathbf{p}} = -\nabla_q U = \mathbf{f}_i \quad (2.7)$$

Solving the first-order differential equations (2.4) and (2.6) above allow the trajectories of particles to be predicted over time. In this way we can probe the microcanonical ensemble (NVE), where the number of particles, the system volume, and the system energy are kept constant ^{[72][73]}.

The instantaneous value of the MD system's energy is explicitly related to the sum kinetic energy via:

$$\sum_{i=1}^N \frac{|\mathbf{p}_i|^2}{2m_i} = \frac{k_b T}{2} (3N - N_c) \quad (2.8)$$

where N_c corresponds to the number of constraints, such that the bracketed term is equivalent to the total degrees of freedom in the system. The average temperature, $\langle T \rangle$, corresponds to the simulation's macroscopic temperature.

These equations can be extended to investigate the (NVT) canonical ensemble, where the number of particles, the system volume, and the temperature are held constant. However, because temperature is not automatically conserved by the Hamiltonian equations, the system conditions can change without a thermostat.

The simplest mechanism of regulating temperature is via velocity scaling. From *Equation 2.8* we can derive:

$$T = \sum_{i=1}^N \frac{m_i v_i^2}{k_b (3N - N_c)} \quad (2.9)$$

If, at time t , we multiply each particle's velocity by a factor λ , the contingent temperature change is given by:

$$\Delta T = \sum_{i=1}^N \frac{m_i (\lambda v_i)^2}{k_b (3N - N_c)} - \sum_{i=1}^N \frac{m_i v_i^2}{k_b (3N - N_c)} \quad (2.10)$$

Substituting *Equation 2.11* into *Equation 2.12*:

$$\Delta T = (\lambda^2 - 1)T(t) \quad (2.11)$$

Therefore, in order to scale to the temperature we require (T_0), λ must take a value of:

$$\lambda = \sqrt{T_0 / T(t)} \quad (2.12)$$

Multiplying the velocities by this λ factor every timestep is used in system equilibration at the start of a simulation in order to fix the temperature to T_0 . However, the method is unsuitable for the long-term timestep-by-timestep operation of the simulation because it works *too well*, damping down genuinely extant fluctuations in T which occur in the physical system because it has a finite time of thermal redistribution (i.e. heat conductivity).

To overcome this new problem we use a weaker form of temperature scaling, the Berendsen thermostat ^[74]. Here we link the MD particles to a fictitious heat bath at T_0 . Instead of indiscriminately locking the temperature of the system T to that of the heat bath, the magnitude of velocity scaling is itself scaled proportional to the difference between T (the instantaneous temperature) and T_0 (the desired equilibrium temperature) :

$$\frac{dT(t)}{dt} = \frac{1}{\tau} (T_0 - T(t)) \quad (2.13)$$

where τ is a ‘coupling parameter’, determining how strongly the system’s temperature is regulated by that of the heat bath. Equation 2.13 yields an exponential decay of the T towards T_0 , with the scaling factor given by:

$$\lambda = \sqrt{1 + \frac{dt}{\tau} \left[\frac{T_0}{T(t - \frac{1}{2}dt)} - 1 \right]} \quad (2.14)$$

δt is the length of the MD timestep. Taking T at $(t - \frac{1}{2}\delta t)$ rather than $T(t)$ comes from the use of the Verlet velocity leapfrog algorithm in the Berendsen thermostat, which integrates the molecular trajectories at half-timesteps (because interpolating the velocity in this way allows us to cancel out the third-order error in the Taylor expansion) ^[75]. The coupling parameter τ is used in practice as an empirical constant to control the amplitude of temperature fluctuations. At the limit of $\tau \rightarrow \infty$ the Berendsen thermostat is not actually active at all and the simulation is once again an NVE microcanonical ensemble; a very small value of τ conversely gives temperature oscillations which are non-physically small. If $\tau = \delta t$, equation 2.14 simplifies to:

$$\lambda = \sqrt{1 + \left[\frac{T_0}{T(t - \frac{1}{2}dt)} - 1 \right]} \quad (2.15)$$

which is the half-timestep equivalent of equation 2.12, where the Berendsen thermostat is equivalent to simple velocity rescaling.

In space, the physical icy grain *will* in fact heat up under gas deposition, as it is a thermally closed system surrounded by vacuum and has no easy way of dissipating the energy of adsorption. If we were simulating an entire grain (see *Section 5.2*) then it might be appropriate to operate with no thermostat at all, and allow the temperature to drift. However, the small system size of our simulations, in both volume and time, means this is not an appropriate treatment. We are modeling only the top few nanometers of the grain, and lower layers are taken to function as an effective heat sink to keep this surface at the (constant) temperature of the rest of the grain.

2.5 - Periodic boundary conditions and the minimum image convention

In order to remove unwanted edge effects, MD uses periodic boundary conditions whereby the simulation cell is repeated through space to form an infinite lattice of

identical cells. Any particles which move out of the volume of the cell are replaced by one of their periodic images moving *into* the cell from the opposite face (see *Figure 2.2*). Since the lattice repeats infinitely, each particle is in turn replicated an infinite number of times. Although this technique apparently introduces an infinite number of interactions, these can be scaled down to manageable finite levels by making further approximations.

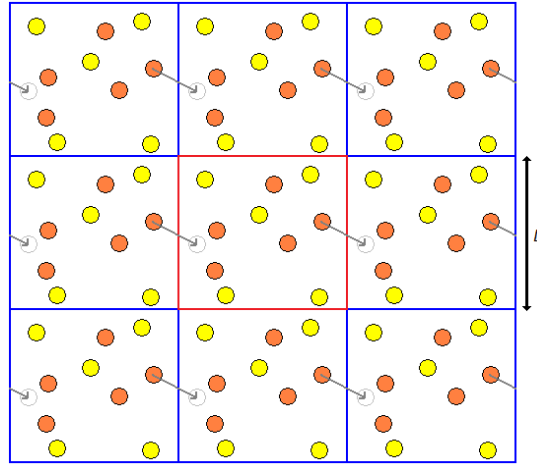


Figure 2.2: Illustration of the periodic boundary conditions applied to the simulation unit cell. A particle leaving the cell (in the red box) is replaced by the entry of its periodic image (from the blue image box on the left).

For interactions which become negligible on longer distance scales than half the length of the simulation cell, the *minimum image convention* can be applied (see *Figure 2.3*): when considering short-range interactions between particles i and j , only the effect of the nearest periodic image of j on i needs to be calculated, because the *next* nearest image of j will be at least half a box length away. Effectively the simulation unit cell is re-centered upon the particle for which forces are being calculated, and only those images which lie within the cube of side L centered upon the particle are considered; a ‘cubic truncation’. However, this does not lead to a isotropic cut-off distance r_c . For consistent force calculation we require a spherical truncation, so in fact a slightly smaller volume (that of a sphere with radius $< \frac{1}{2} L$) is surveyed.

The structural repetition introduced by image cells at the boundary condition, while not so problematic for crystalline systems which genuinely *do* repeat over moderate scales, represents an unphysical structure for ASW as it imposes periodicity on a

fundamentally aperiodic system. There is, however, no real alternative to using them that is *less* unrealistic. Only using larger basic simulation cell-lengths mitigates the effect of the boundaries; but with larger systems comes the increase in computing difficulty.

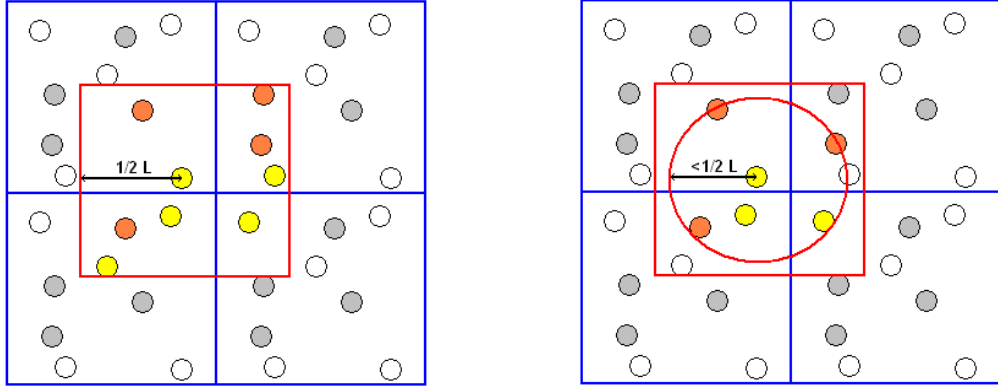


Figure 2.3: The minimum image convention (left), and the spherical truncation (right). If we sample atomic interactions at volumes greater than a cube of L^3 , we will begin double-counting interactions of atom pairs with atom pair images. As long as the box width $\frac{1}{2} L$ is longer than the distance over which short-range interactions becomes negligible, we can avoid this by only sampling a sphere of radius $< \frac{1}{2} L$, which massively reduces computing time while largely preserving the simulation accuracy.

2.6 - Long-range limitations of the minimum image convention

The minimum image convention cannot, however, easily approximate longer-ranged interactions like the electrostatic charge-charge interaction, which scales as r_{ij}^{-1} . The sum effect of long-range terms is treated through Ewald summation methods. The Ewald sum models charge i interacting with the charge j closest to it, *and also* all the images of charge j in other simulation cells. The surrounding simulation cells are arranged into a sphere, and the potential energy can be written as:

$$U^{Coul} = \frac{1}{2} \sum_{\mathbf{n}} \left[\sum_{i=1}^N \sum_{j=1}^N \frac{z_i z_j}{4\pi\epsilon_0} |\mathbf{r}_{ij} + \mathbf{n}|^{-1} \right] \quad (2.16)$$

where U is the energy, n is the box index, i and j are particle identities, and z is the particle charge. The sum over $\mathbf{n} = (n_x L, n_y L, n_z L)$, with n_x, n_y, n_z as integers up to

infinity, accounts for the charge-charge interactions outside the central unit cell. The prime on the sum indicates that the $i = j$ case is omitted for $n = 0$; that is, the central charge does not interact with itself. When $n \neq 0$, the $i = j$ case corresponds to i interacting with an image of itself in another cell.

Although this equation is exact in the limit of a very large number of boxes, it does not converge rapidly enough to be computationally useful. As such, the Ewald sum is split into two other summations that converge more quickly. The first is a neutralisation, where each point charge is screened by a Gaussian distribution of charge of opposite sign. These diffuse charges can be calculated as plane waves in reciprocal space, which are considerably easier to process. A second Gaussian distribution, of *opposite* sign to the first, is also included to cancel out this screening in the total energy term. The effect is shown in *Figure 2.4*:

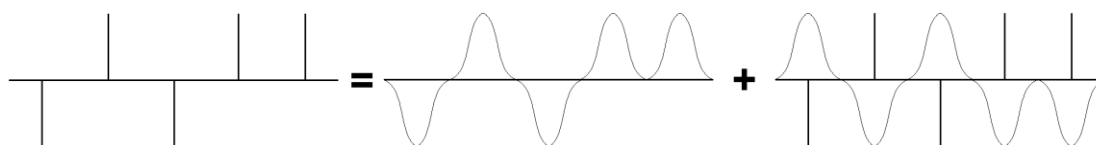


Figure 2.4: Illustration of the calculation of the energy of point charges in the Ewald sum. A series of point charges (left hand side) can be expressed as an (Ewald) sum of point charges and counterbalancing Gaussian curves (right hand side). This composite expression converges more rapidly.

The second summation defines the charge at the surface of the assembled sphere of simulation cells, and the total long-range Coulombic contribution to the energy is taken as the sum of these sums.

2.7 – Water in simulation

The simulation of water – at least under standard conditions – is a well-developed science. The most obvious difference in molecular dynamics models for water is whether they are *implicit* or *explicit*. In an explicit model, water molecules are expressed in the same qualitative manner as other molecules that might be present; that is, discrete H₂O entities with individually defined co-ordinate and velocity data, which move and interact according to the laws of classical mechanics (and/or

quantum mechanics, depending on the detail). This is not the case in an implicit model, which expresses water as a continuum. Continuum methods are useful in biochemical simulations, where the behaviour of water itself is not the focus of the study, and its relevance comes from the behaviour it induces in solute molecules. Mathematically, the influence of a water solvent's instantaneous configuration is approximately integrated out to give a reduced probability distribution which does not depend on solvent co-ordinates. This gives a "Potential Mean Force" which describes the average structure of the liquid. ^[76]

Conversely, *explicit* models generally approximate the water molecule as a rigid, triangular structure (see *Figure 2.5*). In general no intramolecular interactions are calculated; the intermolecular electrostatic interactions (between partial positive charges on Hs and partial negative charges on Os) are expressed through Coulomb's Law.

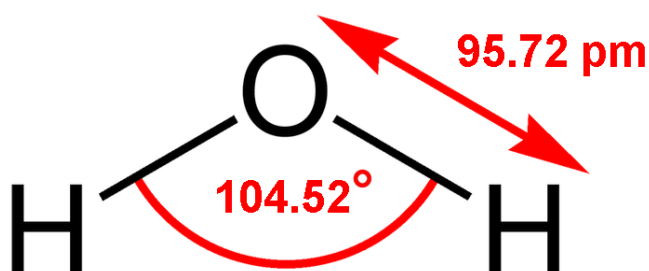


Figure 2.5: The basic geometry of the water molecule under the TIP4P model (see Section 2.8).

Higher-order dispersive forces are usually calculated only for oxygen-oxygen interactions, as the electron density at H is low enough that neglecting the deformation of the cloud at these sites scarcely reduces accuracy. These forces are expressed as a 12 – 6 Lennard-Jones potential (see *Section 2.1*; this potential is only rarely changed; one example is the NSPCE model ^[77]). It was discovered very early in simulations that charge values which exaggerate the gas-phase dipole moment are necessary to reproduce liquid water's physical properties. ^[78]

Parameterisation of the models involves assigning values to the various constants that appear in the energy equations; to control the distance-dependence of the attractive and repulsive forces such that computed properties match with experimental data. This process for models is often accomplished through trial and error^[79].

This method of working can make some simulations seem deceptively accurate. For example, the water models TIP4P, SPC/E, and DEC all return the physical density value of 0.997g.cm^{-3} for water under ambient conditions, but only because they have been parameterised specifically so that they reach this value.^[80]

Different explicit models use different parameters depending on precisely which experimental data it is most important to reproduce. For example, the basic TIP4P model gives the σ value in equation 2.1 as 3.15365\AA , whereas TIP4P/Ice, a different parameterisation which sacrifices physical reproducibility in the liquid to improve it in the crystalline solid, uses 3.16680\AA ^[81] (see *Section 2.8*). Since our investigation concerns an amorphous, glassy system (see *Section 1.6*), with an instantaneous structure most analogous to a fluid, our concern will be the ability to reproduce structural properties of liquid water.

Typically, water models adopt different methods of arranging the partial charge across the molecule. The most intuitive method is to place point charges on the atom sites (i.e. a 3-site model), but there are alternatives:

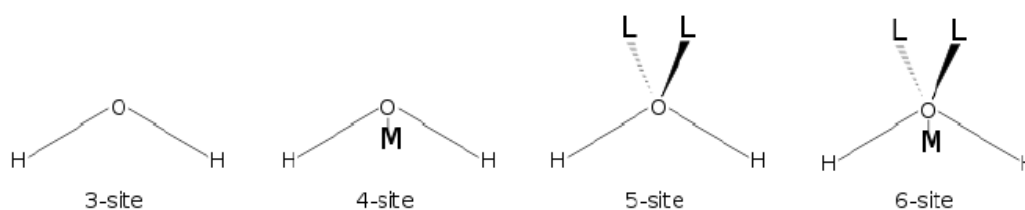


Figure 2.6: Schematic of multi-site water models. O and H represent oxygen and hydrogen atoms. The M site represents a displacement of the center of mass of the oxygen atom from its center of charge. L sites represent a partitioning of the oxygen charge over two separate lone-pair-like sites. Each additional site increases the number of computational processes the simulation has to perform each timestep.

The TIP4P 4-site method places oxygen's $-2q_H$ partial charge on a “dummy site” along the axis of symmetry. In reality, the partial charge on oxygen does not lie on the nucleus, but rather in a diffuse cloud in the molecule's center, and in this manner 4-site methods usually reproduce the bulk properties of water better than 3-site ones (although a notable exception is the very first 4-site model, Bernard-Fowler, which was inaccurate due to parameterisation difficulties ^[78]). 4-site structures tend to provide the best balance between computational efficiency and experimental reproducibility, and as such are the most popular water model.

5-site models follow the Valence Shell Electron Pair Repulsion paradigm of 2 lone pairs on the exterior of the oxygen ^[82]. When compared with 4-site models, the 5-site paradigm gives an improved geometry of hydrogen bonding which more accurately reproduces the Radial Distribution Function of liquid water as determined experimentally by neutron diffraction. It is, however, rather more computationally expensive, to the extent that the accuracy rarely justifies the cost. A six-site model incorporating all three dummy sites from both the 4 and 5 versions has also been developed, which reproduces the phase boundary of I_h and water more accurately. ^[83]

A halfway house between implicit and explicit simulation techniques comes in the form of coarse-graining. Here one attempts to describe the interactions in a system more simply; for example, by replacing the $3N$ atomic sites of N water molecules with N sites that represent whole water molecules (or, even more aggressively, a single site may represent a whole cluster of water molecules). Implementation of a coarse-grain paradigm requires code for this “mapping” step, where the atomistic configuration gets replaced by a reduced configuration; and also code to express the effective force field interactions between these ‘clunkier’ units. One-site course grained models of water can reproduce the liquid radial distribution function reasonably well (see *Section 3.3*), but give poor accuracy in thermodynamic properties. Furthermore, course-graining models do not explicitly deal with inter-water hydrogen bonding, which we anticipate to be important for the structures we consider.

Two-site models can improve the accurate modeling of thermodynamic properties as this allows the inclusion of a dipole. The calculated microscopic liquid structure, however, ends up resembling that of hydrogen fluoride.^[84]

Going in the opposite direction for more accuracy, some models introduce the flexibility of water by allowing intramolecular vibrations. This can be done either by supplementing an existing model with harmonic/anharmonic functions for bond length and angle (an approach adopted by SPC/F), or by defining an intramolecular potential so as to reproduce the value of the three vibrational modes (“central force” models). Flexible models often inaccurately predict a narrowing of the HOH bond in the liquid (104.5° gas phase to 100° condensed) due to molecular packing, whereas in reality the formation of a hydrogen bond network in the liquid redistributes the valence electrons around oxygen to open the bond angle slightly.^[80]

While the incorporation of flexibility in water models is clearly a theoretical improvement in bringing the operation of the simulation closer to the operation of reality, in practice almost all the advantages it brings can be recovered simply by re-parameterising the dipole of the rigid molecule, as in a 4-site model. So flexible water simulations are no more accurate than good rigid models, but yet involve significantly higher cost.

The same is true for models which attempt to explicitly include molecular polarizability (as opposed to simple LJ-oxygen-oxygen approximations). While such models do give much better values for the virial coefficients, other thermodynamic properties are again not significantly affected, in spite of the much more involved calculations.^[120]

A further level of complexity for water simulation is quantum chemistry MD calculations, which are the most ambitious and computationally intensive. Rather than approximating the dipole with dummy site charge centers, models such as TAB/10D use a self-consistent field description to determine the evolving charge distribution of bulk water over the course of an MD simulation, which formally accounts for electronic penetration effects and polarizability. Even more in-depth is *ab initio* calculation of water via Carr-Parinello MD, treating the electrons with density functional theory. This can only be used on systems of ~10 molecules due to

the computational complexity, and the results depend strongly on the exchange-correlation functional used. It is only these quantum models, however, which can describe to any degree the chemical differences between H₂O, D₂O, and T₂O. Indeed, the present classical MD models are most closely simulating T₂O from a qualitative standpoint, with quantum effects stemming from the low mass of H being accounted for only by parametric refinement. For example, entirely classical H₂O should have a ΔH_{vap} close to that of T₂O's 10.93kcal/mol, whereas SPC, RPOL, and the TIPS models are parameterised to reproduce the physical value of 10.52kcal/mol ^{[11][79]}.

Although the conditions under which astronomical ices act (very low temperatures and very long timescales) might *ex facie* suggest that quantum tunneling effects could become relevant, experimental and modeling work by Smith and Kay shows that for chemical vapour deposition ASW films, self-diffusion is essentially zero below 150K regardless of isotopic mix ^[85]. Although quantum tunneling is seen to exert an experimentally measurable inverse isotope effect on He diffusion inside H₂O-ASW compared to D₂O-ASW, this is not directly relevant to the present simulations, and is a minor effect unlikely to be detected in on a Molecular Dynamics timescale ^[86].

2.8 - TIP4P water models

We expect that the structures of amorphous ice to be largely dictated by the hydrogen bonding geometry of the molecules, and so on first consideration the use an explicit model with 5 or 6 sites might seem necessary. However, the >4 site models have significantly less underlying literature to confirm any parameterisations are accurate. At the same time, the computational cost of increasing the number of sites is undesirable (see *Section 2.2*). Finally, we know from previous computational studies ^{[87][88]} that 4-site models can adequately reproduce the bond lengths and angles of hydrogen-bonding in ices. As such, our simulations are conducted using TIP4P.

Based on the above considerations, fully classical 4-site models are used throughout this work. The most widely applied rigid 4-site model is TIP4P, which uses a HOH

angle of 104.52° and an OH distance of 0.9572Å. Although these properties remain fixed throughout all variants, TIP4P has in turn spawned a family of similar, alternately parameterised models to get the best results for the precise system to which they are being applied:

TIP4P-Ew, a version which uses Ewald sums (see *Section 2.4*) to treat long-range electrostatic interactions (rather than the standard TIP4P method of simply truncating interactions longer than a specified r) is able to qualitatively reproduce the entire water phase diagram of crystalline solid water below 1GPa^[89]. Referring to *Section 1.7*, however, our concern remains with the non-crystalline phase diagram, for which there has been much less work.

TIP4P/Ice is parameterised even more rigorously for the simulation of crystalline ices, having been developed precisely for the purpose of superseding normal TIP4P in this regard (which it does, replicating the 1 bar melting point to within 0.8 Kelvin (it returns 272.2K)).^[81]

TIP4P/2005, with a parameterisation based on a fit of the temperature of maximum density (indirectly estimated from the melting point of hexagonal ice), the stability of several ice polymorphs, and other commonly used target quantities^[90].

See *Chapter 3* for more information on comparisons between the models.

Model	qH (e)	ϵ (kJ mol ⁻¹)	σ (Å)	O-Q dist. (Å)
TIP4P	+0.5200	0.6480	3.15365	0.1500
TIP4P/Ew	+0.52422	0.680946	3.16435	0.1250
TIP4P/Ice	+0.5897	0.8822	3.16680	0.1577
TIP4P/2005	+0.5564	0.7749	3.15890	0.1546

Table 2.1: Properties of TIP4P parameterisations.^{[90][81][94][95]} qH is the charge on the hydrogen sites in units of e (1.602×10^{-19} C) – the oxygen charge site has exactly $-2qH$ for charge neutrality. ϵ and σ are the constants of the Lennard-Jones potential in equation 2.2. The O-Q distance is the displacement along the bisector of oxygen and its dummy charge site.

2.9 – Previous work in ASW simulation

Molecular Dynamics work has been conducted on analogous amorphous water ices before. Halabi (see *Section 1.7*, *Figure 1.15*^{[52][53][62]}), generating configurations for use in dissociation and adsorption studies, produced slabs of amorphous solid

through hyperquenching 300K liquid water – an unphysical method likely to produce HGW as opposed to astrochemically relevant ASW. Andersson et al. ^[96] do the same, though they admit that “[the ice] does not show the microporous structure that is obtained through the vapour deposition technique”, citing Kimmel’s ballistic deposition paper (see *Section 1.6*, ^[45]; also CO degassing from Fraser et. al. ^[55]). Zhang and Buch’s work ^[44] investigates ASW as gas-phase clusters, an unlikely occurrence in the ISM due to the kinetics of the gas/grain equilibrium and the scarcity of three-body collisions. Laboratory methods which work on similar systems generally grow ASW either through molecular beams or by introducing very diffuse water vapour to a cold plate (see Dulieu & Lemaire’s work, ^{[14][91]}), but both these methods are likely to deposit clusters of H₂O rather than individual molecules.

A study which is of direct relevance to the project – and the one from which our methodology evolves – is that of Essmann and Geiger ^[92], who simulated the deposition of water molecules by physical vapour deposition onto a flat silica substrate, returning a high-surface-area ice of intermediate LDA / HDA character (see *Section 1.6*). Their study used a simpler water model (three-site SPC/E) and a single deposition regime. In this work, discussed in *Chapter 3* and *Chapter 4*, we expand on the scope of previous investigations, varying the temperature and surface properties to reflect and compare ice growth under different astrophysical conditions.

An important consideration to make of many of these earlier works is that they were single-run studies. Computational capacity has increased tremendously in recent years, and while running multiple simulations would have been prohibitively expensive in terms of computing resources at the time many of these previous studies were conducted, today we have much more processing power available to us. Single-run studies are particularly limiting for studying non-equilibrium materials like amorphous ices, because we expect the final structures to be kinetically dependent on the chaotic initial conditions, rather than determined exclusively by the thermodynamic conditions. This is why our studies repeat each set of conditions 5 times; see *Table 3.4*.

There are various other computational studies of astronomical ASW growth which have been conducted using Monte Carlo simulation techniques, a probabilistic method where particles do not follow Newtonian trajectories but instead are rearranged semi-randomly dependent on energy minimization. We postpone our discussions of these until our comparisons in the results section, see especially *Section 4.7*.

2.10 – Summary

Chemical simulation via molecular dynamics applies Newton’s laws of motion to individual particles, integrating over time to generate particle trajectories. In order to constrain the number of interactions we have to model, and to negate surface effects, periodic boundary conditions and force cut-offs are applied.

There are a number of proposed models for water in simulation, ranging from continuum PMF methods to an explicit 6-site representation of each individual molecule. The 4-site model has proven itself to be the most practically workable in a variety of other analyses, so we use TIP4P for this project.

In the next chapter, we consider more specific aspects of our simulation: applying the general techniques explored in *Chapter 2* to the specific question of modeling astrochemical water deposition.

Chapter 3 – The New Model

3.1 – Overview

In this section, the details of the *in silico* experimental setup are described. The intention is to generate various amorphous solid water structures through physical vapour deposition, extending Essmann and Geiger’s methodology by using a more sophisticated force model, different temperatures, different substrates, and gathering better statistics. In this manner, deposited ices can be grown and analysed at a greater breadth of understanding than in previous studies.

As elaborated in *Section 3.6*, different temperatures of incoming water molecules are specified: 300K represents deposition conditions usually found in the laboratory. 150K is the estimated temperature of a typical shock wave which may induce water to freeze out onto grains. 10K, finally, is the low temperature at the core of a cloud. Likewise, the temperature of the substrate is maintained at alternately 10K (the equilibrated cold cloud temperature), 60K (the temperature used by Essmann and Geiger^[92]), and 130K (slightly lower than the temperature at which cubic ice forms preferentially over ASW). The temperature of the grain is known to exert a critical influence on both the exchange between the solid and gas ISM phases, as well as the character of chemical reactions which can take place^[22]. In addition to changes in temperature, hydrophobic and hydrophilic surfaces are tested, represented by silica and I_c respectively. The simulations are periodic in 2 dimensions, with the $+z$ -direction representing the near-vacuum of the ISM.

3.2 – Force limits

The essential constraints of our deposition simulation are informed by the work of Essmann and Geiger, who conducted a small-scale 1995 investigation on water deposition using a 3-site SPC model (see *Section 2.9*,^[92]). As in their study, we simulate the deposition of 500 water molecules one-by-one onto a pre-existing substrate. Studies of liquid water radial distribution functions have shown that

simulation cell lengths of at least 18Å prevent ‘size effects’ – artefacts of the cell-replicating periodic boundary conditions – from influencing the local environments of individual water molecules ^{[75][93]}. As in [92] we will use a cell length of roughly double this limit; ~36Å in the x and y directions, with the precise value determined by the unit cell dimensions of the substrate material. The z direction has no periodic boundary condition applied to it; the simulation in bulk is therefore effectively an infinite two-dimensional surface, on which water molecules may deposit.

Essmann and Geiger used a minimum image convention cut-off distance (r_{cut}) of 8.5Å. In order that our work simulates a more realistic system, we should use a value greater than this one, and less than the possible maximum of ½ boxlength, i.e. ~18Å. As a compromise between accuracy and efficiency, a value of 14Å is used throughout. The force cut-off is applied to both Coulomb and dispersive terms, and takes the form of a ‘cut-and-shifted’ potential: additional constant terms are applied to *Equation 2.1* such that the interaction energy reaches zero at r_{cut} .

$$U_{ij}(r_{ij}) = \frac{q_i q_j e^2}{r_{ij}} + \frac{q_i q_j e^2}{r_{cut}} + 4\epsilon_{ij} \left[\left(\frac{\sigma_{ij}}{r_{ij}} \right)^{12} - \left(\frac{\sigma_{ij}}{r_{ij}} \right)^6 \right] + 4\epsilon_{ij} \left[\left(\frac{\sigma_{ij}}{r_{cut}} \right)^{12} - \left(\frac{\sigma_{ij}}{r_{cut}} \right)^6 \right] \quad (3.1)$$

where U is the interaction energy, q the particle’s unit charge, e the electron charge, and σ and ϵ their Lennard-Jones values from *Figure 2.1* and *Table 3.2*. This form of the equation adds the interaction value at r_{cut} to the potential at every value of r , in order that the energy and the first derivative (though not the second derivative) of the energy remains continuous at r_{cut} . Keeping the potential continuous is essential for ensuring the conservation of thermodynamic properties in the system.

As demonstrated in *Figure 3.1*, the form of the potential is virtually unchanged because the *values* of the additive constants (and the corresponding interaction energies at r_{cut}) are in fact very small. For example, taking the parameters of the

TIP4P/2005 model from *Table 2.1*, the $\frac{q_i q_j e^2}{r_{cut}} + 4\epsilon_{ij} \left[\left(\frac{\sigma_{ij}}{r_{cut}} \right)^{12} - \left(\frac{\sigma_{ij}}{r_{cut}} \right)^6 \right]$ additional terms return a value of only 2.203×10^{-29} J for oxygen-oxygen interactions (counting both dispersive and electrostatic interactions, ignoring here the 0.1546Å displacement of the interaction sites). Contrasted with an ϵ LJ well-depth of

1.287×10^{-27} J, the effect of the cut-and-shift on the potential at intermediate distances is negligible, only increasing in importance as $r \rightarrow r_{cut}$.

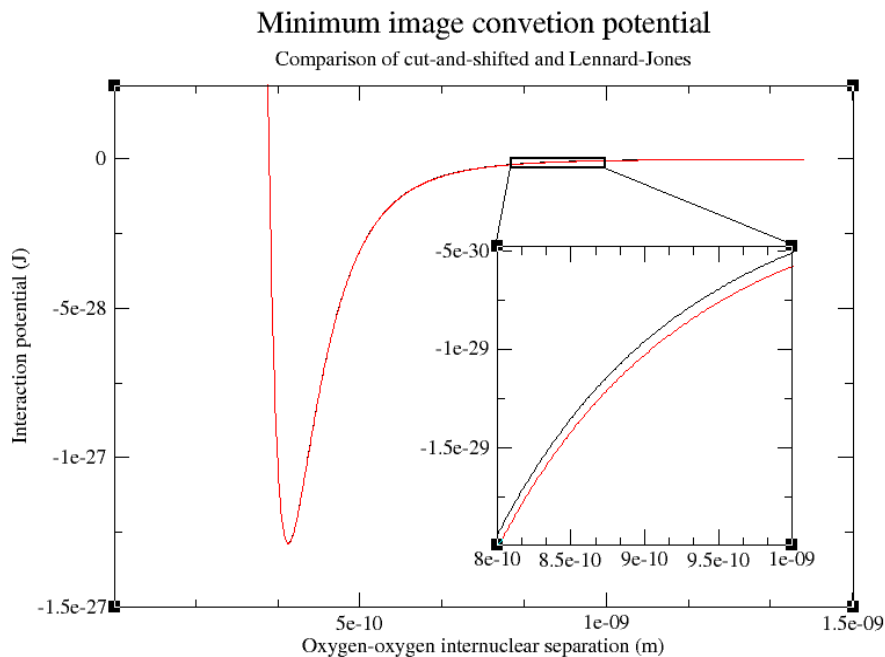


Figure 3.1: Near-coincidence of the cut and shifted LJ potential (equation 3.1, black) with the standard LJ potential (equation 2.2, red) for interaction of 2 oxygen sites using TIP4P/2005 parameters.

3.3 – Choosing a water model

The various TIP4P models elucidated in *Section 2.8* each have certain properties to recommend them for our specific purposes in this study, but in order to select the most appropriate form of the water molecule, each one was tested under the intended minimum image conventions of the cell. In order to avoid the dangers of self-fulfilling prophecy with parameterisation mentioned in *Section 2.7*, the models' suitability are tested by way of their ability to replicate the properties of liquid water under standard conditions. This has the added advantage that said properties are very well corroborated by experimental studies (unlike those of ASW, see *Section 1.7*). We will be paying particular attention to the radial distribution functions and

densities of the resultant simulations, as these are the principal properties by which the different forms of ASW are to be distinguished.

The model testing simulations are conducted with a 1536 water molecule cell with periodic copies in three dimensions. The water molecules are initially arranged in a cubic crystalline ice lattice, and the system is allowed to melt at 348K before being cooled to standard conditions. After 350,000 0.1-femtosecond timesteps (i.e. 35 ps), the average densities and radial distribution functions are collected:

Model	TIP4P	TIP4P/Ew	TIP4P/Ice	TIP4P/2005
Volume (\AA^3)	46416	46261	46379	46122
1st rdf peak (\AA)	2.76	2.76	2.76	2.76
1st peak intensity	2.96	3.13	3.43	3.21
2nd rdf peak (\AA)	4.43	4.38	4.43	4.48
2nd peak intensity	1.10	1.13	1.18	1.14

Table 3.1: Results of TIP4P model tests for oxygen-oxygen separations. Volumes are calculated disregarding the first 50,000 steps of a 350,000 step run. Radial distribution functions are taken from particle positions at every 100 steps. Intensities are normalised such that ‘bulk’ intensity as $r \rightarrow \infty$ is unity.

The experimental volume of water under standard conditions is 997.77 kg.m^{-3} ; accordingly, 1536 molecules (mass $4.5909 \cdot 10^{-23} \text{ kg}$) should occupy $4.601 \cdot 10^{-23} \text{ m}^3$ (see *Figure 3.2*). The first and second radial distribution peaks are in reality found at ~ 2.75 and ~ 4.49 respectively (via neutron ^[97] and x-ray diffraction ^[98] experiments), with peak intensities of ~ 2.21 and ~ 1.15 (different methodologies report different results).

There is very little variation in the values returned from the radial distribution functions from each model (see *Figure 3.3*); the only minor outlier is TIP4P/Ice, which is not intended to be as accurate for standard conditions liquid water, as it is parameterised for rigour in the crystalline solid phase instead. The density profiles also differ by only 0.6% at maximum as well. While the differences were not altogether significant, TIP4P/2005 was found to be slightly more accurate for three of the values: density, 2nd peak intensity, and 2nd peak position, while jointly leading in 1st peak position. Consequently, TIP4P/2005 is the model chosen for the main deposition simulations in the remainder of the work.

Volume equilibration of water models

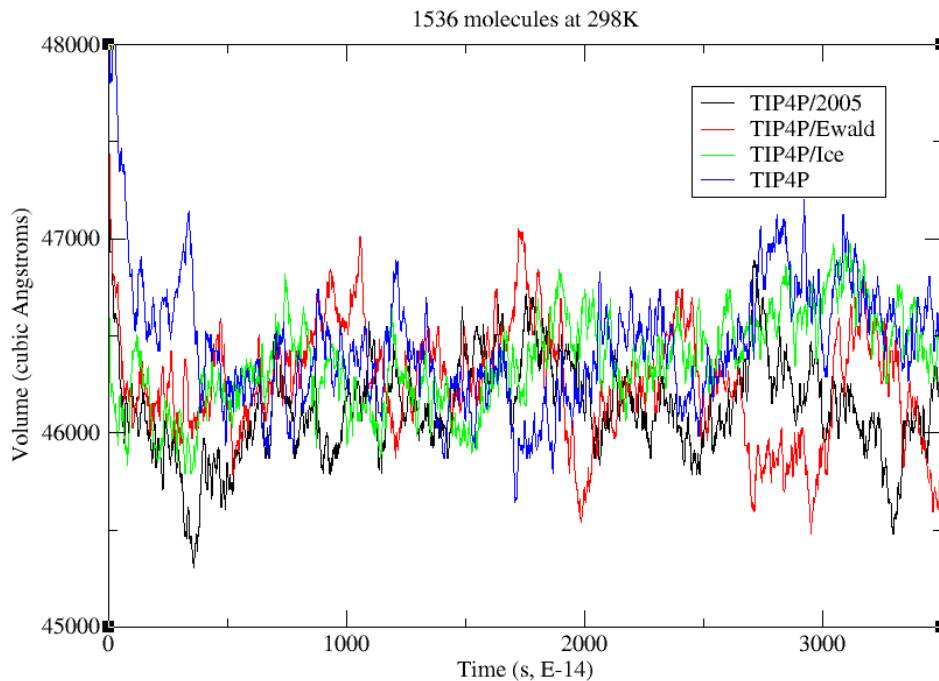


Figure 3.2: Volume occupancy of water models (298K, NPT ensemble) plotting the equilibration of the simulation cell dimensions with time. The model contracts on start-up, reducing in volume from a maximum of $\sim 48,000 \text{ \AA}^3$ for TIP4P/2005 to around $46,100 \text{ \AA}^3$, which is close to the experimental value.

Radial distribution functions of water models

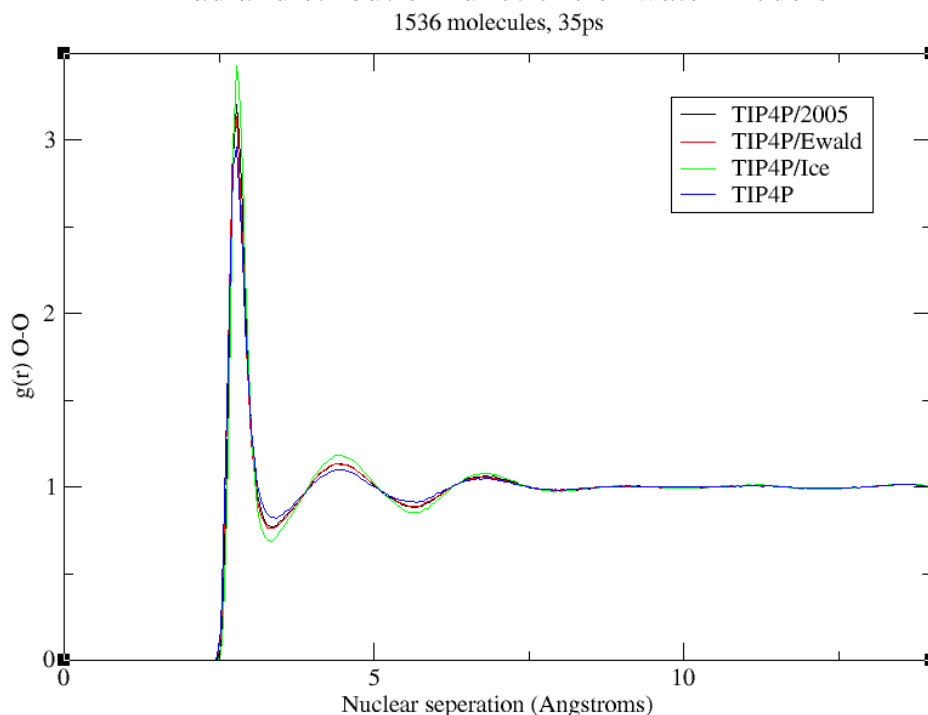


Figure 3.3: Oxygen-oxygen radial distribution functions of water models (298K, NPT ensemble) normalised about the long-range tail.

3.4 – Creating the silica substrate

Our interest is in modeling the deposition of water molecules on a surface simulating the dust grains of the interstellar medium (see *Section 1.2*). Two different kinds of substrate are to be modeled: a silicon dioxide surface representing a ‘naked’ dust grain on which water is just beginning to deposit; and a crystalline water ice surface for a grain which has already accrued a partial mantle of water.

For the silicon surface we use the same model as in the Essmann and Geiger study ^[92]. Silicon dioxide is modeled using a cluster method where the SiO₂ unit is represented by a single charge-neutral Lennard-Jones site. Although this raises questions of accuracy (surface hydroxyl groups – below the granular resolution of the cluster model - may be important for equilibration of water on silica ^[99]), with this formulation we can take the silica results as representative of hydrophobic substrates in general, rather than reducing our computational efficiency to rigorously calculate complex and specific silica-water interactions.

The LJ parameters used for silicon dioxide’s interactions (along with the TIP4P/2005 oxygen/oxygen interactions) are:

Interaction	ϵ (kJ mol⁻¹)	σ (Å)
Silica/Silica	5.7632	2.8000
Silica/Oxygen	2.1133	2.9790
Oxygen/Oxygen	0.7749	3.1589

Table 3.2: SiO₂ cluster unit Lennard-Jones interaction parameters.

To generate the surface, a 1400 particle cell of hexagonal close packed silica was generated with periodic images in three dimensions. The cell lengths of x 30.41Å, y 30.41Å, and z 28.20Å are chosen so as to conform to the desired specifications of the deposition simulations (see *Section 3.2*). The cell was allowed to relax under conditions relevant to the interior of a cold cloud – 10K and zero applied pressure – in an NPT ensemble for 350,000 timesteps of 0.1 femtoseconds, producing a silica

with hexagonal close packed structure inside a simulation cell of dimensions $x = 31.94\text{\AA}$, $y = 31.94\text{\AA}$, $z = 29.62\text{\AA}$.

Slicing the silica along a $[1,1,1]$ plane produced a 1020\AA^2 slab of 300 SiO_2 molecules, which is to be used as our periodic surface. The slab consists of three layers of silica, each containing 100 molecules. In order to keep the surface level and anchor it in the right place, the lowest layer is ‘frozen’, with their velocities fixed at 0 during every step of the deposition simulation and thus rendering them unable to move from their starting lattice sites. The upper two levels are free to librate, their positions maintained simply by the interactions with their neighbours. This keeps the slab anchored in the simulation box.

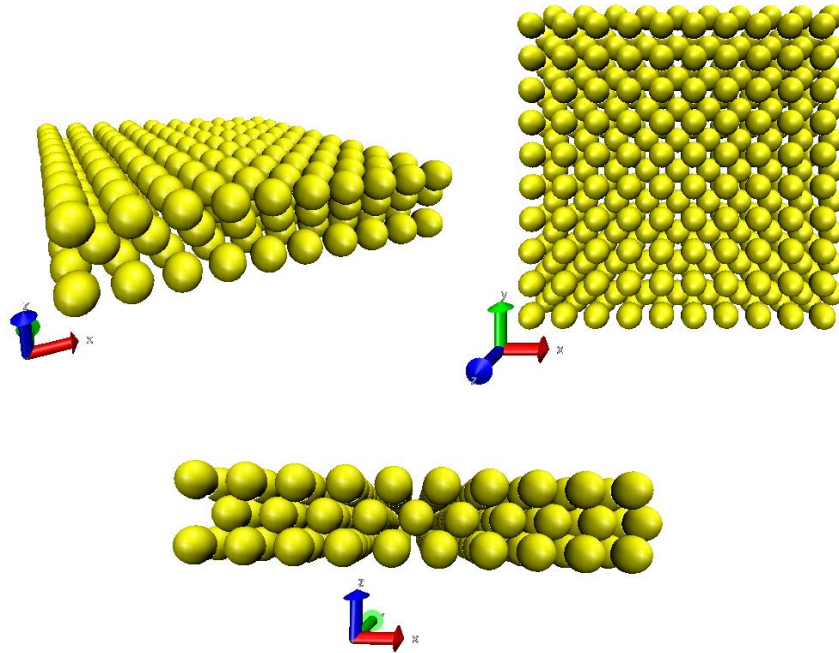


Figure 3.4: The 300-particle silica surface viewed (top right) down the z axis, (bottom) down the y axis, and (top left) with a perspective view. This and other MD visualization figures produced using Visual Molecular Dynamics [100]

Although the grain surface in interstellar space – and in the lab – is expected to be disordered, with dislocations and steps, defining a specific degree of ‘surface roughness’ would introduce an additional confounding variable into our work. We persevere with the flat surface of Essmann and Geiger ^[92], so as to observe the structures which self-assemble, rather than potentially template themselves to an

arrangement already induced by the specific irregularities of a given substrate configuration.

3.5 – Creating the water substrate

The cubic ice substrate requires more involved considerations. While proton ordered ice is trivial to generate in simulation, proton-disordered ice – as found in nature ^[101] - presents more of a challenge as it cannot simply be abstracted from unit cell replication.

Ideal crystalline ice is expected to follow the Bernal–Fowler ice rules, which describe the arrangement of hydrogen atoms in the solid (see *Section 1.5*). The rules are as follows:

- Each water molecule is oriented such that its two hydrogen atoms are directed approximately toward two of the four surrounding oxygen atoms (arranged almost in a tetrahedron)
- Only one hydrogen atom is present on each O-O linkage
- Each oxygen atom has two nearest neighboring hydrogen atoms such that the water molecule structure is preserved.

Proton-disordered ices still conform to the Bernal-Fowler rules, but they exhibit orientational disorder in hydrogen direction, which contributes a residual entropy in I_c of $3.4 \pm 0.2 \text{ J K}^{-1} \text{ mol}^{-1}$ at 0K ^[102], deviating from the third law of thermodynamics. This entropy arises because, for a given H_2O oxygen atom on an I_c (or I_h) lattice site, there are four available sites for a hydrogen atom to occupy. With two hydrogens per water molecule this leads to six orientations in principle allowed under the ice rules. Although an individual water on an individual lattice site will have its allowed orientation dictated to it by the orientations of its four nearest neighbours, the internal orientations of a given cluster of molecules are not obligated to follow any systemic motif in order to conform with the ice rules.

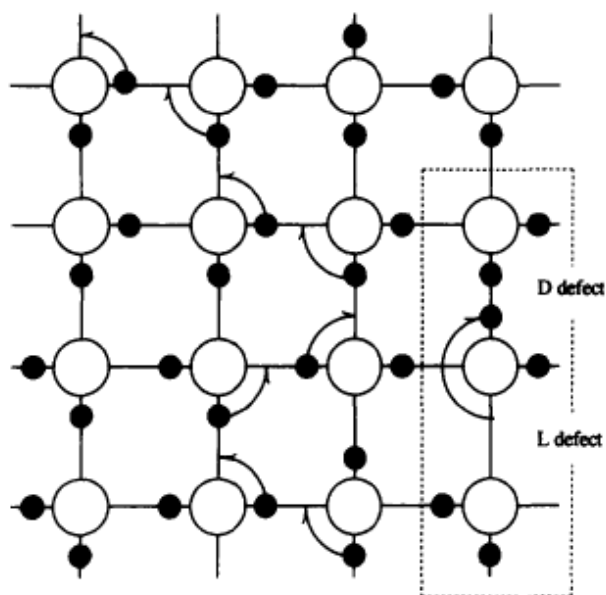


Figure 3.5: 2D representation of ice proton disorder and defect migration. Reproduced from [101].

Additional disorder can derive from the fact that, as shown in Figure 3.5, the ice rules are in fact violable – indeed, it is violations that produce ice’s electrical conductivity and dielectric relaxation, where some of the water dipoles can respond to an external AC electric field with an appropriate frequency ^[101]. These effects are believed to derive from a violation of the second Bernal-Fowler rule through a kind of “orientational defect” lattice fault known as a Bjerrum defect. These occur in pairs when a water molecule rotates out of position, producing a D (*doppelt* in German) and L (*leer*) defect. The former has two protons in a hydrogen bond, while the latter contains none. The number of orientational defects is, however, quite small (around one in every 10^{12} H-bonds at 200K) and decreases exponentially on lowering the temperature ^[102].

Our method of arriving at a proton-disordered substrate initially requires the generation of a proton-ordered lattice. Proton-ordered cubic ice can be manufactured in simulation through essentially the same method as produced the silica surface: a unit cell of TIP4P/2005 cubic ice is generated in simulation and then replicated to produce a 1152 molecule cell of cubic close packed water ice with periodic images in

three dimensions. The cell lengths are $x = 36.18\text{\AA}$, $y = 31.34\text{\AA}$, and $z = 44.32\text{\AA}$, again comparable to our desired *Section 3.2* dimensions.

In order to create a proton-disordered grain surface, we then adapt the ‘worm-algorithm’ approach of Rahman and Stillinger^[103], which has been shown by other studies^[104] to successfully reproduce the experimental configurational entropies of proton disorder. The approach begins by generating a topological representation of hydrogen bond network ice lattice, with oxygens occupying the correct lattice sites and serving as nodes, while the hydrogen bonds serve as the connections between them. Vector annotations are added to the h-bonds to record which way the bond is pointing (i.e. which of the two connected oxygens possesses the O-H bond covalent bond). At the start, then, the vectors correspond to those of our simple proton-ordered ice.

Next, we generate random walk paths along the hydrogen bond network. Where the random walks intersect with themselves, all hydrogen bonds along the closed loop have their directions flipped, so an intramolecular O-H covalent bond becomes an intermolecular O \cdots H hydrogen bond and vice-versa. It is only those waters within the closed loop which have their h-bonding network directions reversed, *not* all waters within the whole random walk. Because we only invert the bonding around a closed loop, each involved oxygen loses an incoming hydrogen bond, but also gains a new one by the transfiguration of a previously outgoing bond, so the ice rules remain satisfied.

The periodic boundary conditions of the cell increase the complexity of the algorithm; while the walk can cross cell boundaries, it should not curtail by forming a ‘loop’ with a periodic image of itself. Curtailing in such a manner actually forms an infinite line rather than a closed loop (due to the infinite periodicity of the cell images), and this can lead to a net dipole moment in the cell^[105]. As shown in *Figure 3.6*, we discard random walks of this nature.

The worm algorithm is run for 10^6 sequential walks through the 1152-molecule ice block, by repetition removing any vestige of the original proton ordering. By this mechanism we produce a proton *disordered* network representation of the H-

bonding. Once the worm algorithm has finished, Cartesian proton positions are mapped back onto the vector representations. The ice is then allowed to relax for 250,000 timesteps (25 ps) to equilibrate under its new structure.

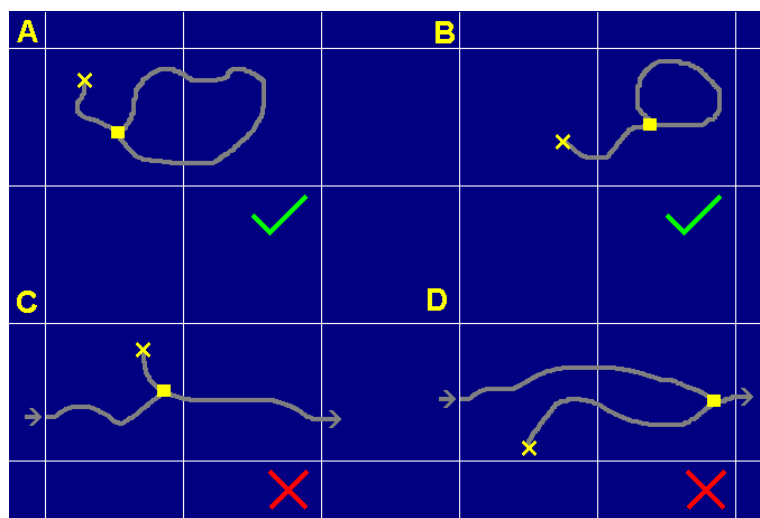


Figure 3.6: 2D representations of allowed and disallowed walks under the Rahman-Stillinger worm algorithm. Each box represents a $\sim 36\text{\AA}$ simulation cell image.

***A:** The random walk takes the path into an adjacent image cell, but then re-enters the origin cell and intersects. This walk is allowed.*

***B:** The random walk takes the path into an adjacent image cell, and intersects with itself in the image cell. This walk is allowed.*

***C:** The algorithm crosses over cell boundaries in two different image cells before intersecting with an image of itself in the original cell. This walk is not allowed.*

***D:** The algorithm crosses over cell boundaries in three different image cells before intersecting with an image of itself outside the original cell. This walk is not allowed.*

As with the silica block in Section 3.4, the ice cell is then sliced along a $[1,1,1]$ plane to produce a ‘triple bilayer’ I_c substrate of 384 molecules, with a surface area of 977\AA^2 . Again, the particles of the lowest bilayer are frozen in place to act as an anchor, while the upper 256 waters are free to vibrate.

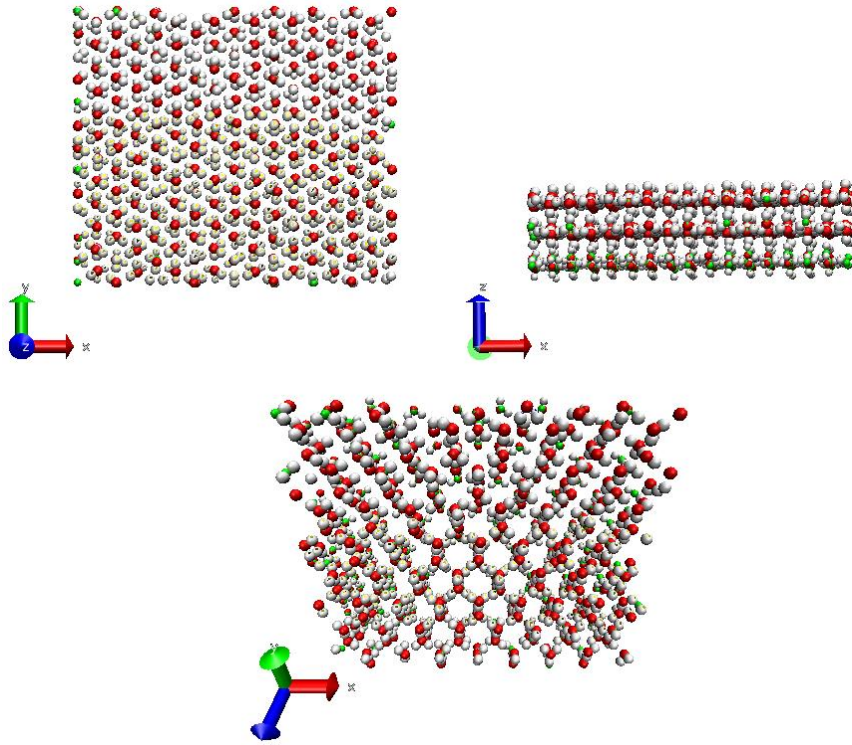


Figure 3.7: The 384-molecule cubic water ice surface viewed (top left) down the z axis, (top right) down the y axis, and (bottom) with a perspective view. Red spheres are oxygen, white spheres are hydrogen, and green spheres are the dummy “ Q ” charge sites.

3.6 – Creating the incident water

Although the temperature within the cold cores of molecular clouds can reach lows of around 10K (see *Section 1.3*), the extremely diffuse nature of the ISM means that clouds are not expected to attain a homogeneous temperature, as interparticle collisions occur at too low a rate to allow bulk thermal equilibration, even over millions of years. Water molecules incoming to the grain surface, then, may do so with a variety of kinetic energies.

In the deposition studies we intend to use three different incoming molecule temperatures: 10, 150, and 300K. The root mean square speed of a molecule is given in kinetic theory as:

$$c_i = \sqrt{\frac{3RT}{M}} \quad (3.2)$$

$$c_x^2 + c_y^2 + c_z^2 = c_t^2 = 3c_z^2 \quad (3.3)$$

where R is the gas constant, T is the temperature, and M is the molar mass in kg. The root mean square speed c_t is composed of c_x , c_y , and c_z components, which, provided no bulk movement is occurring, are assumed to be equal. Consequently we anticipate the following properties of incoming molecules at these temperatures:

Temp. (K)	rms speed (m.s ⁻¹)	z-axis rms speed (m.s ⁻¹)	z-axis rms K.E. (J*10 ⁻²²)	z-axis momentum (kg.m.s ⁻¹ *10 ⁻²⁴)
10	117.72	67.96	0.69	2.03
150	455.92	263.22	10.35	7.87
300	644.77	372.26	20.71	11.12

Table 3.3: Root mean square properties over all trajectories and on projection down the z-axis. All directions of motion are considered equally probable. Water's mass taken as $18 \times 1.66054 \times 10^{-27}$ kg, i.e. 18u.

Molecules at a given temperature can be generated automatically by the simulation, which assigns them speeds according to a Maxwell-Boltzmann distribution around the stipulated value, along a random vector.

When incoming water molecules are being generated for the deposition simulation, we require that they have a random starting position in the simulation cell, and a random trajectory with the caveat that their z-velocity must be directed towards the substrate. The procedure adopted is to run a 1152-molecule TIP4P/2005 simulation at the desired temperature, where all intermolecular forces are turned off. At the beginning of the simulation, the waters are automatically thermalised by the program, and a run of arbitrary length can be conducted (because no forces have to be calculated by *Equation 3.1*; r_{cut} is effectively 0, so the principal limitation on speed simply becomes the read / write updating of co-ordinates each timestep) to scramble the particle positions over the whole of the image cell. The lack of force interactions mimics the extremely diffuse environments that the incoming molecules would genuinely experience in the ISM.

3.7 – Combining for deposition

After no fewer than 10^6 tenth-femtosecond timesteps, a molecule is selected at random from the 1152-particle gas phase simulation for transfer into the combined substrate + incident water deposition simulation. The co-ordinates of the oxygen atom are scaled as (b_s/b_g) , where b_s and b_g are the appropriate box lengths in the substrate and gas cells, while the relative positions of the H and Q substituents are preserved. After checking for correct conservation of bond length across all twelve periodic cell boundaries (6 from each of the incoming and outgoing cells), the z position of the oxygen atom is set at 15\AA above that of highest molecule in the deposition simulation; that is, just beyond the 14\AA force cut-off radius as stipulated in *Section 3.2*, thereby ensuring that we do not subject the simulation to abrupt discontinuous interaction energy changes as we introduce the new molecule. For the first incoming water molecule introduced to the deposition, then, this starts it at 15\AA above the topmost layer of the substrate.

The linear z -momentum of the incoming molecule is given by:

$$p_{H_2O} = \sum_{i=1}^4 m_i v_i = 16u.v_O + 1u.v_{H1} + 1u.v_{H2} + 0u.v_Q \quad (3.4)$$

and this property is checked to ensure the center-of-mass is travelling downwards. If it is not, the atoms' velocities are simply reflected in the xy -plane such that the center of mass now *is* on a trajectory towards the substrate. x and y velocities go unchanged, so in this way the incoming molecule is permitted to any kinetic energy along any negative v_z vector.

After the new water molecule is introduced to the simulation, it is allowed to descend for 2.5ps (5,000 0.5-femtosecond timesteps). The routine then checks to see whether the molecule has accommodated with the surface or not, the criteria being that it has descended at least 15\AA *and* that there is at least one intermolecular bonding interaction associated with it (see *Section 4.7*). If it not, the sequence repeats to a maximum of 10ps (20,000 timesteps). A successful deposition is followed by a 3ps equilibration period in order to allow the solid to relax with the new particle addition, after which the next new molecule is inserted. An unsuccessful deposition sees the

errant water molecule deleted wholesale from the simulation, and a replacement is inserted.

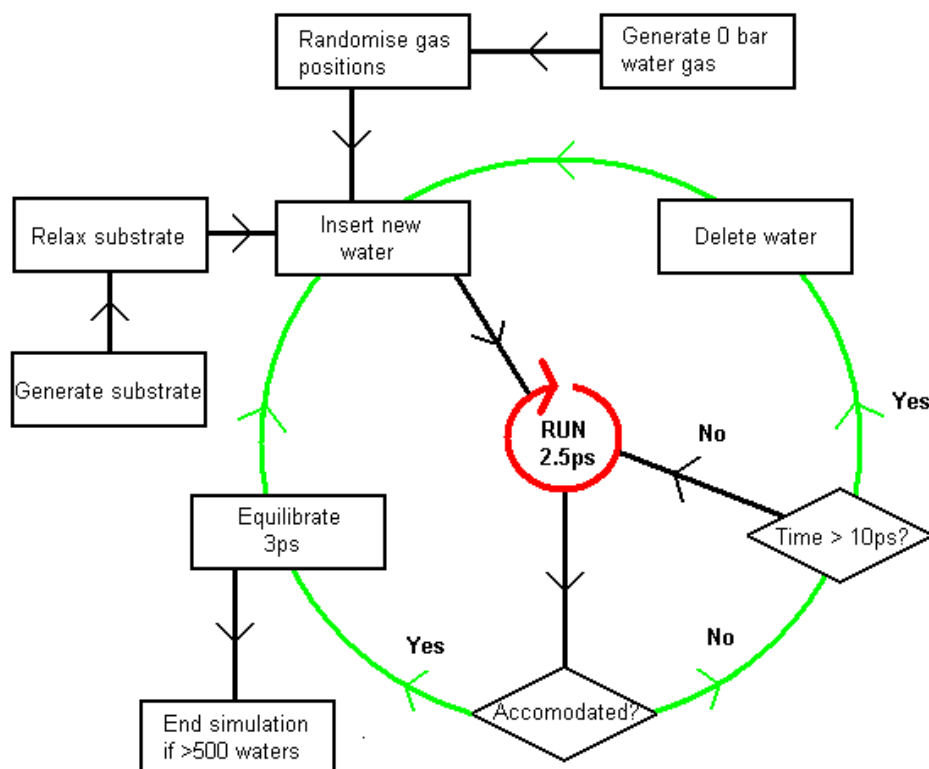


Figure 3.8: Flowchart detailing the main features in the deposition methodology. The red circle is the main molecular dynamics cycle; the green circle is the automated framework of checks and molecule insertions which takes place around the principal force integration loop.

This simulation methodology evolved gradually from test runs, and incorporates a variety of features. The technique of checking for deposition every 2.5ps, for example, adds the additional overhead of exiting the MD loop, analysing the co-ordinate files for the break parameter, and then returning to the MD loop if it is not found. So this does make the simulation less efficient if the deposition is taking a long time. However, in cases where the incoming molecule has descended and accommodated quickly it allows the main MD loop – the most time-consuming element of the methodology by several orders of magnitude – to finish a maximum of 75% faster, and therefore on aggregate makes the program more time-efficient.

The major justification for the potential deletion of ‘failed’ deposition molecules is explained in *Section 4.8*; however, a secondary rationale can be deduced *a priori*

from the kinetic considerations of *Section 3.6*. Because the randomly selected insertion molecule may have a z -component velocity of any value, this may in some cases prove itself to be a value too small to reach the substrate in a timely manner. In order to deposit within the allotted 10ps, the molecule has to descend approximately 15Å; a ‘grace’ distance of 5Å is allowed, reducing the limit to 10Å. Proper deposition potentially requires even more than 15Å, if the surface is non-uniform (such that the z co-ordinate of the topmost molecule differs significantly from the z co-ordinate of the average molecule). This means that the incoming water’s z -velocity must, at a crude first approximation, be at least 10ms^{-1} (although in fact we expect the molecules to accelerate as they fall into the surface’s potential well - see again *Section 4.8*— so *some* lower velocities will also successfully deposit). With reference to *Table 3.3*, 10ms^{-1} is less than one tenth of the average z -velocity expected of even the slowest, 10K deposition; however, the Maxwell-Boltzmann distribution guarantees a proportion of molecules possessing both significantly higher and significantly lower linear speeds than this; so, inevitably, a fundamentally arbitrary 10ps cut-off will discard some legitimate depositing molecules. However, if the simulation has the ill-fortune to select for insertion a water molecule with only infinitesimal z -velocity, the time taken for the particle to cross even the 14Å force cut-off threshold would be prohibitively high for the deposition’s timely completion. The *a priori* reason, then, for instituting such a cut-off is simply a matter of the *Section 2.2* compromise between efficiency and accuracy.

The actual proportion of molecules expected to be discarded in a 10K deposition regime can be calculated as follows:

The formula for the volume of a segment of a sphere is:

$$V_{seg} = \frac{1}{3}\pi h^2(3R - h) \quad (3.5)$$

where h is the height of the segment (here $117.72 - 10.0 = 107.72 \text{ ms}^{-1}$) and R is the sphere’s total radius (117.72 ms^{-1}). The total volume of the hemisphere in $(\text{ms}^{-1})^3$, $\frac{1}{2}(\frac{4}{3}\pi R^3)$, is 3416720, while V_{seg} calculates as 2982405. This gives us a proportion of 10K molecules we expect to have a permissible trajectory as 87.28%; i.e. around 13% of the trajectories will be rejected.

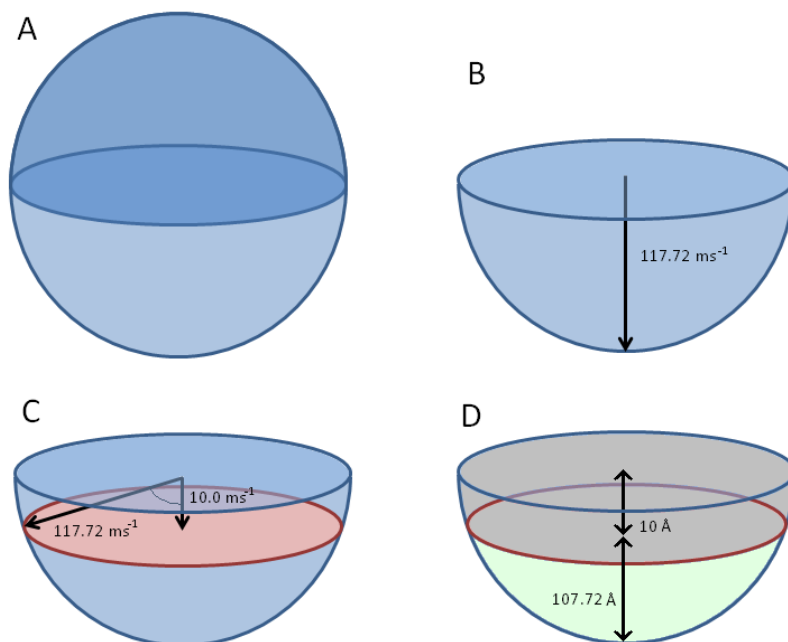


Figure 3.9: Cutoff proportion calculation. All numbers relate to an average 10K depositing molecule with a root mean square speed of 117.72 ms^{-1} .

A: A given water molecule in the gas phase simulation may be travelling along any vector. The $+z$ vectors are reflected, giving:

B: A hemisphere of possible trajectories with average magnitude 117.72 ms^{-1} .

C: In order to reach the substrate before the time cutoff, the molecule must have a $-z$ velocity component of at least 15 ms^{-1} ; the 5 \AA grace distance reduces this to 10 ms^{-1} .

D: This means there is a section of the velocity hemisphere (in grey) where the molecule will not reach the substrate in time.

3.8 – Summary

Of the available 4-site TIP4P water models tested, the TIP4P/2005 parameterisation was found to perform slightly better under our simulation cell size. Substrates, generated for the water to deposit on, are composed of three layers of particles (coarse-grained silica or TIP4P/2005 water) of which the lowest layer is fixed in place to provide an ‘anchor’ for the slab. The water layers were made proton-disordered by application of a bond-flipping loop algorithm. The deposition cycle itself is described as a loop of molecule-position checks and equilibration steps around the main force-integrator MD core loop.

<u>Comparison with Essmann & Geiger Methodology</u>		
<u>Property</u>	<u>Our simulations</u>	<u>Essmann & Geiger</u>
Deposition temperature	10K, 150K, 300K	60K
Substrate temperature	10K, 60K, 130K	60K
Substrate material	Cubic ice, silica	Silica
Pairwise force cutoff	14Å	8.5Å
MD timestep	5E-16 s	2E-15 s
Deposition frequency	0.077 to 0.182 molecule.ps-1	0.25 molecule.ps-1
Surface area	Silica: 1020Å ² , Ice: 977Å ²	484Å ²
Number of depositions	500	500
Water model	3-site SPC/E	4-site TIP4P/2005
Number of simulations	5 for each of 18 conditions	1

Table 3.4: Our methodology compared to Essmann & Geiger's.

This methodology updates and expands the Essmann & Geiger study by sampling more temperatures and materials, with lower deposition rates, larger surface areas, and a more accurate, longer-range force model. We also run a total of 90 simulations compared to the original 1, in order to get a more statistically rigorous collection of results.

Chapter 4 – Results

4.1 – Overview

At the end of the simulation runs, 90 separate ASW structures were generated: all combinations of 10K, 60K, 130K substrate temperature with 10K, 150K, 300K incoming water temperature and silica or cubic ice substrate, which gives 18 distinct regimes, within each of which 5 independent runs were completed. These runs differ only in the trajectories of their incoming molecules, selected randomly from the appropriately thermalised gas simulation (see *Section 3.6*).

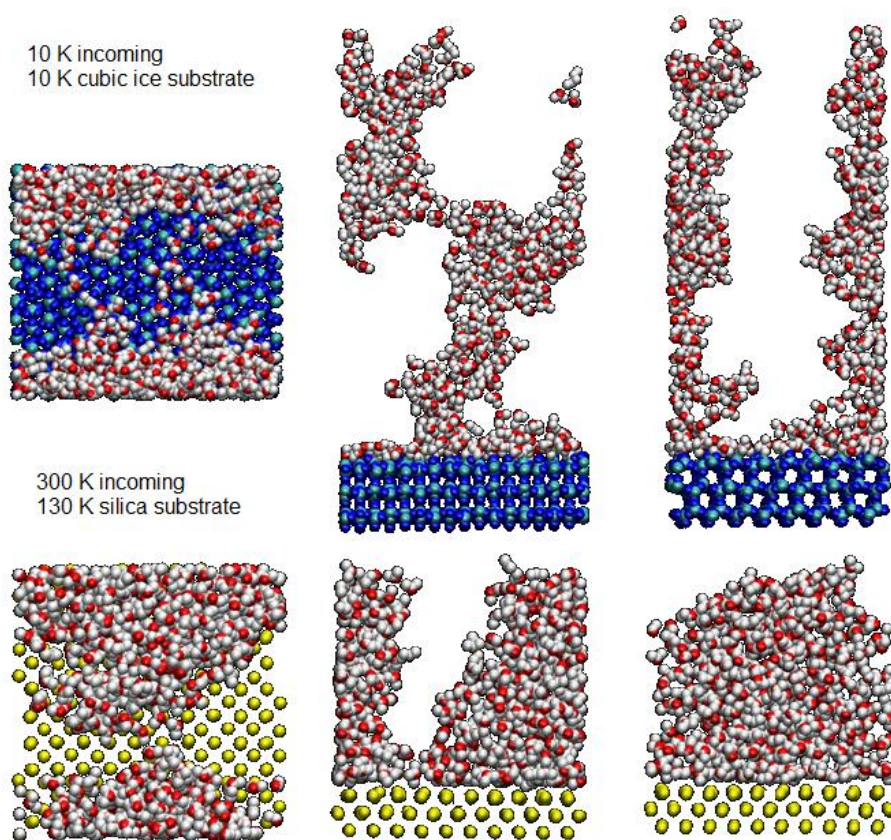


*Figure 4.1: Examples of the ASW ice structures formed from these simulations, seen along the z , y , and x axes. Recall from *Section 2.5* that 2D molecular dynamics periodic boundary conditions are in effect, so in fact these unit cells are replicated across space in the x and y directions. Blue-green particles are part of the pre-existing cubic ice substrate; yellow molecules are coarse-grained SiO_2 particles; red-white particles are deposited water.*

Significant differences in the kinds of structures formed can be observed for changes in deposition temperature, with more subtle effects detected as arising from surface temperature and substrate molecule (see especially *Figures 4.1, 4.7, 4.8*). Our analysis codes quantify the height of structures produced, their volumes, the proportion of the grain surface which they occlude, and the preferred orientations in which they deposit. Growth modes are inferred based on the data, and the astrochemical ramifications discussed.

Various properties of the grown ice structures were extracted from the simulations for discussion. *Static* results (see *Section 4.3*) refer to the properties of the final structures, after the 500 deposition events have completed. *Dynamic* results (see *Section 4.4*) refer to the growth process itself during the course of the deposition. Results in both sections are given as the average statistics for five runs under each of the 18 sets of conditions.

The generation of the structures themselves produces some unexpected effects, notably an effective nonzero sticking probability as discussed in *Section 4.8*. Combined with the arguments in *Section 3.7* this means that the number of particles inserted does not equal the number of water molecules in the deposited structure. On account of these effects, in the subsequent results we report “Number of deposition attempts” to keep track of the rate of structure build-up.

4.2 – Methodologies and averages for static results

Analysed static properties – those deriving exclusively from the final structures after 500 depositions, as opposed to intermediate points – are as follows:

Structure height: The z-axis position of the oxygen atom within topmost water molecule in the ice structure, with 0 being the average absolute z-position of the topmost layer of substrate (i.e. 100 SiO₂ particles in the silica surface, 128 oxygen atoms in the I_c substrate; same criterion used for other heights below).

Median height: The z-axis position of the 251st-highest deposited water oxygen.

Average height: The average z-axis position of a deposited water oxygen.

Surface relaxation: The difference in z-axis position between the surface at the commencement of the simulation and the surface at the end of the simulation; to detect surface rearrangement if it occurs.

Surface occlusion: Viewing the substrate from directly above, surface occlusion describes the proportion of the substrate surface area which is obscured by deposited molecules. It is related to the more conventional surface coverage, though occlusion is preferred because a surface site may be *blocked* despite being *unoccupied* due to surface-level cavitations or the formation of overhanging structures (see rain shadows, *Figure 1.11*).

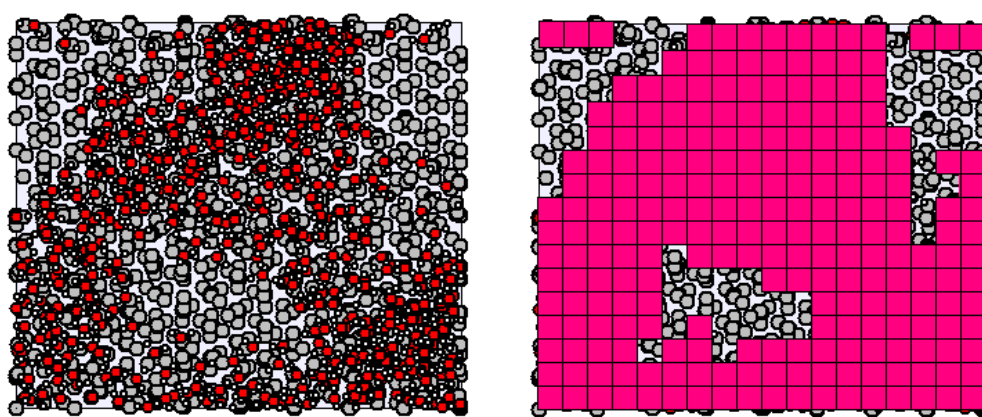


Figure 4.2: The determination of surface occlusion by grid method on the final structure of 10K water substrate, 10K incoming molecules run 2. On the left, a 500-molecule ice structure (red/white) on a cubic ice substrate (grey) is viewed along the z-axis. On the right, a representation of areas which the algorithm determines to be occluded. Grid squares are greatly increased in size here for demonstrative purposes; in fact the fractal length used is 0.04nm, which gives over 7,000 grid points.

The degree of occlusion is determined by generating regularly-spaced geometric points throughout the *xy* plane of the simulation cell. Then the *xy* positions of deposited water oxygen atoms are referenced, and if a point lies within a specified distance of the oxygen, said point is considered ‘occluded’, and a grid square of dimensions equal to the specified fractal length is subtracted from the unoccupied surface area count.

Selecting an appropriate fractal length is extremely important for this analysis, and relates to a general theoretical problem with space-occupancy studies: how large

does a vacancy have to be in order to count as a vacancy? Even perfect hexagonal packing of circles occupies only $[\frac{1}{6} \pi 3^{1/3}]$ (i.e. 90.69%) of a two-dimensional area. A total monolayer coverage of water molecules, meanwhile, would be significantly less densely packed than this, due to the open, hexagonal-channeled structure of ice; so despite the fact that it is not energetically tractable to accommodate any more matter on the surface, an analytical solution would record at best $\sim 1/10^{\text{th}}$ packing inefficiency. We also run up against the problem of *defining* the radius by which we measure ‘coverage’, since water in the TIP4P model is not a hard sphere (and not even a sphere at all, as our concern is in fact the coverage of water molecules), Accordingly, then, any radius we use will be somewhat arbitrary. The position of the first maximum in the oxygen-oxygen radial distribution function has some merit, and it is approximately this distance we choose by taking the hexagonal radius (see *Figure 4.3*):

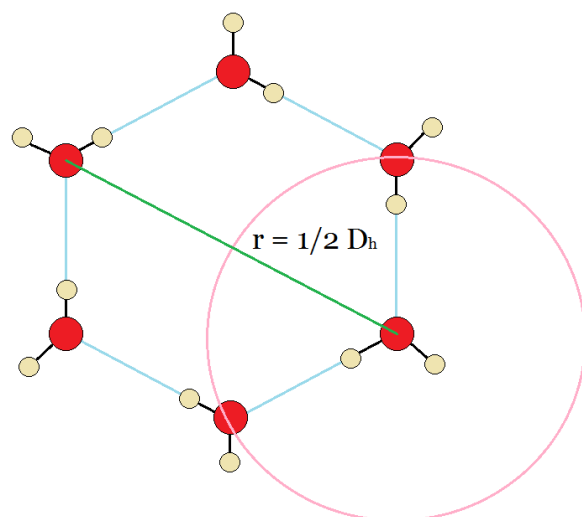


Figure 4.3: The fractal length, r , chosen for surface and volume occupancy calculation is equal to half the diameter of the 3D quasi-hexagonal cross-section in I_c . This gives bulk crystalline cubic ice a space-filled index of 1 in our analysis.

The hexagonal motif in I_c is three-dimensional, with opposite vertices of the hexagon displaced in height by 0.702\AA , which means the displacement is slightly longer than it would be in a regular hexagon: D_h is 5.467\AA , corresponding to an effective exclusion radius of 2.734\AA – close to the 2.75\AA particle diameter, as reported by Zhang & Xu ^[106] and corroborated in *Table 3.1*. Any grid point which lies beyond this radius from any deposited oxygen atom is considered non-occluded.

The ‘hexagonal radius’ is chosen because by applying this analysis to a perfect bulk crystalline water ice bilayer, we achieve a space-filled index of 1: all grid points will definitely lie within the exclusion radius of at least one oxygen atom. So for values *less* than 1 which may be returned by applying the analysis to an ASW, we know the *degree* by which the structure contains more gaps than crystalline ice.

It is possible to perform this space-filling calculation analytically instead of iteratively, and therefore obtain an exact answer. Since we know the positions of all particles at all times, we could calculate the effective radius of each molecule, subtract their overlaps, and determine the surface occlusion that way. A procedure for performing this analysis (and for the volume analogue, see *Figure 4.4* below) is outlined by Truhlar & Cramer ^[107], but the authors themselves confess in the paper that the technique adds vast amounts of computational complexity for only modest accuracy gains over the grid technique of *Figure 4.2*. As such, the latter is the method we use throughout.

Volume occupancy: Using much the same grid-point methodology of the surface occlusion determination, here the three-dimensional volume of the entire simulation cell is embedded with spaced geometric points, and those inside the radius of a water molecule are, again, subtracted from the total volume of the box. It was our original intention to calculate the density of the deposited ice by this method, and from this analysis determine the character of the ice related to LDA, HDA, or VHDA – Essmann and Geiger’s analysis ^[92] reported a hybrid LDA / HDA structure. However, after performing the simulations it was discovered that the microstructure of the deposited ice is often so open and columnar that the majority of molecules are surface molecules, rendering any assessment of bulk volume largely invalid. Instead, then, the volume is measured as a proportion of the whole simulation box – up to the z-co-ordinate of the highest deposited atom - filled by water molecules, providing a measure of the absolute space-occupancy of the structure, rather than the local density of the ASW.

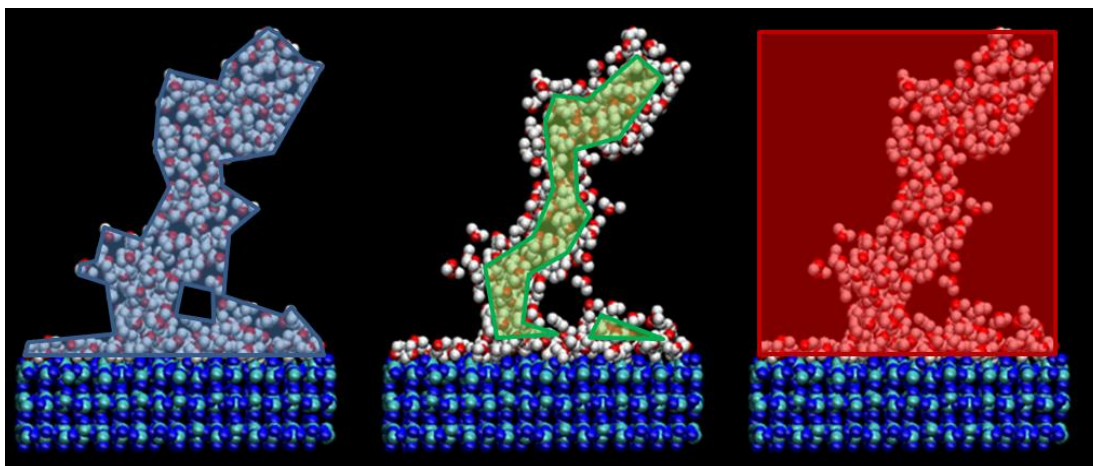


Figure 4.4: Options for sample volume measurement. Sampling the blue volume on the left would give us the nominal density of the tower, but it is not a credible indication of the bulk density of the icy material because so much of the volume is surface atoms, which will orient in space differently to the 'bulk' (green, center). Instead, then, we sample the whole volume of the simulation box, from the height of the lowest oxygen atom to the highest (red, right).

The three-dimensional analogue of the grid method used for surface occlusion is applied, using the same fractal length, 0.04nm. The number of grid points varies from structure to structure because some are taller than others; for a typical 50 Ångström deposition there will be approaching 900,000 points. This 3D grid method is similar to that used by Cazaux et al ^[108] in their assessment of ASW porosity.

Z-density profiles: Oxygens per cubic Ångström as a function of height above the substrate. A similar analysis to the global volume occupancy mentioned above, but observing the evolution of the space-filling as the height profile increases.

Radial distribution functions: Oxygens as a function of their displacement from other oxygens; the same kind of analysis as in *Section 3.3* for the liquid water model comparison runs.

Substrate material	Cubic ice								
Substrate temperature (K)	10			60			130		
Deposition temperature (K)	10	150	300	10	150	300	10	150	300
Maximum structure height (Å)	78.85	30.48	35.43	53.78	32.62	30.96	49.49	25.67	21.04
Std. Dev. in max height (Å)	18.62	3.35	9.83	14.47	4.85	5.90	10.80	1.48	3.16
Average molecule height (Å)	38.87	12.66	12.43	22.44	12.45	11.61	21.74	10.48	9.36
Median molecule height (Å)	39.15	10.84	10.44	20.98	10.60	9.60	21.23	9.04	8.67
Substrate z-axis relaxation (Å)	0.085	0.087	0.105	0.116	0.121	0.121	0.189	0.148	0.185
Volume occupancy proportion	0.211	0.443	0.435	0.288	0.423	0.438	0.307	0.503	0.576
Substrate occlusion proportion	0.692	0.841	0.879	0.702	0.870	0.855	0.687	0.926	0.961

Substrate material	Silica								
Substrate temperature (K)	10			60			130		
Deposition temperature (K)	10	150	300	10	150	300	10	150	300
Maximum structure height (Å)	69.37	49.12	38.52	56.61	47.52	33.72	53.43	33.19	29.83
Std. Dev. in max height (Å)	12.50	3.93	3.83	9.45	7.69	8.56	11.87	5.69	4.60
Average molecule height (Å)	32.31	20.92	14.92	22.05	20.25	13.69	22.20	13.23	12.95
Median molecule height (Å)	30.43	19.82	12.55	18.21	17.69	12.40	20.53	11.28	11.85
Substrate z-axis relaxation (Å)	0.001	-0.005	-0.009	0.041	0.039	0.027	0.122	0.098	0.088
Volume occupancy proportion	0.261	0.338	0.408	0.305	0.351	0.478	0.319	0.473	0.512
Substrate occlusion proportion	0.773	0.741	0.848	0.711	0.729	0.839	0.656	0.812	0.761

Tables 4.1 and 4.2: Static results for each simulation regime. Values are averaged over 5 individual molecular dynamics simulations. See Sections 4.5 - 4.8 for diagrams and discussion of these results.

4.3 – Methodologies and averages for dynamic results

128-height: The cubic ice substrate contains 128 molecules per bilayer, with each bilayer having an approximate depth of 3.65Å. Therefore, if deposited water molecules preferred to form a complete wetting monolayer, at 128 successfully deposited molecules we should expect a height of 3.65Å. Values above this figure quantitatively indicate the preference for island and tower growth on a comparatively clean surface. Therefore we can infer the pseudo-epitaxial growth mode (see Figure 4.12) from the heights at 128 depositions.

Hydrogen bonding: Referring to the nomenclature of Zhang and Buch^[44] in Section 1.6, we detect the connectivity of the deposited waters from their hydrogen bonds. The first minimum of the oxygen-hydrogen radial distribution function lies

immediately beyond 0.957\AA , this being the fixed length of the intramolecular O-H bond. The first intermolecular maximum lies at 1.83\AA and the first minimum lies at 2.50\AA , and so this is the radius around each atom (the oxygen and both hydrogens separately) where we check for the presence of other atoms. Any oxygen within range of a deposited water's hydrogen is considered to have formed a hydrogen bond, and vice-versa; there is no calculated energetic criterion, as the interparticle energy in the simulation depends exclusively on the separation, so the two analyses are equivalent. Alternatively, one could use the first minimum in the oxygen-oxygen separation RDF, which lies at $\sim 3.4\text{\AA}$ ($2.50 + 0.957$), which was the method of Essmann and Geiger.

Only hydrogen bonds between depositing molecules and *other* previously deposited molecules are considered in this analysis. Interactions with the substrate, SiO_2 or I_c , are not sampled.

Number of deposition attempts: Refer to *Section 4.8*; number of deposition attempts gives an indication of effective nonzero sticking probability. Ideal deposition would return a number of deposition attempts equal to the total number of deposited water molecules, 500.

Silica

Deposition T (K)	Substrate T (K)	Deposition attempts	Height 128 depositions	Bonds H@O	Bonds O@H	Bonds OH@HO	Bonds O@HH	Bonds HH@OO	Bonds HOH@OHO	Bonds OH@HHO	Bonds Other
10	10	1092	20.319	0.24	0.2	0.26	0.04	0.05	0.08	0.06	0.07
	60	1089	10.675	0.26	0.22	0.25	0.04	0.06	0.06	0.06	0.05
	130	1101	12.893	0.24	0.2	0.26	0.03	0.07	0.07	0.05	0.07
150	10	612	11.036	0.27	0.21	0.22	0.04	0.07	0.08	0.06	0.06
	60	611	10.978	0.23	0.21	0.27	0.03	0.05	0.08	0.07	0.06
	130	627	10.303	0.23	0.21	0.26	0.05	0.05	0.08	0.05	0.07
300	10	579	9.371	0.23	0.24	0.25	0.04	0.05	0.07	0.06	0.07
	60	581	10.381	0.22	0.22	0.24	0.04	0.05	0.09	0.06	0.08
	130	584	10.679	0.23	0.23	0.24	0.03	0.07	0.09	0.06	0.06

Cubic ice

Deposition T (K)	Substrate T (K)	Deposition attempts	Height (\AA) at 128 waters	Bonds H@O	Bonds O@H	Bonds OH@HO	Bonds O@HH	Bonds HH@OO	Bonds HOH@OHO	Bonds OH@HHO	Bonds Other
10	10	999	21.713	0.26	0.25	0.22	0.04	0.04	0.08	0.06	0.05
	60	1023	12.641	0.26	0.23	0.25	0.03	0.04	0.07	0.05	0.06
	130	998	13.011	0.26	0.19	0.27	0.04	0.05	0.09	0.05	0.06
150	10	628	9.857	0.23	0.25	0.24	0.04	0.04	0.08	0.05	0.07
	60	634	7.109	0.26	0.21	0.24	0.02	0.05	0.1	0.05	0.06
	130	629	7.466	0.24	0.24	0.21	0.04	0.08	0.07	0.05	0.07
300	10	583	7.702	0.25	0.23	0.23	0.03	0.06	0.08	0.04	0.07
	60	586	7.649	0.24	0.22	0.23	0.03	0.06	0.09	0.06	0.07
	130	598	7.075	0.23	0.24	0.23	0.04	0.06	0.08	0.06	0.06

Tables 4.3 and 4.4: Dynamic results for each simulation regime. Values are averaged over 5 individual molecular dynamics simulations. See Sections 4.4 – 4.7 for diagrams and discussion of these results.

4.4 – Height and Growth Modes

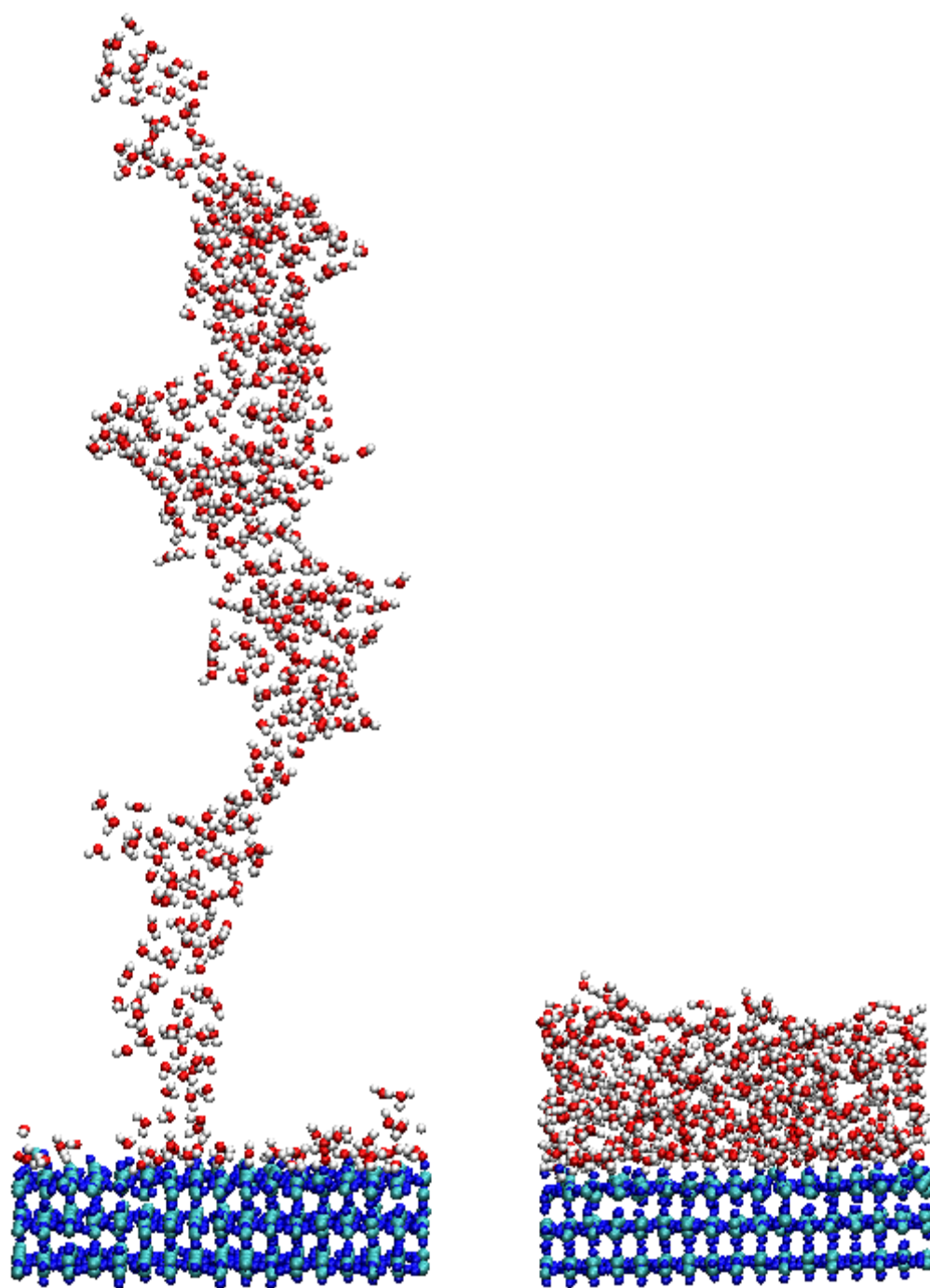


Figure 4.5: Comparison of the tallest (100.6Å, 10K on 10K water substrate Run 2) and shortest (17.7Å, 300K on 130K water substrate Run 4) ASW structures produced in this work. Both structures are composed of 500 deposited water molecules. Blue-green molecules are the pre-existing cubic ice surface; red-white molecules are deposited waters.

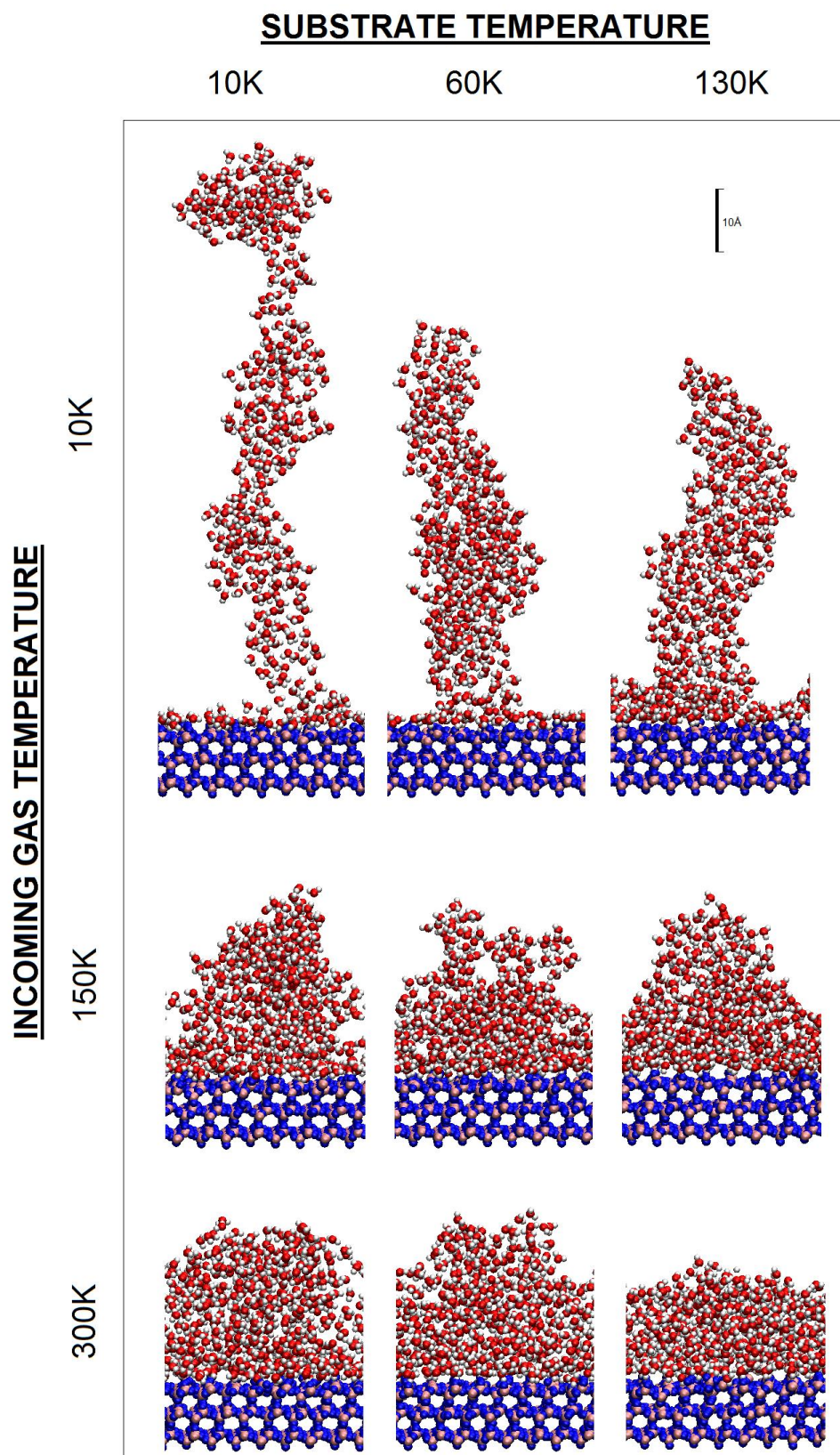


Figure 4.6: Representative images of the produced ice structures at each substrate and gas temperature. Cubic ice substrate in blue, deposited waters in red/white.

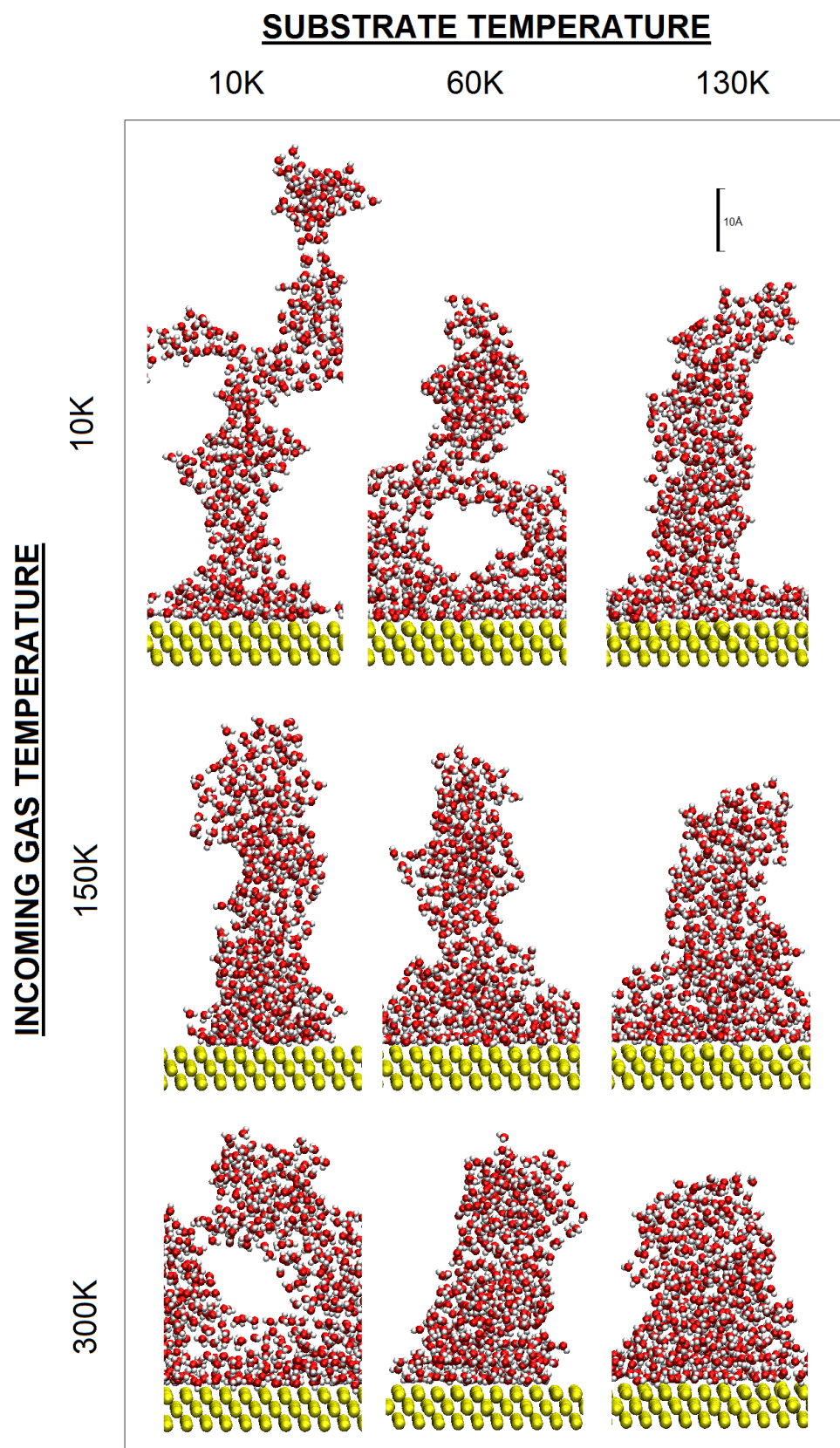


Figure 4.7: Representative images of the produced ice structures at each substrate and gas temperature. Silica substrate in yellow, deposited waters in red/white.

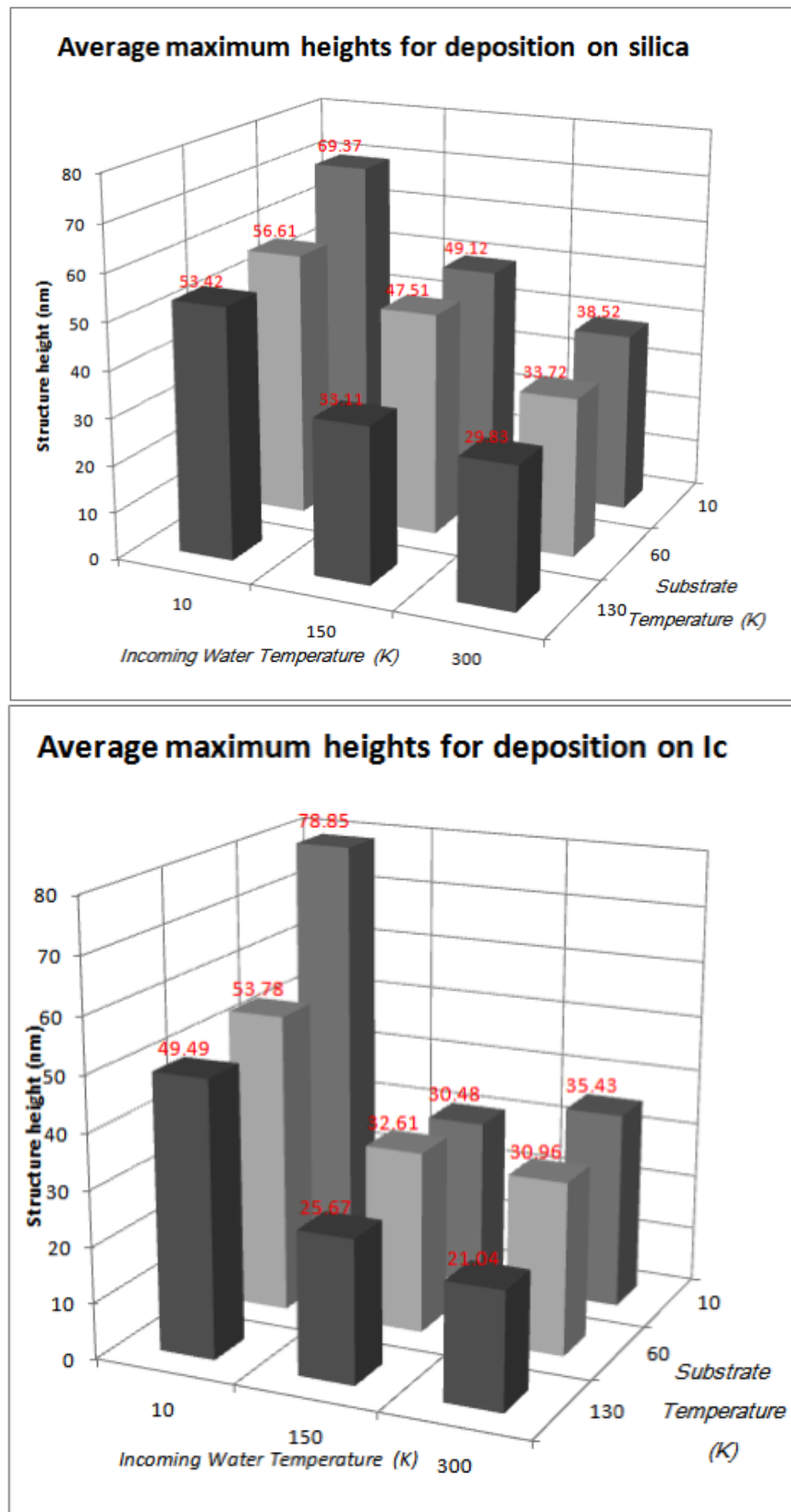


Figure 4.8: Graphs of the average structure height under each temperature / substrate regime. Results averaged over 5 runs.

The overall height of the ice structures produced varies significantly between temperature regimes. Most obviously, lower temperature produces taller structures; as shown qualitatively in *Figure 4.7* and *4.8* and quantitatively in *Figure 4.9*, deposition at colder conditions tended to produce tower-like structures which filled the cell volume inefficiently, while warmer conditions produced compact ice with fewer voids (though not eliminating them entirely).

Both the temperature of the substrate and the temperature of the incoming molecule correlate negatively with final structure height, though the temperature of the depositing molecule is the stronger determinant.

Two separate mechanisms may account for this trend. The first considers that molecules coming in at 300K are less likely to have their trajectories as significantly perturbed by electrostatic interaction with existing structures. Cold deposition molecules are expected to adhere to existing water structures rather than follow a straight path to the bare surface; behavior which would, necessarily, produce larger towers.

This theory would imply a that there should be a greater difference in median and average molecule heights in the 300K depositions than in the 10K depositions, because in the 10K case, molecules are expected in general to stack on top of each other in sequence, with new incoming molecules regularly coming to rest close to, or at, the top of the structure. If this arrangement were adhered to exactly, the height of the median water molecule would be the same as the height of the average water molecule. Meanwhile, 300K molecules are expected to fly ballistically along their random initial trajectories, proportionally less affected by the electrostatic contribution to their travel vectors, and so there should be less correlation between the median and the average.

<i>Comparison of Mean-Median oxygen height deviation</i>			
Deposition T	10K	150K	300K
$ Z_{Med}-Z_{Avr} / Z_{Max}$	0.0356	0.0496	0.0469

Table 4.5: The disparity between median and mean water heights as a function of the total height, segregated by incoming molecule temperature. Values quoted are averages over all 30 structures at each deposition temperature. A low value indicates that the median height and the average height are similar. While 150K returns a roughly similar value to 300K, the salient feature is that both significantly exceed the 10K value, suggesting there is some merit to our reasoning.

In rationalizing the effect of substrate temperature (and material), we can consider also the effects of surface diffusion. By considering data from the dynamics analysis, it is possible to infer the actual growth *modes* of these structures.

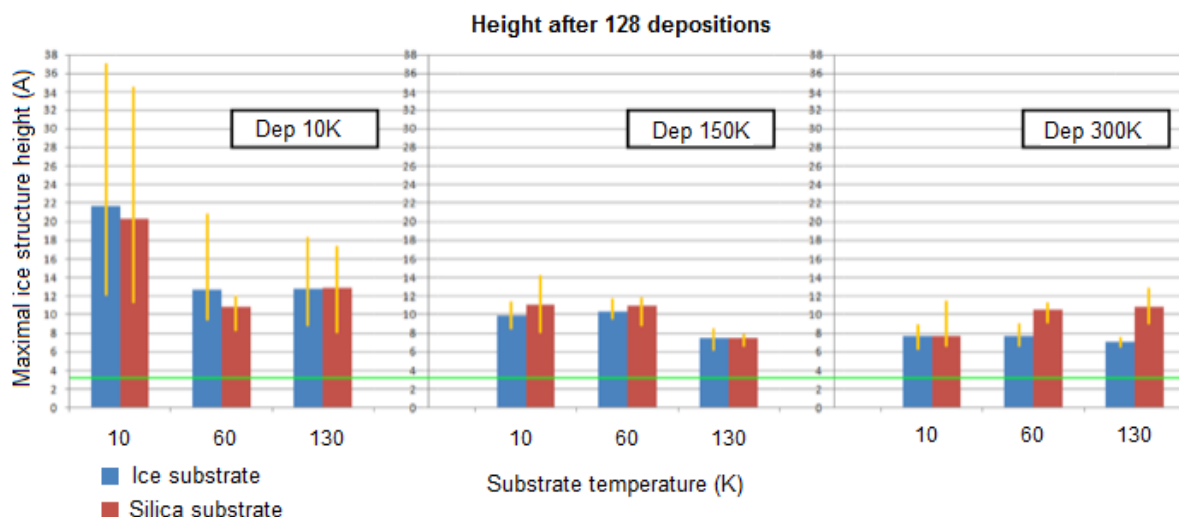


Figure 4.9: Graphs of the average structure height under each temperature / substrate regime after 128 successful depositions. The blue bars represent growth on the cubic ice substrate, the red bars represent growth on silica. The yellow bars on each give an assessment of the range across each of the 5 simulations run for each regime. 3.65\AA is the expected height for ordered monolayer step-flow growth (see Figure 4.10, green line above).

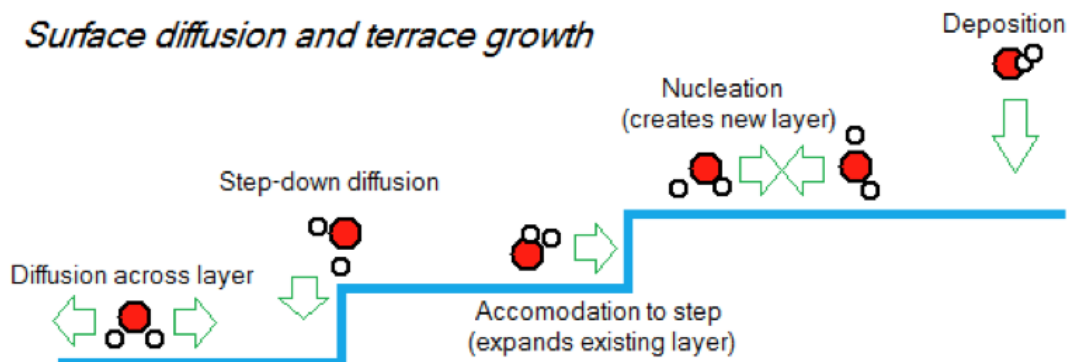


Figure 4.10: The various processes which occur as part of surface diffusion. Not pictured is step-up motion, which is assumed to have too high an energy barrier to be of concern in our cold-cloud environment.

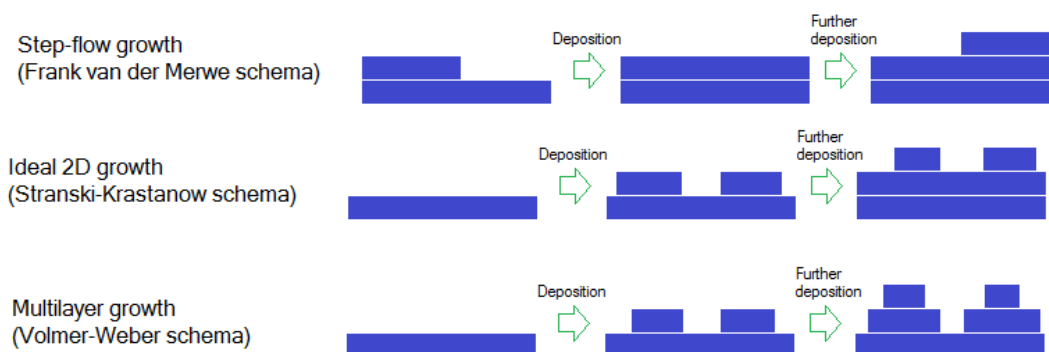


Figure 4.11: The relative rates of the growth processes give rise to three principal different growth modes. Frank van der Merwe growth has fast step-down and accommodation to step; Stranski-Krastanow growth has balanced rates, and Volmer-Weber has slow cross-layer diffusion but fast nucleation.

Considering first Figure 4.9, we note the large range for 128-deposition heights in the 10K incoming case, particularly for the 10K substrates. Since the only thing that differs between two simulations of the same regime is the trajectories of inserted water molecules, this implies that the large spread is indicative of kinetic control in low-T ASW structure-building. If the salient process were in the thermodynamic execution of the simulation (which is the same for all 5 runs), as opposed to the non-equilibrium input (which is different), this would level the heights out to a smaller constraint range.

As discussed above in the considerations about 500-deposition height, we expect 10K incoming molecules to adhere more quickly to existing structures: that is, fast nucleation. And with low kinetic energy supplied either by their own trajectory *or* the temperature of the substrate, they are less likely to diffuse across layers; this being the behavior typified by Volmer-Weber growth. And since Volmer-Weber is expected to give us taller structures, it appears that this must be the growth mechanism adopted for 10K on 10K deposition.

At higher substrate temperatures, all the above logic about water *depositing* on top of existing structures still applies for the 10K incoming waters, but nevertheless we see a drop in both average maximal height and the spread of the maximal heights. This suggests a process which occurs after the initial deposition event. Diffusion across layers and down steps will be more viable as the substrate temperature rises, likely shifting the growth paradigm towards a Stranski-Krastanow schema. This would still produce the kind of ‘rain shadow’ textures observed for the higher-temperature deposition in *Figure 4.1*, but similarly making them less pronounced than in the 10K-10K case, with a corresponding drop in final structure height.

Looking towards the higher temperatures, Stranski-Krastanow growth remains the option most supported by the evidence for deposition of 150K and 300K molecules, although in these cases the temperature of the substrate seems largely unimportant; 128-deposition heights and ranges are much the same when these energetic molecules are incoming. This suggests that, unlike in the 10K-incoming case, depositing 150K and 300K molecules *bring with them* enough kinetic energy to diffuse along the surface to a degree, and they do not require it to be conferred to them by thermal equilibration with the substrate. This rationale applies to *Figure 4.8* as well as *Figure 4.9*, with the implication for astronomy being that a higher temperature in the gas phase ISM will encourage ices to grow by a Stranski-Krastanow mechanism largely irrespective of the solid-phase temperature of the grains.

A further factor to note with regard to the heights is that (aside from the outlier of 10K on 10K), a water substrate prompts slightly shorter structures than silica,

observable in both the final structure height and the 128-deposition heights. We can attribute this to the relative hydrophobic / hydrophilic character of the two substrates. For depositing water, bonding with other waters has a more favourable energy of interaction than with the Lennard-Jones silica, so deposited material is more inclined to form a wetting layer over the surface (successful adoption of which would prompt Frank van der Merwe growth for the first layer) on cubic ice than on silica; see *Figure 4.12*. At low temperatures, this is a moot point, as depositing molecules don't have enough kinetic energy to escape the first position they happen to land in. However, as T increases, molecules are more mobile on the surface, and so more likely to find a deeper minimum. This is why the highest discrepancy between silica-based and I_c -based heights lies in the regime with the most net energy: 130K substrate with 300K deposition. These molecules are better able to move and thus wet the surface; and it is more energetically favorable for them to do so in the water case.

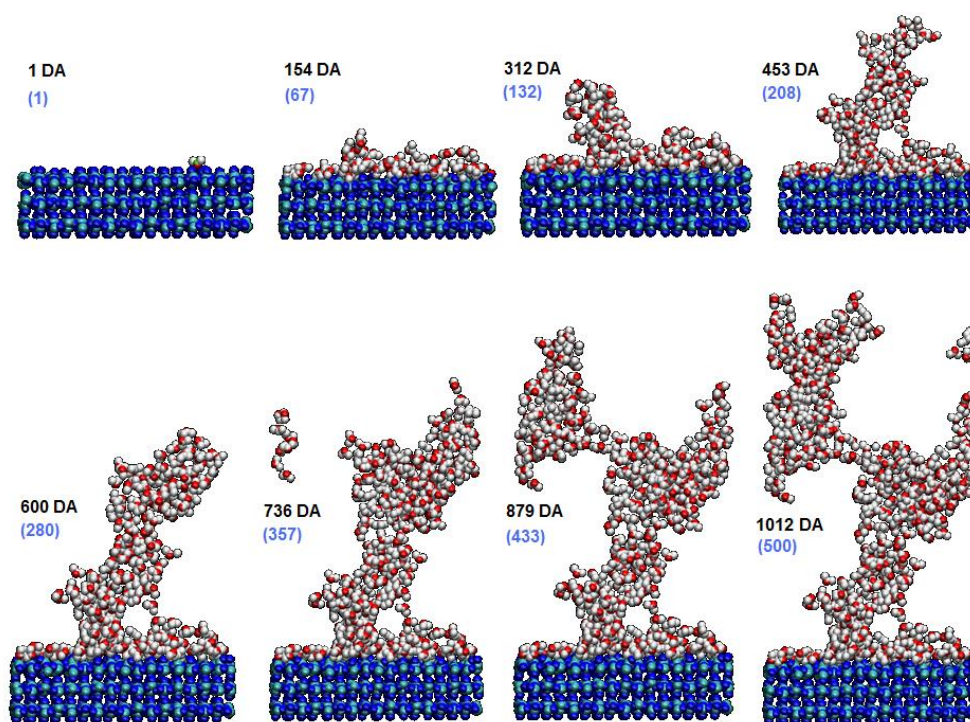


Figure 4.12: The growth of the 10K on 10K ice run 5 ASW structure over time. The number in white represents the number of deposition attempts (DA), while the blue number in parentheses counts the number of deposited water molecules present. The depositing ice can be seen in this orientation to deposit a superficially uniform surface in the second projection, after which the later forms islands and towers. Note the production of a cavity by 879DA as the structure 'closes up' over a rain-shadow void. Another large void seems to be taking shape in the upper right at 1012DA.

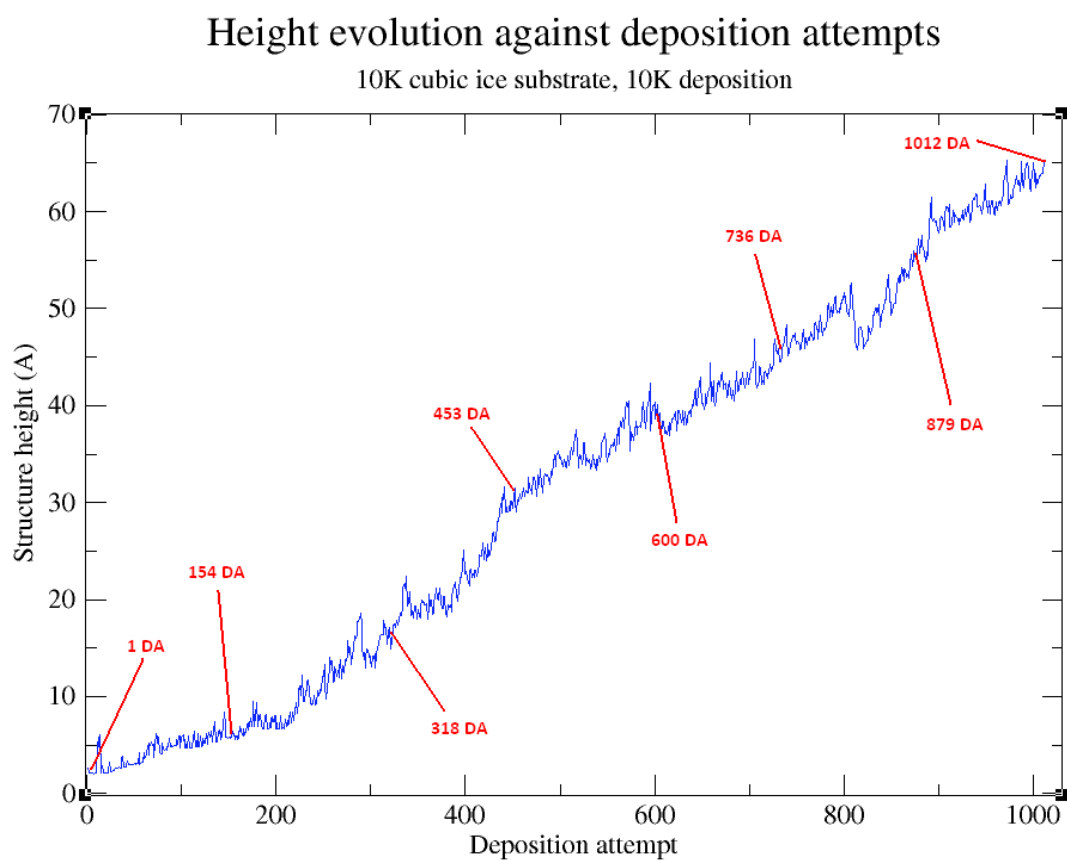


Figure 4.13: Quantitative height of the ASW structure shown in Figure 4.12.

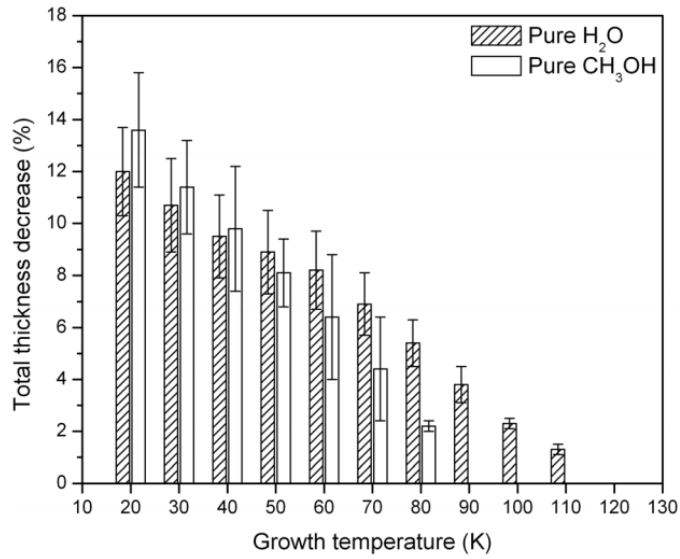


Figure 4.14: The effect of post-deposition heating on water and methane ice structures. Reproduced from [109]. The bars show the decrease in maximum height (in %) of ices deposited at the plotted temperature and then heated to 120K (for water) or 90K (for methane),

Although not directly analogous, some results from Isokoski show a similar sort of effect from temperature. Their physically deposited amorphous solid water ices are assembled at various different (whole-system) temperatures on a silicon surface, and subsequently heated to 120K. Isokoski records a height decrease from this process, as shown in *Figure 4.14*; their value is between 10 and 14%. For 10K water deposition, we see (as shown in *Figure 4.8*) an average structure height of 69Å at a silica surface temperature of 10K, and an average structure height of 53Å at a silica surface temperature of 130K. Although there is no heating involved in our simulations, the difference between the systems at different temperature constitutes a height ‘reduction’ of 23%.

4.5 – Surface Relaxation and Occlusion

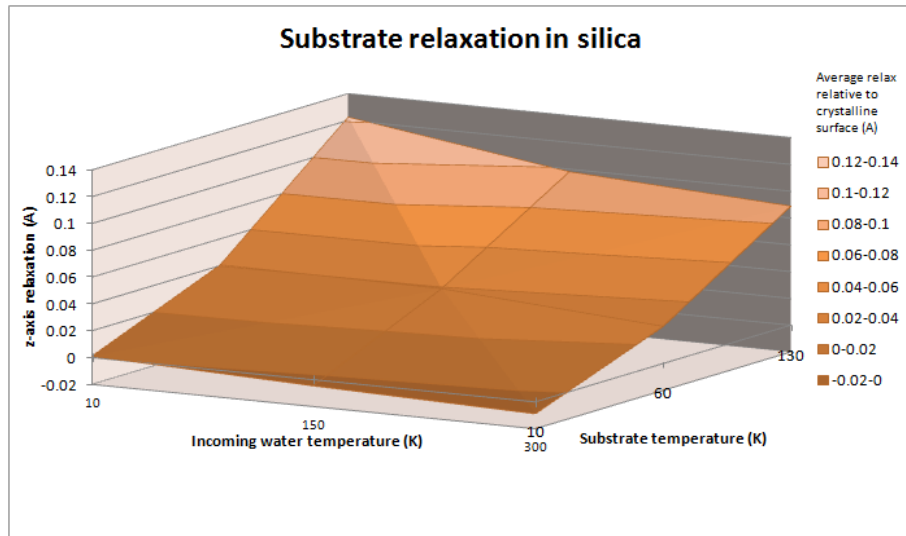


Figure 4.15: z-axial surface relaxation for the silica substrates, plotted against deposition temperature and substrate temperature.

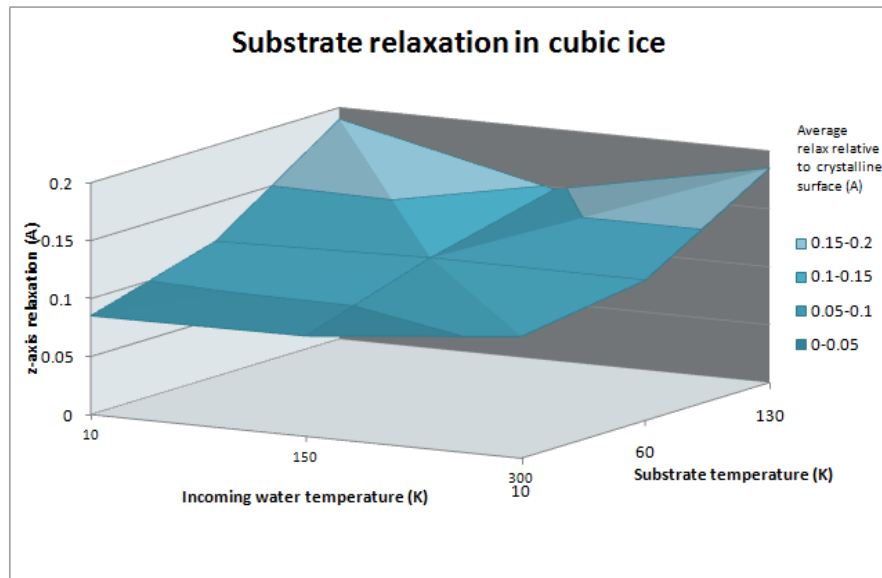


Figure 4.16: z-axial surface relaxation for the water substrates, plotted against deposition temperature and substrate temperature.

Surface relaxation is dominated by substrate temperature. As mentioned in *Section 3.4*, all the surfaces were initially relaxed for a 10K cold cloud; consequently, on travelling to a different part of the ISM and experiencing higher temperatures, we fully expect thermal expansion of the substrate, which is observed at simulation start-up.

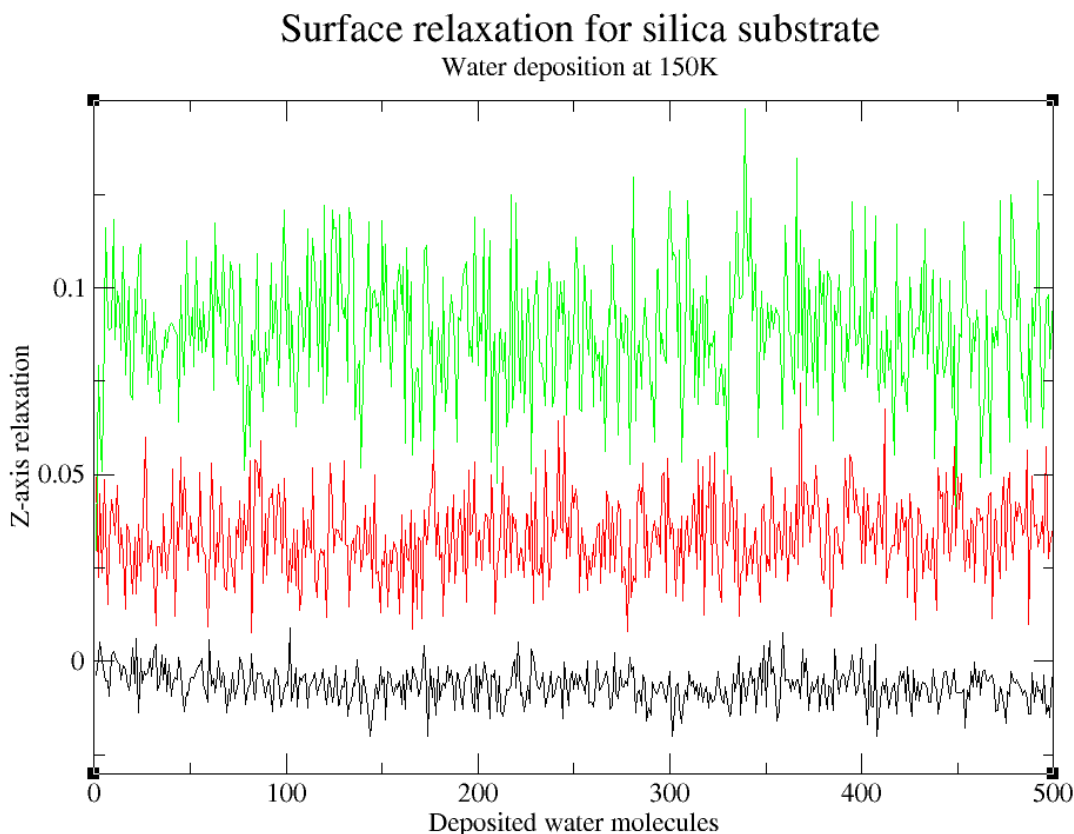


Figure 4.17: z-axial surface relaxation as a function of time, plotted for a single run at the 3 different substrate temperatures. **Black** represents a 10K silica substrate, **red** indicates a 60K silica substrate, and **green** represents a 130K silica substrate. We see that the bulk of the relaxation occurs as a consequence of thermal expansion. The noise in the trends masks any time-dependence for the hotter substrates, but the 10K possibly shows a slight contraction.

An interesting feature from Figure 4.15 is the minor positive correlation between deposition temperature and surface expansion (most consistently displayed for silica): higher T incoming water somehow ‘squashes’ the substrate down.

It has long been known that experimental silica surfaces ^[110] relax ‘inwards’ on cleaving from the bulk; that is, the interlayer separation between the top two layers slightly decreases, principally as a consequence of the complex in-plane rearrangements to three and six-ringed structures. The dangling oxygen atoms form additional partial covalent bonds with the recessed silicon atoms, and so the surface on a whole contracts. However, the opposite is true for the Lennard-Jones approximations used here; LJ atoms relax *towards* the vacuum interface ^[111],

increasing the interlayer separation as a consequence of the absence of repulsive forces on one side of their libration well.

It is concluded that deposited water molecules do not so much *create* an effect by virtue of the substrate-ASW interface, but rather *abnegate* an effect induced by the substrate-vacuum interface. Through the presence of water molecules in an adsorbed layer, and their Lennard-Jones interactions with the SiO₂ particles, the substrate is re-constrained and what was once a surface rearrangement along the *z*-axis now becomes more bulk-like behavior.

If this hypothesis is true, we anticipate that the incoming water temperature dependence of the substrate relaxation arises not as a consequence of the deposition temperature *per se*, but rather from the growth mode induced by the temperature, and more specifically, the degree of coverage of the original substrate by ASW.

The astronomical implication of this effect is that some stresses may be induced in the depositing ice layer as the substrate layer rearranges. This may encourage cracking and the eventual re-release of particles into the ISM.

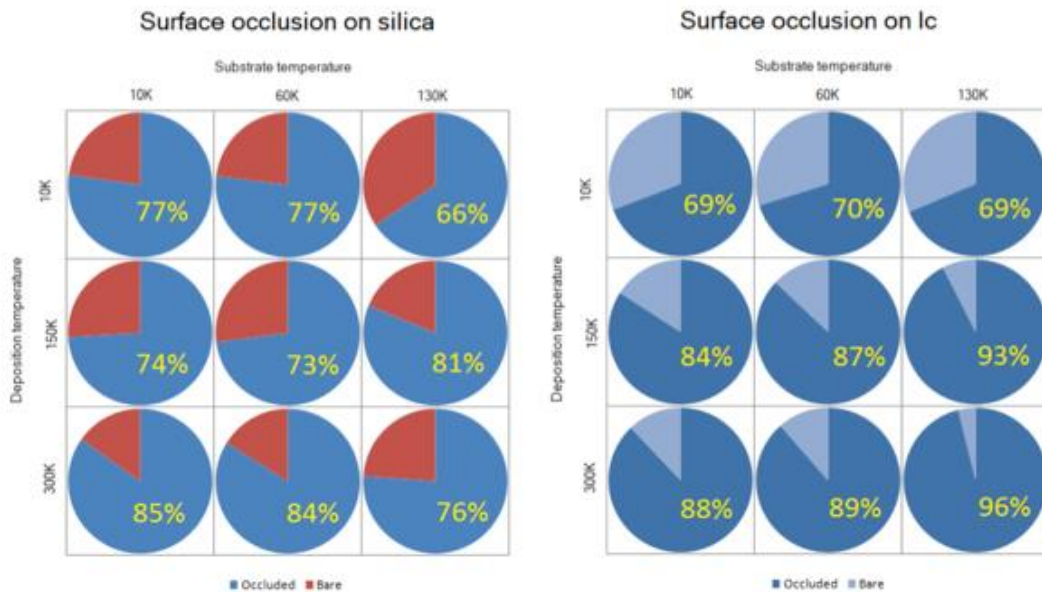


Figure 4.18: Surface occlusions given as proportional coverage of the substrate by deposited water molecules. Looking down on a surface from the *z*-axis, brown represents the amount of bare silica visible, light blue represents the amount of bare cubic ice, and dark blue represents the amount of ASW. All segments are average occlusions taken over the 5 runs performed for each regime. See Section 4.2 for tabulated numerical statistics.

The trend in surface occlusion largely confirms our previous inferences about the nature of growth on the substrate. Occlusion in general increases as deposition and substrate temperature increases, with molecules in the first case provided more energy to *reach* the substrate rather than adhere to a tower, and in the second case allowed more energy to move across the surface and step-down or adhere to steps. The depositions at 10K are the only ones which do not conform to the trend; we would expect both greater occlusion in on the I_c substrate due to hydrophilic wetting, and greater occlusion as the substrate temperature increases. As mentioned in *Section 4.4*, however, the behavior of the 10K ice is much more chaotic, and reliant on the random starting trajectories of its inserted molecules. Collection of additional statistics from further runs would be expected to negate this behavior.

4.6 – Surface Hydrogen Bonding

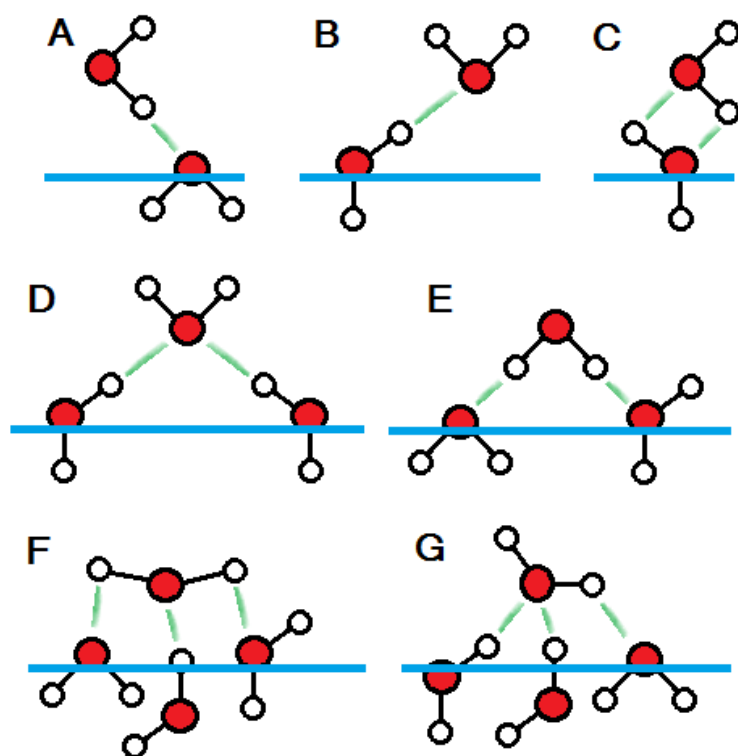


Figure 4.19: Various different classifications of hydrogen bonding mode between a depositing water molecule and other ASW water molecules; see text below.

We describe surface hydrogen bonding in terms of eight different bonding orientations:

- **Type A:** H@O, one hydrogen on the depositing molecule forms a bond with one oxygen in the structure
- **Type B:** O@H, the oxygen on the depositing molecule forms a bond with one hydrogen in the structure
- **Type C:** OH@HO, two H-bonds are formed by the depositing molecule, one on H and one on O
- **Type D:** O@HH, the depositing oxygen forms two hydrogen-bonds while the hydrogen atoms are both ‘dangling’
- **Type E:** HH@OO, both hydrogens form bonds with the structure while the oxygen is ‘dangling’
- **Type F:** HOH@OHO, the depositing molecule forms three hydrogen bonds, one from each hydrogen and one from the oxygen
- **Type G:** OH@HHO, the depositing molecule forms three hydrogen bonds, two from the oxygen and one from a hydrogen
- **Not shown:** “Other” geometries, including molecules with saturated hydrogen bonding networks, or ‘supersaturated’ ones as reported by Zhang & Buch^[44], where oxygens may be ‘H-bonded’ to more than 3 other intermolecular hydrogens.

Molecules are introduced to the simulation 15Å above the topmost pre-existing molecule. When introduced, the molecules have been thermalised in a rarefied gas of the specified deposition temperature: 10K, 150K, or 300K. This means the molecules are introduced with not only different center-of-mass trajectories, but different starting orientations and rotational velocities. As such, a molecule may be expected to impact on the surface in a variety of different ways, forming bonds to the existing deposited molecules with many different possible connectivities. We attempt to quantify the preferred deposition geometries with an analysis of the hydrogen bonding, over 7 different proposed bonding modes.

We define a hydrogen bond by reference to a molecule's co-ordination environment. Co-ordination environments of particles can be probed experimentally through neutron or x-ray diffraction experiments; in MD simulations, however, the co-ordination number of a given particle can be obtained simply, because the simulation has knowledge of each particles' instantaneous position at each timestep. The co-ordination shell of a particle is defined through its neighbour list, \mathcal{L}_i . The neighbour list is a vector which describes the positions of all other particles in the system relative to particle i :

$$\mathcal{L}_i = \begin{pmatrix} f(r_{i1}) \\ \vdots \\ f(r_{iN}) \end{pmatrix} \quad \text{where} \quad f(r_{ij}) = \begin{cases} 1 & \text{if } r_{ij} < r_{lim} \\ 0 & \text{if } r_{ij} \geq r_{lim} \end{cases} \quad (4.1)$$

$f(r_{ij})$ is the Heaviside function, defined for the particle pair i and j as 1 if r_{ij} is below a given value, r_{lim} , and 0 if it is above. Functionally, then, this means the neighbour list can be made to work as a tally for all the particles which are within a given distance of particle i . When r_{lim} is set to the position of the first minimum in the radial distribution function of an particle pair of interest, the squared modulus of the neighbour list over all i , $\langle |\mathcal{L}_i|^2 \rangle$, gives the mean co-ordination number.

We use this method to arrive at a tally of the hydrogen bonding, considering only connections formed between the incoming molecule and other, previously deposited molecules (i.e. bonds to substrate silica and substrate I_c are not included in these statistics). Taking any intermolecular hydrogen-oxygen pair separation of less than the first RDF minimum ($\sim 2.2 \text{ \AA}$) to represent a H-bond, we sum the totals across each simulation. Using the H under the nomenclature of *Figure 4.19*:

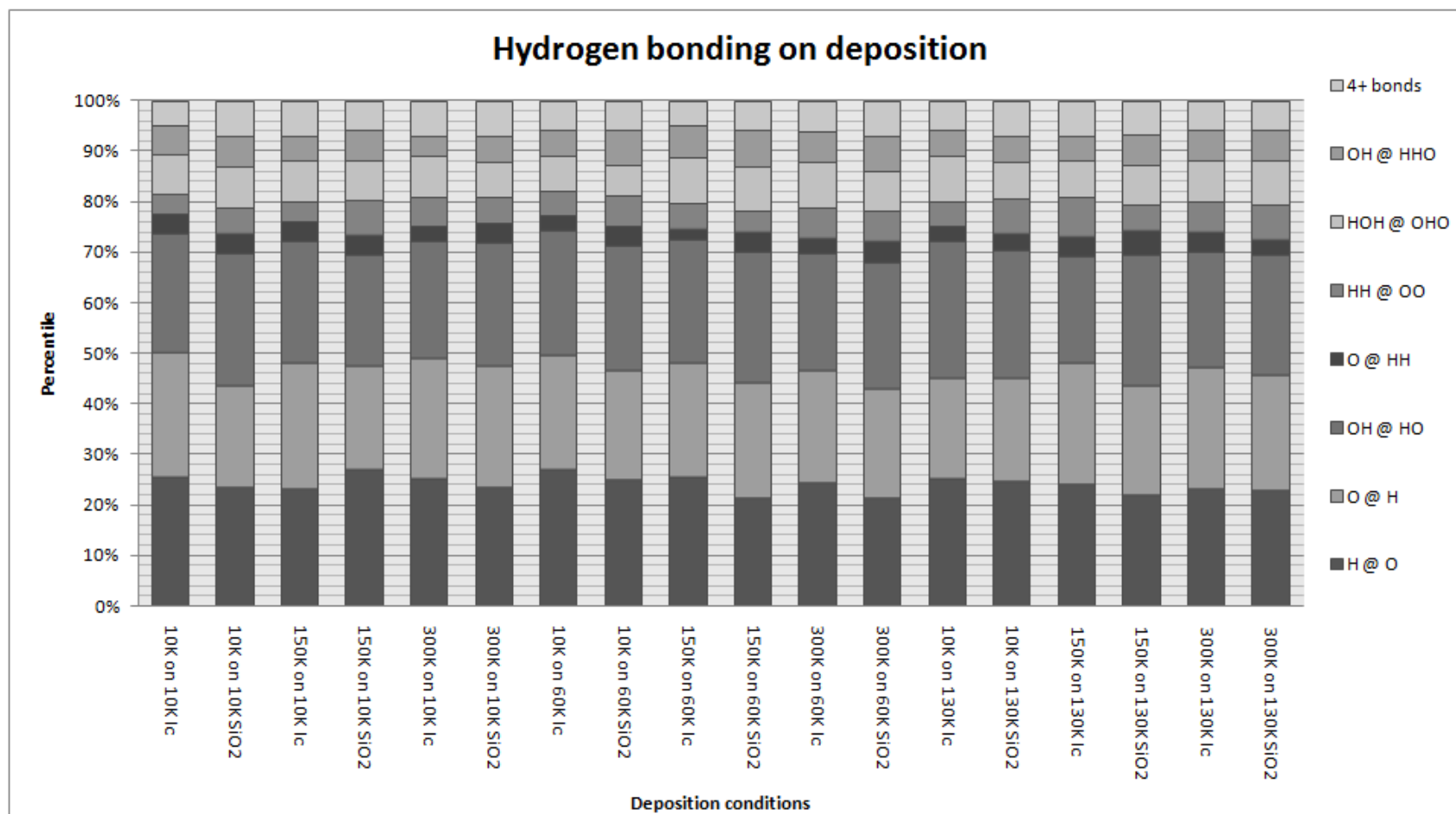


Figure 4.20: Proportion of deposited molecules which report given bonding modes, taken over all successful deposition events for each of the five simulations under each regime. See Appendix B for a statistical quantification.

As shown in *Figure 4.20*, there seems to be no general trend in *any* direction for preferred bonding geometry. Single hydrogen bonds predominate throughout, with between 40 and 50% of all depositions resulting in either O @ H or H @ O only. The next most common arrangement is OH @ HO, which sees a depositing water form two hydrogen bonds. Together, these three geometries account for roughly 75% of all depositions in approximately equal proportion. Other, higher-connectivity bonds are rarely seen, the most common of these being HOH @ OHO, which gives a figure of about 8%.

To an extent, the dearth of highly-connected arrangements is expected. When perfectly crystalline I_c or I_h , which conform to the ice rules, are cleaved to create an interface (as in *Section 3.5*), depending on the plane the surface molecules will have either 1 or 2 dangling bonds. Rearrangement may occur under annealing, but given the structural frustration in low-temperature glassy ASW, a lowering of connectivity is the obvious consequence. A depositing molecule will have difficulty finding a site with the correct distribution of charge to perfectly accommodate it because of the essential amorphous character of the ice.

However, proceeding from arguments in *Section 4.4* and *Section 4.5* regarding rearrangements of surface molecules down steps in approaching Stranski-Krastanow growth, we would anticipate better connectivity on deposition for those molecules with enough kinetic energy to settle into a lower-energy minimum. Specifically, that molecules at higher temperatures, particularly deposition temperatures, are likely to have stepped-down or adhered-to-step, increasing their number of bonds relative to those of deposited molecules which simply stay where they land on a cold surface. *Figure 4.20* does show a minor decrease in the number of highly connected bonds for the 10K depositions, but only of a few percent.

A possible explanation for this result may lie in the question of surface diffusion rates. The geometry of these depositions is calculated from a trajectory where the incoming molecule has been given a *maximum* of 13ps to descend, impact, and equilibrate. It may be the case that surface diffusion processes depicted in *Figure 4.11* occur after this period, surface rearrangement proceeding concurrently with (or

maybe even induced by) the deposition of additional molecules. This could be tested by performing simulations with longer equilibration times before the H-bonding geometry is checked, or through mean square displacement analyses of the thermalised ice. Essmann and Geiger ^[92] and Smith and Kay ^{[85][86]} reported from both simulation and experimental studies that the ices are essentially static after deposition, but our higher-T runs may disagree, particularly at 130K substrate temperature where the bulk phase change towards I_c is approaching.

If the bonding geometry is indeed (meta)stable in the long term after deposition in nature, the dangling bonds are liable to assist in the binding of other molecules to the surface: either subsequent water molecules or other species from the ISM. We would expect that a surface with many dangling bonds (compared to a highly rearranged surface where the bonds are weak van der Waals forces) would retain more gas adsorbents. However, the strength of the binding would disfavor surface diffusion over that on a van der Waals surface, so the overall effect on the ability of such a surface to function as a catalyst for the kind of surface-mediated reactions mentioned in *Section 1* is liable to be mixed.

4.7 – Volume and Density

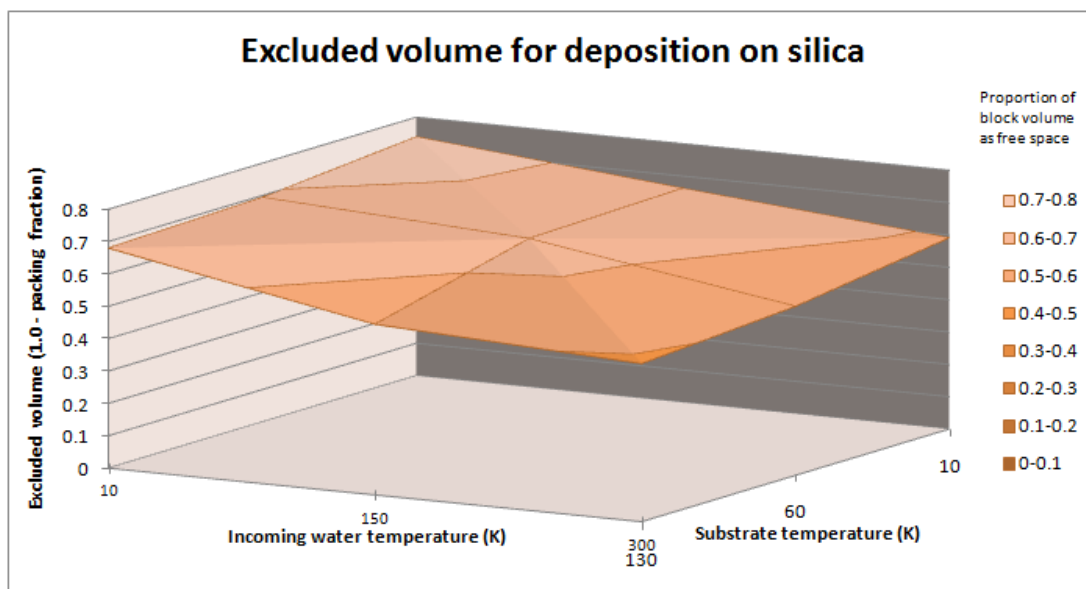


Figure 4.21: Volume occupancy of ice structures on silica as a function of $(1-P)$, where P is the packing fraction as reported in Section 4.3. In these graphs, a 'higher' peak represents ice which is less dense.

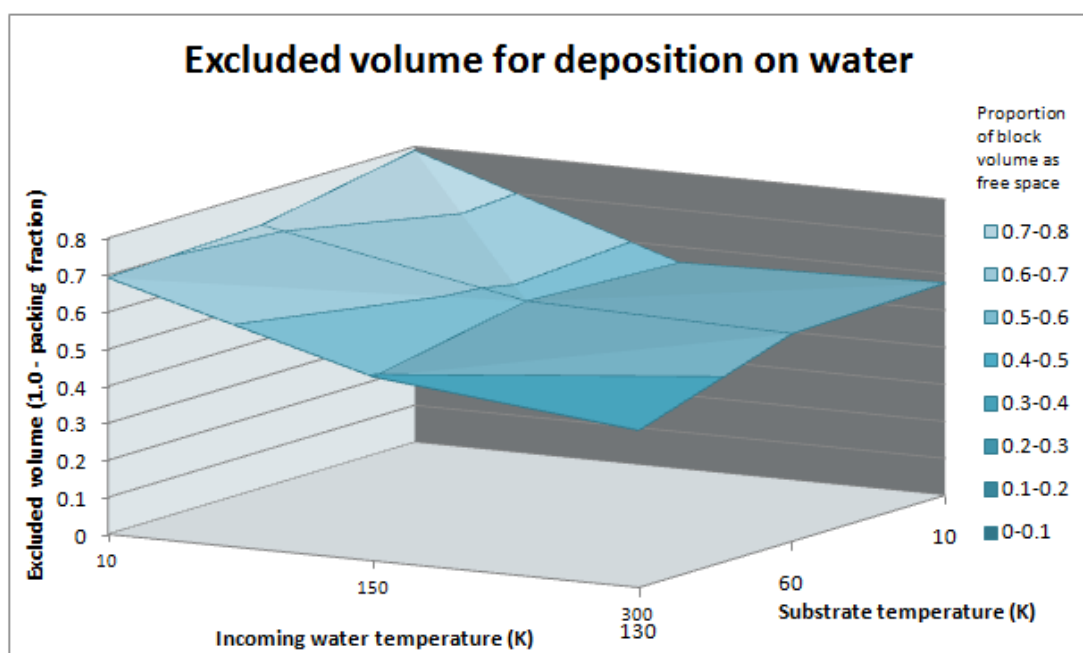


Figure 4.22: Volume occupancy of ice structures on water as a function of $(1-P)$, where P is the packing fraction as reported in Section 4.3. In these graphs, a 'higher' peak represents ice which is less dense.

Volume occupancy follows the trends suggested by *Section 4.4* and *Section 4.5*. With less energy to promote surface diffusion and the step-down mechanism, cold conditions see Volmer-Weber growth and the formation of deep voids and cavities in their structure. This excluded volume – empty but nonetheless semi-enclosed by the surrounding ice through the formation of rain shadows – become like bubbles in a sponge, lowering the density. The average volume occupancy for 10K on 10K water is only 0.21: i.e., approaching only a fifth the overall density of bulk crystalline ice (in regular units, the density of crystalline I_h at 10K is approximately 0.9419 g.cm^{-3} [3], so this corresponds to a meso-scale density of 0.198 g.cm^{-3}). 300K on 130K water, meanwhile, approaches a packing fraction of 0.58. The nature of the sampling method (see *Figure 4.4*) does mean that the irregularity of the top surface has an effect; so this quoted density is expected to increase as more molecules deposit and the surface area / volume ratio reduces. But even given this caveat, it seems obvious that the propensity of the cold ice to form cavities is high, particularly in the low temperature scenarios (see *Figure 4.23*). Given that ASW produced by supercooling or the application of high pressure returns (HGW / HDA, see *Section 1.5*) a density of between 0.91 and 0.98 that of regular ice, it is clear that astrochemical ASW as generated here by physical deposition is a fundamentally different material on the meso-scale than these other water glasses. For Essmann and Geiger’s physical vapour deposition ices (60K incoming molecules on a 60K silica substrate), they report via a “sphere expansion” method densities of 1.1 to 0.75 g.cm^{-3} (corresponding to 1.16 and 0.80 in our nomenclature). However, they sample the density only over local volumes of $< 118 \text{ \AA}^3$ (a sphere of radius 3.0 \AA), whereas for a 50 \AA -high structure on a silica substrate our sampling volume is $51,000 \text{ \AA}^3$. The trend in Essmann and Geiger’s density is that the value decreases as sampling volume increases, and therefore on a basic level this is compatible with our results. They conclude that the physical vapour deposition ice is an intermediate structure between LDA and HAD. In our simulations, the thinness of the films and abundance of cavities mean the ice is not sufficiently bulk-like to credibly attribute a bulk structural type.

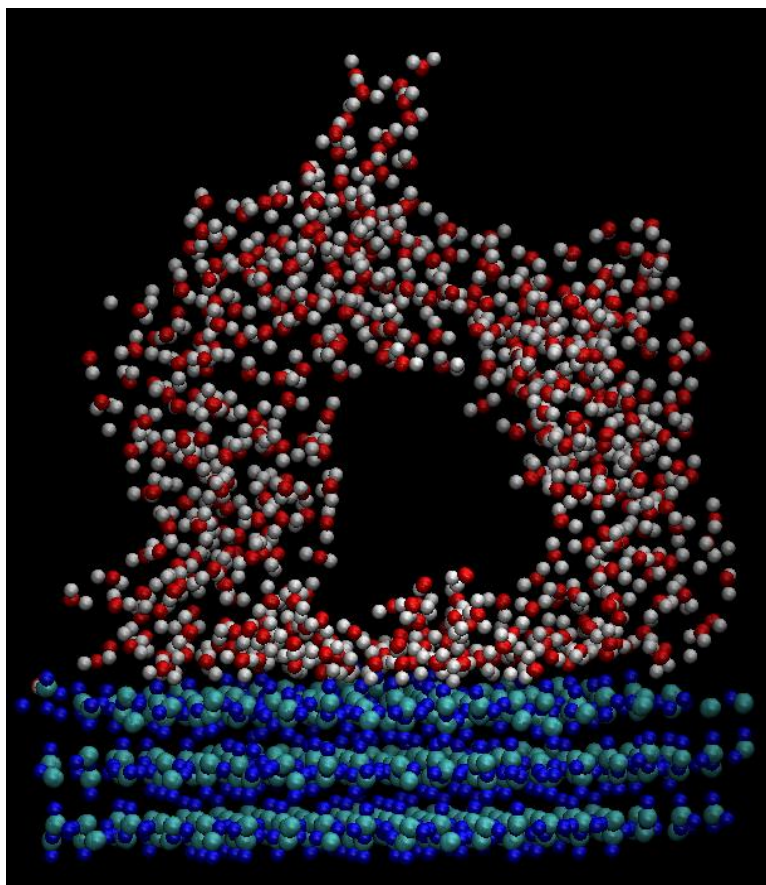


Figure 4.23: An enclosed cavity generated in 10K deposition on a 60K water substrate Run 3. Referring to Figure 1.14, we expect that such cavities may be filled with CO or other gasses from the ISM, eventually closing up in three dimensions and trapping volatile guest species under the ice.

The information about the nature of the ice which we can legitimately draw from radial distribution studies is limited for precisely the same reason that constrains our conclusions from the volume analysis: a high proportion of the molecules are surface molecules, and as such we see in the RDFs the profile of the surface structure rather than the bulk. A sharper first peak in the low-temperature case is expected, and observed, both on account of the damped particle libration but also as a consequence of the more anisotropic environment at the surface; as in the columnar structures, water molecules do not *have* as many long-range neighbours as they do in the more compact structures, which – via the normalisation – skews the RDF to reporting a higher first peak and lower second peak; see *Figure 4.24*.

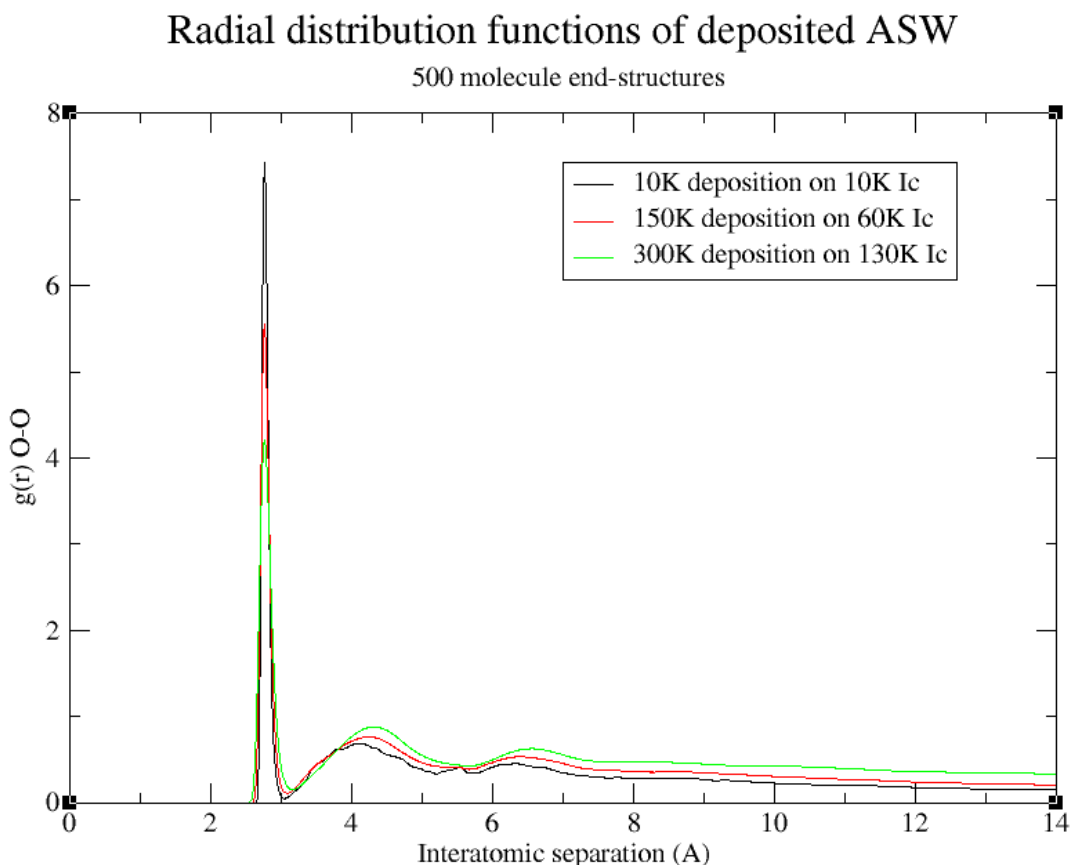


Figure 4.24: Radial distribution functions for oxygen-oxygen separations in some of the ASWs produced on cubic ice. Functions are averaged over all 5 runs for each of the 3 regimes. Histograms accrued for 100,000 timesteps with bin widths of 0.01Å. Results for the silica substrate were very similar to the above; see Table 4.5.

It is at least interesting to note that all the regimes report the first peak at the same separation: in the 2.75-2.76Å region, the same as in liquid water (see *Table 3.1* and *Figure 3.3*), but much sharper peaks. This agrees with Essmann and Geiger’s work, who likewise saw a taller spike with comparison to liquid water (though theirs was somewhat more pronounced than ours, with an intensity >8 for 60K on 60K). A feature which the previous work would not have been able to pick up – given their restriction to a single temperature regime – is the retreat of the second and third peaks as the temperature increases. This behaviour has been observed in liquid water by neutron diffraction and simulation^[112] (although over larger temperature ranges), and we attribute it simply to a positive $\Delta V/\Delta T$ in homogeneous ASW – a trend which would normally be identifiable in the density trends, but in our simulations is obscured by the increased cavitation at lower temperatures.

Radial Distribution Function Results For Silica Substrate										
Atom Pair	Substrate T (K)	10			60			130		
	Deposition T (K)	10	150	300	10	150	300	10	150	300
H-H	1st RDF peak position (Å)	2.15	2.20	2.26	2.26	2.25	2.23	2.23	2.29	2.29
	1st RDF peak intensity	5.76	6.06	5.22	5.31	5.43	5.91	5.27	5.25	4.89
	2nd RDF peak position (Å)	3.64	3.51	3.65	3.73	3.61	3.62	3.78	3.62	3.74
	2nd RDF peak intensity	3.57	3.73	3.36	3.44	3.44	3.86	3.73	3.38	3.44
H-O	1st RDF peak position (Å)	1.85	1.83	1.82	1.85	1.86	1.88	1.87	1.88	1.88
	1st RDF peak intensity	8.85	10.65	9.13	8.28	9.03	8.99	7.59	6.89	6.97
	2nd RDF peak position (Å)	3.12	3.18	3.16	3.15	3.18	3.17	3.17	3.19	3.15
	2nd RDF peak intensity	5.65	5.98	5.47	5.48	5.47	6.10	5.43	5.25	5.11
O-O	1st RDF peak position (Å)	2.76	2.77	2.75	2.76	2.76	2.76	2.80	2.76	2.77
	1st RDF peak intensity	15.97	16.84	15.66	14.75	15.21	16.33	12.23	12.28	12.51
	2nd RDF peak position (Å)	4.22	4.10	4.14	4.20	4.33	4.26	4.20	4.37	4.37
	2nd RDF peak intensity	2.93	3.38	3.02	3.08	3.12	3.71	3.62	3.26	3.43

Radial Distribution Function Results For Cubic Ice Substrate										
Atom Pair	Substrate T (K)	10			60			130		
	Deposition T (K)	10	150	300	10	150	300	10	150	300
H-H	1st RDF peak position (Å)	2.19	2.25	2.27	2.26	2.26	2.22	2.30	2.30	2.21
	1st RDF peak intensity	6.37	6.10	6.21	5.31	6.41	5.94	5.44	5.72	6.03
	2nd RDF peak position (Å)	3.59	3.54	3.59	3.73	3.82	3.64	3.78	3.68	3.68
	2nd RDF peak intensity	4.27	3.76	3.85	3.44	3.98	3.70	3.88	3.94	3.79
H-O	1st RDF peak position (Å)	1.84	1.84	1.84	1.85	1.85	1.84	1.87	1.84	1.87
	1st RDF peak intensity	11.19	10.25	10.86	8.28	9.62	10.17	7.37	9.12	8.05
	2nd RDF peak position (Å)	3.14	3.16	3.19	3.15	3.16	3.18	3.16	3.14	3.23
	2nd RDF peak intensity	6.34	6.03	6.33	5.48	6.01	6.09	5.78	6.00	5.81
O-O	1st RDF peak position (Å)	2.76	2.75	2.76	2.76	2.76	2.74	2.76	2.76	2.76
	1st RDF peak intensity	18.22	18.06	18.60	14.75	16.03	15.72	13.07	15.93	14.11
	2nd RDF peak position (Å)	4.07	3.91	4.51	4.20	4.27	4.30	4.23	4.30	4.44
	2nd RDF peak intensity	3.55	3.38	3.51	3.08	3.99	3.60	3.71	3.69	4.30

Table 4.5 and 4.6: Radial distribution features averaged over 5 runs for each deposition regime; see Figure 4.24.

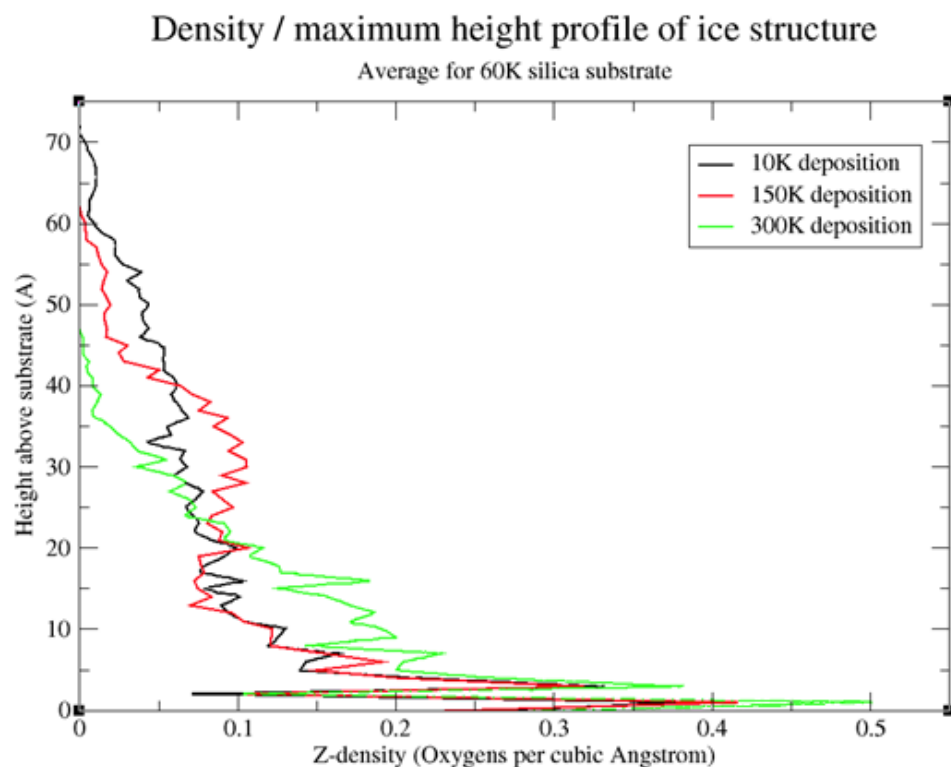


Figure 4.25: Density / height distributions for deposition on 60K silica. Functions are averaged over all 5 runs for each of the 3 regimes. Histograms accrued for 100,000 timesteps with bin widths of 1Å in all Figures 4.25 – 4.29.

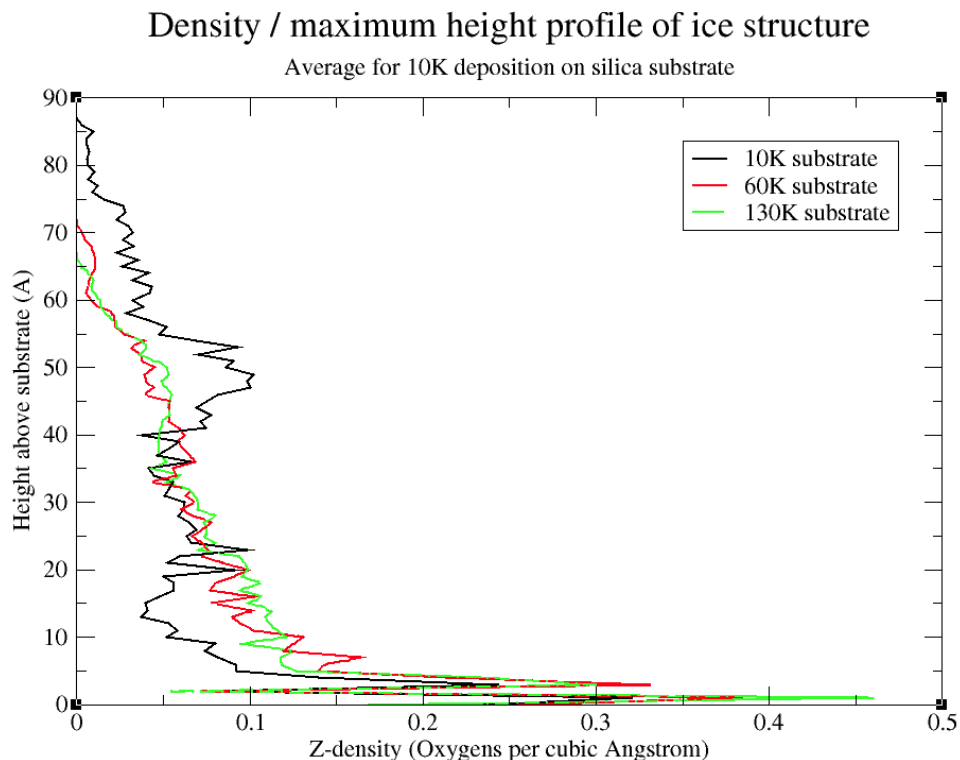


Figure 4.26: Density / height distributions for deposition of 10K water on silica at different T. Functions are averaged over all 5 runs for each of the 3 regimes.

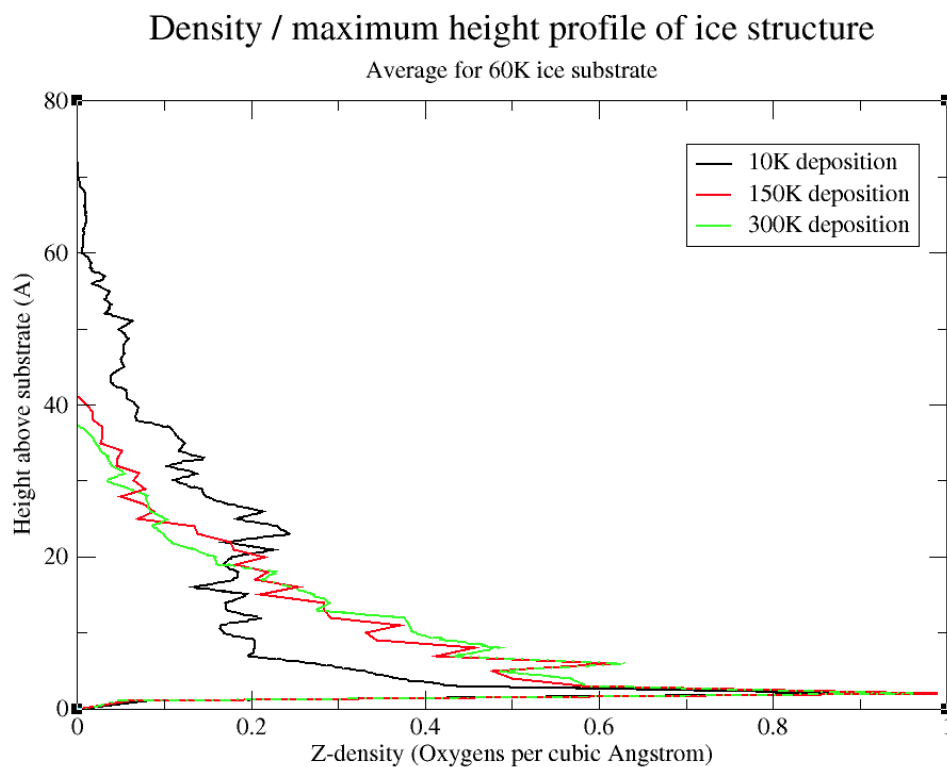


Figure 4.27: As in Figure 4.25, density / height distributions for deposition on 60K cubic ice. Functions are averaged over all 5 runs for each of the 3 regimes.

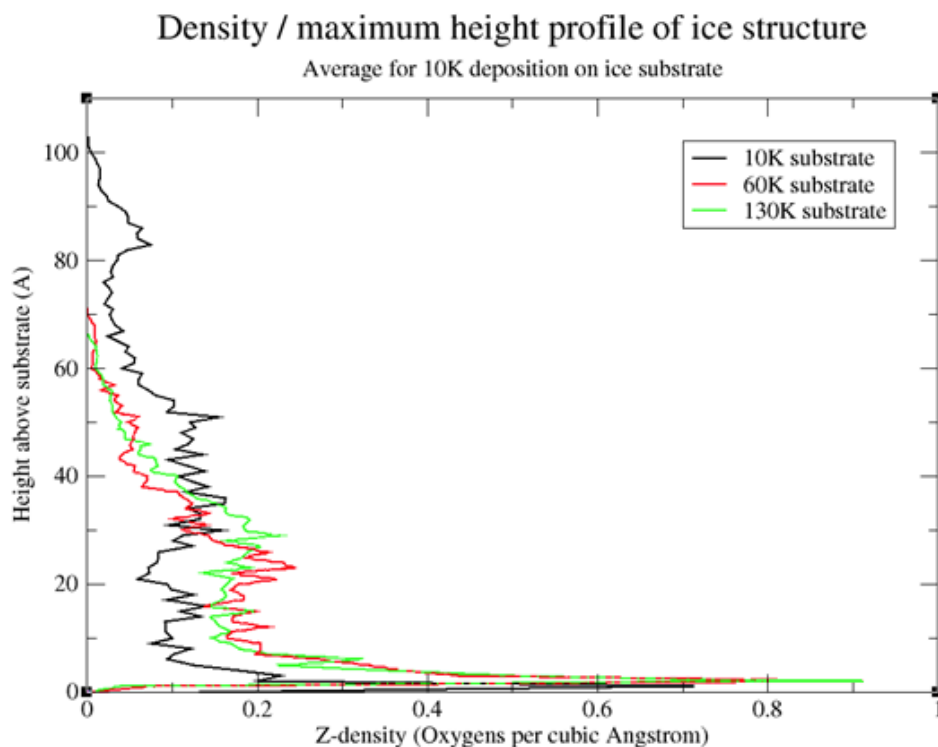


Figure 4.28: As in Figure 4.26, density / height distributions for deposition of 10K water on cubic ice at different T . Functions are averaged over all 5 runs for each of the 3 regimes.

Consideration of the density/height distributions is most interesting at the lower reaches of the graphs, where two sharp peaks (most visible in *Figure 4.25*, see expanded *Figure 4.29*) give possible indication of the formation of a partial, semi-amorphous ice bilayer (the second peak lies at 4\AA , which conforms to the known crystalline bilayer width of 3.65\AA). This behaviour corroborates the surface occlusion charts of *Figure 4.18*, with the highest water densities occurring at both high deposition temperatures and high substrate temperatures.

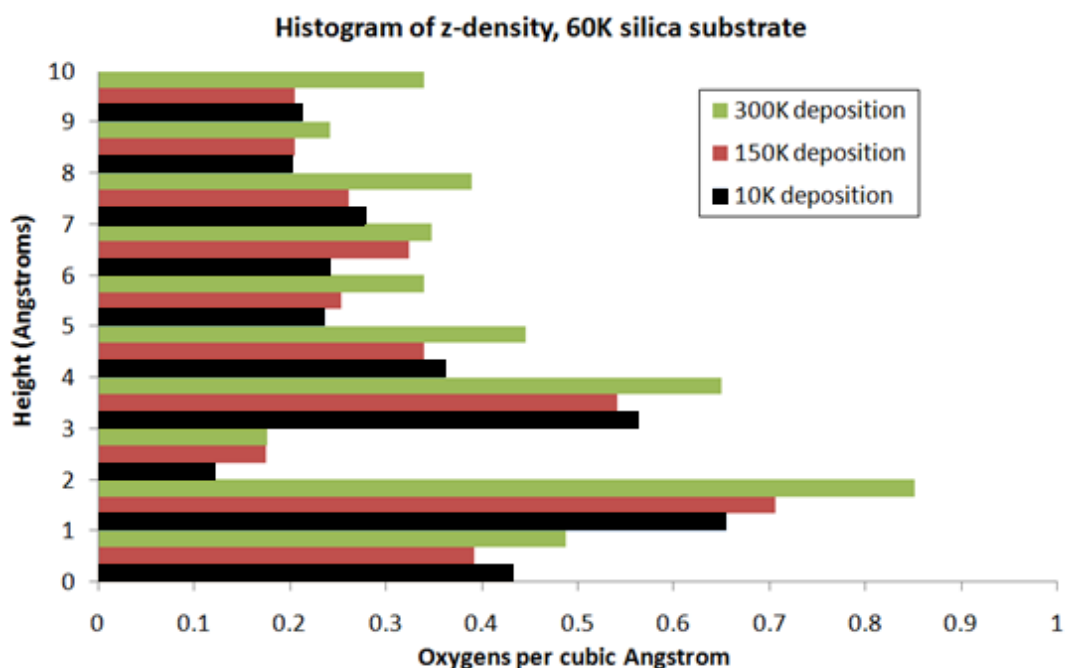


Figure 4.29: Expansion of the lowest 10 Angstroms of Figure 4.25, i.e. deposition on the 60K silica surface. The highest densities of all 3 deposition temperatures come at 1-2 \AA and 3-4 \AA : a bilayer.

In all of these figures it is the highest temperature (of either substrate or deposition) which produces the densest arrangement of water molecules at the very bottom of the graphs, 0-2 \AA . This is a partial wetting layer on the substrate itself, and so those with more energy to rearrange are those which can migrate laterally to cover more of the grain surface.

Also interesting to note in *Figure 4.26* is the irregularity of the 10K on 10K height profile. While the 60K and 130K density profiles are essentially pyramidal, with a gradual decrease in density as the z -ordinate increases, the 10K profile has bumps and peaks all the way up to 50\AA . This is once again indicative of the random and irregular structures of the towers formed under the coldest conditions. *Figure 4.30* gives a representation of this behavior from the visualiser.

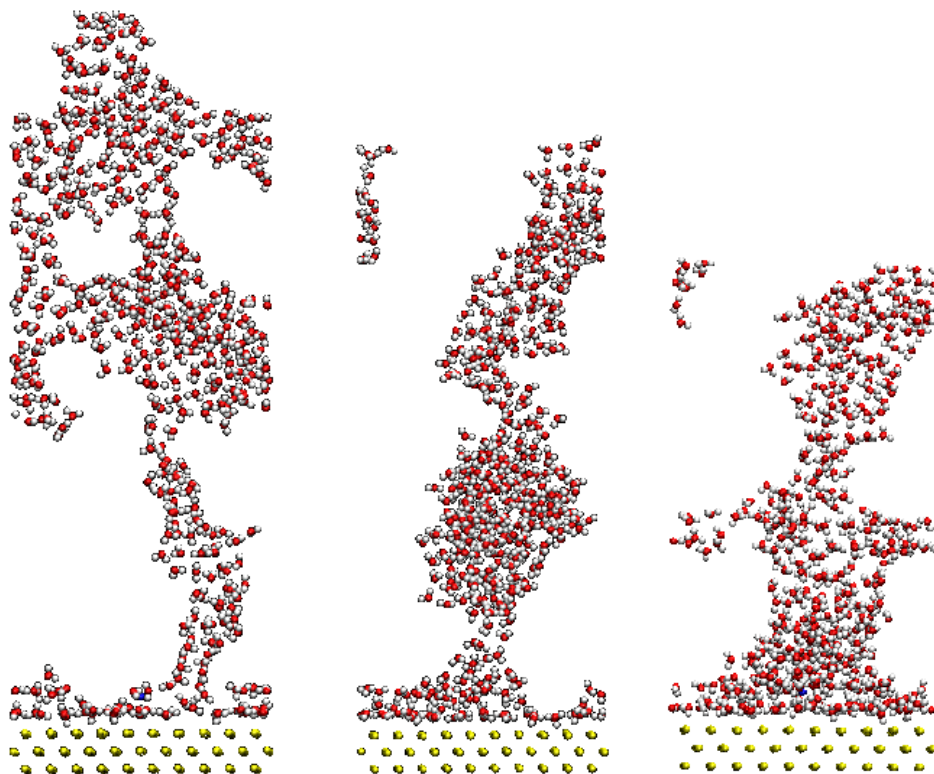


Figure 4.30: Irregular towers in the 10K deposition on 10K silica regime. Recall again that ‘floating’ atoms are connected across the cell width by the periodic boundary conditions.

These irregular, towering structures have been seen in the simulations of other workers. The work of Kimmel (with regard to ‘rain shadow’ structures) was mentioned in Section 1.6, but a similar visualization can be seen in the work of Garrod ^[113]. He performed large-scale Monte Carlo simulations of water-grain interactions in the ISM, see *Figure 4.31* below. Monte Carlo techniques differ from our Molecular Dynamics in that the former do not compute Newtonian trajectories for particles, but rather particles are moved probabilistically, weighted on whether the energy state of a projected (random) move is energetically favourable or not.

Garrod’s work was primarily concerned with effects of gas-phase density (not explicitly tested by us) on the grain-surface formation of water from its radical O and H constituents (refer to *Section 1.4*, depicted on the right in *Figure 4.31*). While the quantitative results of that work concern themselves with the distribution of co-formed H_2 , the ‘control’ simulation of molecular H_2O deposition shows a great deal of qualitative similarity to our disordered tower structures produced at the same gas and grain temperatures. Garrod attributes these structures to the low surface diffusion rates at 10K; at higher temperatures, lateral movement of molecules can fill in pores.

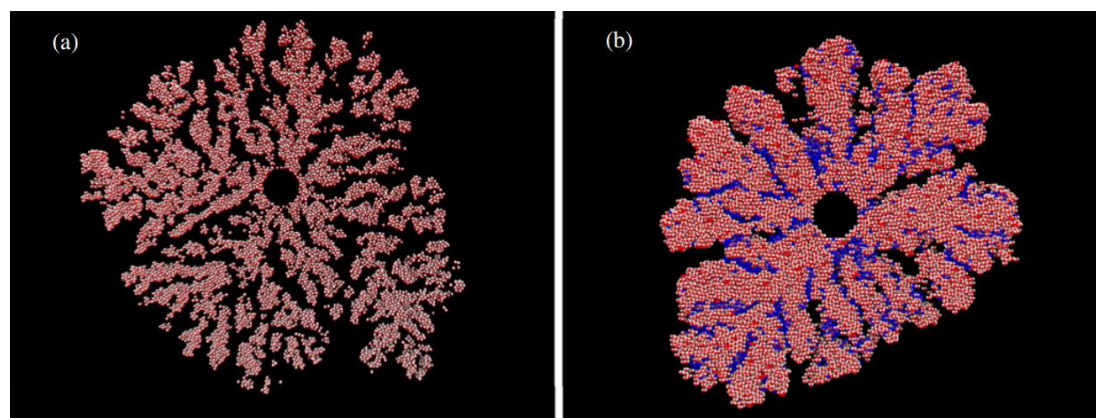


Figure 4.31: Reproduced from [113], Monte Carlo simulations of ice layer growth by Garrod. Left: Deposition of molecular H_2O , 10K gas and 10K grain temperature, van der Waals surface. Right: Deposition of atomic H and O followed by reaction.

Previous studies which did consider system temperature include those of Isokoski^[109] (see *Section 4.4*), and that of Cazaux et al^[108]. The latter’s work (as with Garrod’s) performed all depositions at gas and grain temperatures of 10K, and then subsequently proceeded to heat the structures to 120K. Their 10K molecular deposition ASW ices gave similar porous structures to our and Garrod’s results, but at higher temperatures their structures produced larger pores, not smaller as in our work. The process described by Cazaux is that, on heating, the overall structural height of the ice remains fairly constant, but small pores agglomerate into larger ones, raising the connectivity of water molecules as well as raising the average pore radius (contrasting with Isokoski’s results of a $\sim 15\%$ reduction in structure height).

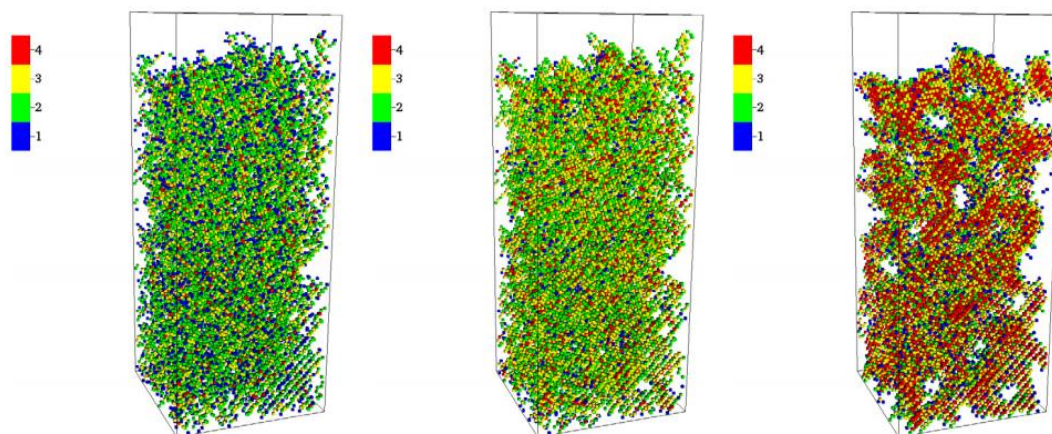


Figure 4.32: Reproduced from [108], Monte Carlo simulations of ice layer growth by Cazaux et al. Left, 10K; center, heated to 60K; right, heated to 100K. The colour key represents the number of H-bonds each water molecule is involved in (measured at the end of the simulation, rather than at the moment of deposition as we do in Section 4.7; as such the connectivity results are not directly comparable. What is of relevance is that the maximum height of the structure, and thus the excluded volume, is almost invariant over the course of the heating.

However, our results and Cazaux's are not necessarily mutually exclusive, as their work concerns 10K deposition and subsequent heating, whereas ours involves no heating over time. From our work, ASW layers which *form* at higher temperatures (especially higher gas temperatures) have higher density; Cazaux's study agrees that deposition at 10K produces a low-density structure, but adds that when these structures are heated, the low density remains, as the structure rearranges via pore coalescence rather than via 'melting' to a pore-free structure, the latter being what was observed in our simulations when the ices were *formed* at the higher temperatures.

4.8 – Deposition failures

In a preliminary test deposition of 83 gas-phase molecules at 10K on a 10K cubic ice substrate, the sticking probability of water on the surface was found to be 1 by inspection. However, of the 83 molecules inserted into the simulation with $-z$ momentum, only 66 were adhered to the surface at the end of the run; 17 had been reflected on the approach to the surface, a significantly higher proportion than the ~13% rejection rate expected by Section 3.7.

This effect was determined to be partially dependent on orientation, and can be rationalized by reference to the starting surface topology and force fields employed in the model. As part of the minimum image convention management of long-range forces, a truncated and shifted Coulomb sum is employed for the electrostatic interactions (see *Equation 3.1*). Accordingly, an incident water molecule descending towards the cubic ice substrate will, at the instant of its insertion beyond the r_{cut} of the topmost surface atom, experience no outside forces and simply travel downwards towards the surface along its starting center of mass trajectory.

The surface at the start of the simulation is [1,1,1] cubic ice with H δ^+ as the topmost atoms, with an O-H bond distance in TIP4P/2005 of 0.9572Å. Due to the Coulomb force truncation, an incoming water molecule experiences *only* electrostatic interactions with these hydrogens when it is at a distance of between 14.00 and 13.04Å from the surface. Although the incoming water molecule overall is charge-neutral, low linear downward momentum and slow rotation speeds at 10K mean that if the molecule approaches the surface in a ‘hydrogen-first’ orientation, the repulsive interaction between the H δ^+ charges could be sufficient to reverse the molecule’s momentum and reflect it away from the substrate.

Test simulations were conducted to test the hypothesis, using non-rotating incident molecules travelling downwards without x or y velocity components, and with $-z$ momentum commensurate with either a 10K or 50K gas (i.e. 67.96 ms⁻¹ for 10K, see *Table 3.3*; 151.97 ms⁻¹ for 50K, via *Equations 3.3* and *3.4*). Waters orientated ‘oxygen-first’ towards the surface deposited successfully at both temperatures. The ‘hydrogen-first’ water at 50K deposited successfully (having enough momentum to overcome the initial H-H repulsion and enter the regime where attractive O-H Coulombic and O-O dispersive forces dominate), while the analogous molecule at 10K was reflected (*see Figure 4.33*).

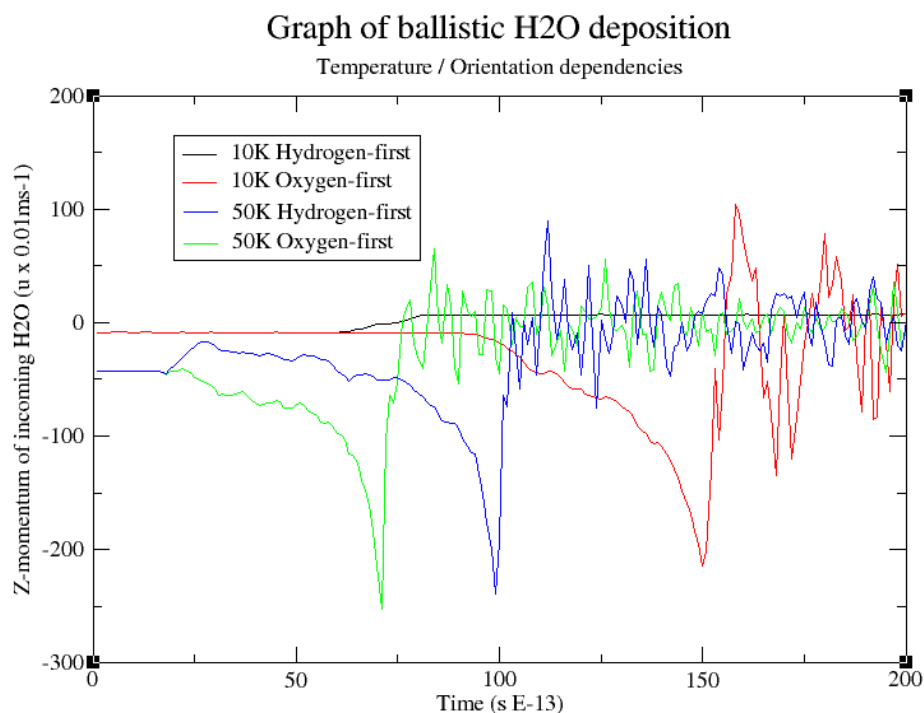


Figure 4.33: Reflection of low-velocity incoming water molecules occurs only when they are orientated hydrogen-first. The green, blue, and red lines show descent, acceleration, impact, and surface libration, while the black line representing 10K hydrogen-first is repelled away from the surface and never impacts.

Although this analysis confirms an orientational dependence in the water-on-ice depositions, the results from the deposition on silica suggest that it is not a specific consequence of an *ordered* polar surface. The simulated silica-water interaction is never repulsive at long distances; it is zero above r_{cut} and attractive between r_{cut} and the σ value of the oxygen-SiO₂ Lennard-Jones interaction (i.e. between 14Å and 2.939Å, see *Table 3.2* and *Figure 2.4*). This means a silica surface cannot repel water molecules; and yet in *Section 4.3* the silica substrates are seen to have comparable numbers of failed depositions to the cubic ice substrates. It seems that in the simulations the developing amorphous surface must also be able to repel incoming water molecules under certain orientations – i.e., once a water layer has begun to build up on top of the silica substrate, like-charge repulsion may occur to reflect new incoming molecules.

The numbers of failed depositions are higher at low deposition temperatures for two reasons: long low-T time-of-flight as explained in *Section 3.7*, and low-T inability to

overcome electrostatic reflection when orientated in such a way that homopolar groups interact. It may also be the case that slow collisions bring with them too little kinetic energy to induce surface rearrangement, thereby leaving deposited molecules in relatively high-energy surface sites. From these locations, the energy barrier to re-sublimation will be lower, and molecules have more chance of evaporating from the surface as the simulation progresses.

4.9 - Astrochemical Implications

In the laboratory ^[114] and in simulation ^[62], amorphous ice is often produced by rapidly quenching liquid water, the rationale being that HGW is sufficiently similar to PVD-ASW that this form of setup still produces ices that are astronomically relevant. Our research indicates that, particularly in the coldest temperature regimes at the core of molecular clouds, this assumption may not be valid. Amorphous solid water structures formed at 10K have a significantly different structure to those formed at higher temperatures, with long ice filaments providing a larger surface area and increased chance of cavitation. Such structures, when built up further, should provide more sites for surface chemistry reactions (potentially affecting the stochastic limits of chemical networks; see *Section 1.3*), as well as more adsorption sites – allowing them to function as more efficient stores for other ISM gas particles. Even if the *surface* is broadly of similar structure in vapour-deposited ASW and bulk-solidified HGW, the structure beneath the surface may evolve pores differently, regarding their interconnectedness and diameter distribution (as suggested in *Section 4.7*); all these are important considerations regarding the relevance of different laboratory studies.

These results may also inform understanding of ice radiolytic processes (*Equations 1.12 – 1.15*). The domination of thin, tower-like structures, only a handful of molecules thick, will improve the probability of radical escape from the ice matrix and lower the probability of radical-radical recombination, such as the formation of dihydrogen or methanol ^[10]. This may also decrease the concentration of OH in cold ices and thereby likewise decrease the adsorbed peroxide concentration, affecting internal ice chemistry (*Equations 1.12 and 1.13*).

Surface occlusion – while expected to tend towards total coverage as the ice layer grows thicker – could play a role in maintaining available surface sites for substrate-specific Eley-Rideal or Langmuir-Hinshelwood reactions which work at different rates depending on the structure of the surface. The partial occlusions seen in our study are also suggested by certain observational studies, specifically the combined presence in IR spectra of chemisorbed CO bands (absorbed onto bare grain surfaces) and adsorbed H₂O in the same regions ^[115].

However, ‘bare’ grain surfaces may not be ‘accessible’ grain surfaces; even when not occluded along a line of sight, many of these sites remain at the bottom of rain shadows, leaving them effectively inaccessible for incoming molecules – particularly slow-moving ones. We can also consider the likely effect on the albedo. We anticipate that amorphous ice will have a slightly lower albedo than crystalline water, but the effect will be much more pronounced in a grain where it is dark, non-occluded silicate grain surface which is left open to space ^[116]. This will allow the dust particles to absorb, rather than reflect, more radiation, and could contribute to more rapid heating (and hence ice restructuring and outgassing, see *Figure 1.14*) around a circumstellar core, which will again affect chemical network models when accounting for the rate of material replenishment from grain-surface reservoirs.

Chapter 5 – Conclusions

5.1 – Overview

In this work we have used classical Molecular Dynamics simulations to model the formation and structures of amorphous solid water ices under astrophysical conditions. We conclude that chemical vapour deposited water produces amorphous solid (rather than crystalline) ice films for all gas temperatures 10-300K and all surface temperatures 10-130K *and* both silica and I_c surfaces. Higher temperatures, particularly of the surface, tended to produce more flat, uniform structures, while lower temperatures produced tall, tower-like structures. The hydrophobic silica substrate exhibited less surface coverage and (in general) taller towers than the hydrophilic I_c surface.

During the process of deposition, the tower-like ASW structures produce ‘rain shadows’, occluding the surface from direct bombardment and instead accruing further material onto the top and sides of existing structures. The preferred geometry of newly-deposited molecules is found to be largely independent of temperature, with most molecules only forming one or two hydrogen bonds when they initially adhere to the growing ice structure.

The rain shadows produced particularly at lower temperatures leave substrate surfaces which may be only partially covered with adsorbed molecules but nonetheless are blocked from further interaction with the interstellar gas due to overhanging structures higher above. The effect diminishes as temperature increases, allowing better step-down surface migration and shifting the distribution of deposited matter closer to the grain: Volmer-Weber growth giving way to partial Volmer-Weber / Stranski-Krastanow growth. Consequently, cavitation is suppressed by high temperatures, and it is the ice layers formed in the cold cores of Bok globules which are likely to accommodate the greatest volume of extrinsic gas.

No clear trends were observed with regards to the hydrogen-bond deposition geometry, so we infer that, if structural rearrangement takes place, it does so as part of medium-term thermalisation with the surface, rather than fast kinetics immediately after deposition.

5.2 – Further Work

We mentioned in *Section 1.1* that key aims of the work were to contribute to the understanding of the small-scale structure of this astronomical amorphous ice, and to determine how different surfaces and temperatures may affect the ices' growth mechanism. Our simulations demonstrate that the structures produced proceed from tall towers which poorly cover the surface at 10K, to wetting-layer type flat structures which obscure the surface more effectively. The temperature of the incoming water molecules is most important in determining the overall height of the structures, but higher surface temperature also decreases structure height.

There are various additional avenues down which this work could be taken. For a quantitative measure of the dynamic stability of the ices, mean square displacement analyses of the migration of water molecules in an equilibrated structure could be accomplished with a time-dependent positional autocorrelation function. The actual effective surface area of the uneven ice structures could be determined by adapting the volume-occupancy algorithms ^[107] to measure exposed surface area as well (although, as in the volume analysis, distinguishing between astrochemically accessible surface area and cavity or rain shadow areas may be difficult). These features could be extracted simply by coding additional analysis algorithms. The present methodology *produces* the necessary data in the form of iterative structures – it is merely a case of *extracting* it.

In the medium term, a great deal of benefit could derive from optimally parallelizing the code such that it becomes tractable to run depositions on significantly larger systems ^[121]. As mentioned in *Section 4.6*, depositing more molecules would allow a better 'bulk-like' phase to accrue below the actual top surface of the deposited ice;

although other sources indicate that the cold structures are liable to remain filamentous even as more water accrues, 500 molecules was perhaps too small a number to unequivocally specify this emerging trend.

In the longer term, the process might be reversed, and the structures accrued by deposition could be heated to desorption. In order to simulate the laboratory method of temperature programmed desorption, the thermostat might be sequentially ramped to a specified higher temperature, and the evaporation of water molecules measured based on those which rise above a certain height beyond the substrate. Measuring the progress of pore collapse would be particularly interesting, as this is expected to be the means by which the interstellar medium is replenished with adsorbed gas molecules.

References

- [1] Arnett, D., Supernovae and Nucleosynthesis (textbook), *Princeton University Press*, **1996**
- [2] Fisenko, A. I., Malomuzh, N. P.; The role of the H-bond network in the creation of the life-giving properties of water, *Chem. Phys.*, **345**, 164-172, **2008**
- [3] Atkins, P., de Paula, A., Atkins' Physical Chemistry 7th Edition (textbook), *Oxford University Press*, **2002**
- [4] Harwit, M., *Adv. Space Res.*, **30** (9), 2151, **2002**
- [5] Snell, R. L., Howe, J. E., Ashby, M. L. N., Bergin, E. A., Chin, G., Erickson, N. R., Goldsmith, P. F., Harwit, M., Kleiner, S. C., Koch, D. G., et al., *The Astrophysical Journal*, **539**, L101-L105, **2000**
- [6] Ioppolo S, Cuppen HM, Romanzin C, et al; Laboratory evidence for efficient water formation in interstellar ices; *Astrophysical Journal*, **686** (2), 1474-1479, **2008**
- [7] Nisini, B., Giannini, T., Neufeld, D. A., Yuan, Y. A., Antoniucci, S., Bergin, E. A., Melnick, G.J., Spitzer Spectral Line Mapping of Protostellar Outflows. II. H(2) Emission in L1157, *Astrophysical Journal* **724**, 69-79, **2010**
- [8] van Dishoeck, E. F., Kristensen, L. E., et al, Water in Star-Forming Regions with the Herschel Space Observatory (WISH): Overview of key programme and first results, *Publications of the Astronomical Society of the Pacific*, **123**, 138-170, **2011**
- [9] Aikawa, Y.; Ohashi, N.; Herbst, E.; Molecular Evolution in Collapsing Prestellar Cores. II. The Effect of Grain-Surface Reactions, *The Astrophysical Journal*, **593** (2), 906-924, **2003**
- [10] Tielens, A.G.G.M., The Physics and Chemistry of the Interstellar Medium (textbook), *Cambridge University Press*, **2005**
- [11] McCullough, P., photograph from the Hubble Space telescope STScI/ AURA surveys, **2006**
- [12] Whittet, D.C.B.; Cook, A.M.; Chiar, J.E.; Pendleton, Y.J.; Shenoy, S.S.; Gerakines, P.A., The nature of carbon dioxide bearing ices in quiescent molecular clouds *Astrophysical Journal*, **695** (1), 94-100, **2009**
- [13] Images reproduced from the website of the Associated Universities Inc., <http://www.aui.edu/pr.php?id=20081114>, **2009**
- [14] Dulieu, F., Amiaud, L., Conigu, E., Fillion, J. H., Matar, E., Momeni, A., Pironello, V., Lemaire, J. L.; Experimental evidence for water formation on interstellar dust grains by hydrogen and oxygen atoms; *Astronomy & Astrophysics* **512**, A30; **2010**
- [15] Visser, R., van Dishoeck, E. F., Doty, S. D., Dullemond, C. P., The Chemical History of Molecules in Circumstellar Disks I. Ices, *Astronomy & Astrophysics*, **495**, 881-897, **2009**
- [16] Horner, J., Mousis, O., Hersant, F., Constraints on the Formation Regions of Comets from their D:H Ratios, *Earth, Moon, and Planets*, **100**, 43-56, **2007**
- [17] Millar, T. J., Bennett, A., Herbst, E., Deuterium Fractionation In Dense Interstellar Clouds, *Astrophysical Journal*, **340**, 906-920, **1989**

- [18] Notesco, G.; Laufer, D.; Bar-Nun, A., The formation temperature of comets Halley, Hyakutake and Hale-Bopp, *1st International Conference on Comet Hale-Bopp, Tenerife, Spain, Feb 02-05; Tenerife, Spain*, 237, **1998**
- [19] Herbst, E.; Astrochemistry in the gas and on dust particles (textbook), *Proceedings of the dusty and molecular universe: a prelude to Herschel and ALMA*, **2005**
- [20] Cazaux, S., Minissale, M., Dulieu, F., and Hocuk, D, Dust as interstellar catalysis; How chemical desorption impacts the gas, *Astronomy & Astrophysics*, 585, **2016**
- [21] Garrod, R.T., A new modified-rate approach for gas-grain chemical simulations, *Astronomy & Astrophysics (Manuscript 0518)*, **2008**
- [22] Cazaux, S. and Hocuk, S., Interplay of gas and ice during cloud evolution, *Astronomy & Astrophysics*, 576, **2015**
- [23] Garrod, R.T., Complex Chemistry in Star-Forming Regions: An Expanded Gas-Grain Warm-up Chemical Model, *The Astrophysical Journal*, 682 (1), 283-302, **2008**
- [24] Asvany, O., Kumar, P., Redlich, B., Hegemann, I., Schlemmer, S., Marx, D., Understanding the infrared spectrum of bare CH₅⁺, *Science*, **309**, 1219-1222, **2005**
- [25] Geppert, W. D.; Thomas, R.; Semaniak, J.; Ehlerding, A.; Millar, T. J.; Österdahl, F.; afUggla, M.; Djurić, N.; Paál, A.; Larsson, M; Dissociative Recombination of N₂H⁺: Evidence for Fracture of the NN Bond, *The Astrophysical Journal*, 609, (1), 459-464, **2004**
- [26] Chastaing, D.; Le Picard, S. D.; Sims, I. R.; Smith, I. W. M.; Rate coefficients for the reactions of C(³P) atoms with C₂H₂, C₂H₄, CH₃C = CH and H₂C = C = CH₂ at temperatures down to 15 K; *Astronomy and Astrophysics*, 365, 241-247**2001**
- [27] Vidali, G., Li, L.; Roser, J. E.; Badman, R., Catalytic activity of interstellar grains: Formation of molecular hydrogen on amorphous silicates, *Advances in Space Research*, (43) 1291-1298, **2009**
- [28] Hornekaer, L., Baurichter, A., Petrunin, V.V., Field, D., Luntz, A.C., Importance of surface morphology in interstellar H-2 formation, *Science*, 203, 5652, **2003**
- [29] Pat-El, I.; Laufer, D.; Notesco, G.; Bar-Nun, A., An experimental study of the formation of an ice crust and migration of water vapor in a comet's upper layers. *Icarus*, 201(1), 406-411, **2009**
- [30] Minissale, M., Congiu, E., Manico, G, Pirronello, V., and Dulieu, F., CO₂ formation on interstellar dust grains; a detailed study of the barrier of the CO + O channel, *Astronomy & Astrophysics*, 559, **2013**
- [31] Oba, Y.; Miyauchi, N.; Hidaka, H.; Chigai, T.; Watanabe, N.; Kouchi, A.; Formation of compact Amorphous H₂O ice by codeposition of hydrogen atoms with oxygen molecules on grain surfaces, *Astrophysical Journal*, 701 (1), 464-470, **2009**
- [32] Noble, J. A., Dulieu, F., Congiu, E., Fraser, H. J., CO(2) formation in quiescent clouds: an experimental study of the CO + OH pathway, *Astrophysical Journal*, 735, 121, **2011**

- [33] Eisenberg, D. K.; Structure and properties of water (textbook), *Oxford University Press*, **2005**
- [34] Suresh, S. J.; Naik, V.M.; Hydrogen bond thermodynamic properties of water from dielectric constant data, *J. Chem. Phys.*, *113*, 9727-9732, **2000**
- [35] Marion, G. M.; Jakubowski, S. D.; The compressibility of ice to 2.0 kbar, *Cold Regions Sci. Tech.*, *38*, 211-218, **2004**
- [36] Tanaka, H.; Simple physical explanation of the unusual thermodynamic behavior of liquid water, *Phys. Rev. Lett.*, *80*, 5750-5753, **1998**
- [37] Ehrenfreund, P.; Fraser, H. J.; Blum, J.; Cartwright, J. H. E.; Garcia-Ruiz, J. M.; Hadamcik, E.; Lvasseur-Regourd, A. C.; Price, S.; Prodi, F.; Sarkissian, A., Physics and chemistry of icy particles in the universe: answers from microgravity. *Planetary and Space Science*, *51*(7-8), 473-494, **2003**
- [38] Guillot, B., Guissani, Y., Polyamorphism in low temperature water: A simulation study, *J. Chem Phys*, *119* (22), **2003**
- [39] Paschek, D., Ruppert, A., Geiger, A.; Thermodynamic and Structural Characterization of the Transformation from a Metastable Low-Density to a Very High-Density Form of Supercooled TIP4P-Ew Model Water, *Chem. Phys. Chem.*, *9*, 2737 – 2741, **2008**
- [40] Martonak, R.; Donadio, D., Parrinello, M.; Polyamorphism of Ice at Low Temperatures from Constant-Pressure Simulations, *Phys. Rev. Letters*, *92* (22), **2004**
- [41] Chen, S.H., Zhang, Y., Lagi, M., Chong, S. H., Baglioni, P., Mallamace, F.; Evidence of dynamic crossover phenomena in water and other glass-forming liquids: experiments, MD simulations and theory; *J. Phys.: Condens. Matter*, *21*, 504102, **2009**
- [42] Geiger, A; Brovchenko, I.; Oleinikova, A., Liquid-liquid phase transitions in supercooled water studies by computer simulations of various water models, *J. Chem Phys.*, *123*, 044515, **2005**
- [43] Loerting, T., Giovambattista, N.; Amorphous ices: experiments and numerical simulations; *J. Phys.: Condens. Matter*, *18*, R919–R977, **2006**
- [44] Zhang, Q., Buch, V.; Computational study of formation dynamics and structure of amorphous ice condensates, *J. Chem. Phys*, *92* (8), 5004, **1990**
- [45] Kimmel, G. A., Dohnalek, Z., Stevenson, K. P., Smith, R. S., Kay, B. D.; Control of amorphous solid water morphology using molecular beams. II. Ballistic deposition simulations, *J. Chem. Phys.*, *114* (12), **2001**
- [46] Rowland, B., Kadagathur, N. S., Devlin, J. P., Buch, V., Feldman, T., et al., Infrared spectra of ice surfaces and assignment of surface localized modes from simulated spectra of cubic ice, *J. Chem. Phys*, *102*, 8328, **1995**
- [47] Escribano, B., Cartwright, J.H.E., Ignacio Sainz-Diaz, C., Ice films follow structure zone model morphologies, *Thin solid films*, 518, **2010**
- [48] Visser, R., van Dishoeck, E. F., Doty, S. D., The Chemical History of Molecules in Circumstellar Disks II. Gas-phase species, *Astronomy & Astrophysics*, *534*, A132, **2011**
- [49] Watanabe, N., Kouchi, A.; Ice surface reactions: A key to chemical evolution in space; *Progress in Surface Science*, *83*, 10-12, **2008**

- [50] Vilaplana, R.; Gomis, O.; Satorre, M. A.; Luna, R.; Canto, J.; Domingo, M.; Millán, C.; Santoja, C., Lecture Notes and Essays in Astrophysics, vol. 3., *Proceedings of the 3rd Symposium of the Astrophysics Group of the Spanish Royal Physical Society (Real Sociedad Española de Física, RSEF), September 2007*, 201-212, **2007**
- [51] Fraser, H. J., Collings, M. P., McCoustra, M. R. S., Laboratory surface astrophysics experiment, *Review of Scientific Instruments*, **73**, 2161, **2002**
- [52] Al-Halabi, A., Fraser, H.J., Kroes, G.J., van Dishoeck, E.F. Adsorption of CO on amorphous water-ice surfaces. *Astronomy & Astrophysics*, **422**, 777-791, **2004**
- [53] Al-Halabi, A.; Kroes, G.J.; van Dishoeck, E.F.; Sticking of CO to crystalline and amorphous ice surfaces, *J. Chem. Phys.*, **120** (7), **2004**
- [54] Manca, C., Martin, C., Roubin, P., Adsorption of small molecules on amorphous ice: volumetric and FT-IR isotherm co-measurements - Part II. The case of CO, *Surface Science*, **502**, 280-284, **2002**
- [55] Collings, M.P.; Dever, W.J.; Fraser H.J., McCoustra, M.R.S., Williams, D.A., Carbon monoxide entrapment in interstellar ice analogues, *The Astrophysical Journal*, **583**, 1058–1062, **2003**
- [56] Palumbo, M. E., Infrared spectra and the nature of the principal CO trapping sites in amorphous and crystalline H₂O ice, *J. Phys. Chem.*, **101**, 4298-4301, **1997**
- [57] Pontoppidan, K. M., Fraser, H. J., Dartois, E., Thi, W. F., van Dishoeck, E. F., Boogert, A. C. A., d'Hendecourt, L., Tielens, A. G. G. M., Bisschop, S. E., A 3-5 μ m VLT spectroscopic survey of embedded young low mass stars I - Structure of the CO ice, *Astronomy & Astrophysics*, **408**, 981, **2003**
- [58] Jenniskens, Blake; Structural Transitions in Amorphous Water Ice and Astrophysical Implications; *Science*, **285**, **1994**
- [59] Gibb, E.L.; Whittet, D.C.B.; Boogert, A.C.A.; Tielens, A.G.G.M., Interstellar ice: The Infrared Space Observatory legacy. *Astrophysical Journal Supplement Series*, **151**(1), 35-73, **2004**
- [60] Gibb, E. L., Whittet, D. C. B., Schutte, W. A., An inventory of interstellar ices toward the embedded protostar W33A, *Astrophysical Journal* **536**, 347-356, **2000**
- [61] Whittet, D.C.B., Infraredspectroscopy of interstellar ices, *NATO Advanced Study Institute / 3rd Course of the International School of Space Chemistry - Cosmic Dust Connection, Erice, Italy*, 133-154, **1994**
- [62] Al-Halabi, A., Andersson, S.; Molecular-dynamics study of photodissociation of water in crystalline and amorphous ices, *J. Chem. Phys.*, **124**, 064715, **2006**
- [63] Arasa, C., Andersson, S., Cuppen, H. M., van Dishoeck, E. F., Kroes, G. J., Molecular dynamics simulations of the ice temperature dependence of water ice photodesorption, *J. Chem. Phys.*, **132**(18), **2010**
- [64] Collings, M. P., Anderson, M. A., Chen, R., Dever, J. W., Viti, S., Williams, D. A., McCoustra, M. R. S., A laboratory survey of the thermal desorption of astrophysically relevant molecules, *Monthly Notices of the Royal Astronomical Society*, **354**, 1133-1140, **2004**

- [65] Gibson, K. D., Killelea, D. R., Yuan, H., Becker, J. S., Sibener, S. J., Determination of the sticking coefficient and scattering dynamics of water on ice using molecular beam techniques, *J. Chem. Phys.*, **134**, **2011**
- [66] Fraser, H. J., Collings, M. P., Dever, J. W., McCoustra, M. R. S., Using laboratory studies of CO-H₂O ices to understand the non-detection of a 2152cm⁻¹ (4.647μ) band in the spectra of interstellar ices, *Monthly Notices of the Royal Astronomical Society*, **353**, 58-69, **2004**
- [67] Frenklach, Michael; Feigelson, Eric D.; Formation of polycyclic aromatic hydrocarbons in circumstellar envelopes; *Astrophysical Journal*, (341) 372-384, **1989**
- [68] Millar, T.J.; The chemistry of PAH and fullerene molecules in interstellar clouds; *Royal Astronomical Society, Monthly Notices*, **259** (3), 35P-39P, **1992**
- [69] Smith, W., Forester, T.R., DL_POLY 2.0: A general-purpose parallel molecular dynamics simulation package, *Journal of Molecular Physics*, **14**(3), **1996**
- [70] Kim, B., Choe, J., Determination of Proper Time Step for Molecular Dynamics Simulation, *Bull.Korean. Chem. Soc.*, **21**, 419, **2000**
- [71] Winger, M., Trzesniak, D., Baron, R., van Gunstern, W. F., On using a too large integration timestep in molecular dynamics simulations of coarse-grained molecular models, *Phys. Chem. Chem. Phys.*, **11**, 1934-1941, **2009**
- [72] Hoover, W.G., *Phys. Rev. A*, **31**, 1695, **1985**
- [73] Hoover, W.G., *Phys. Rev. A*, **34**, 2499, **1986**
- [74] Berendsen, H. J. C., Postma, J. P. M., van Gunsteren, W. F., DiNola, A., Haak, J. R., Molecular Dynamics with coupling to an external heat bath, *J. Chem. Phys.*, **81**, 3684, **1984**
- [75] Allen, M.P., Tildesley, D.J., Computer simulation of liquids (textbook), *Clarendon Oxford Press*, **1987**
- [76] Roux, B., Simonson, T.; Implicit Solvent Models, *Biophysical Chemistry*, (78) 1-20, **1998**
- [77] Birkett, G.R., Do, D.D.; PVT behaviour of fluids with potential models optimised for phase equilibria, *Fluid Phase Equilibria*, **224** (2), **2004**
- [78] Jorgensen, W.L., Chandrasekhar, J., Madura, J.D., Klein M.L., Impey R.W.; Comparison of simple potential functions for simulating water, *J. Chem. Phys.*, **79** (2), 926, **1983**
- [79] Finney, J.L., The water molecule and its interactions: the interaction between theory, modelling, and experiment, *J. Mol. Liq.*, **90**, 303, **2001**
- [80] Guillot, B.; A reappraisal of what we have learnt during three decades of computer simulations on water, *J. Mol. Liq.*, **101**, 219, **2002**
- [81] Abascal, J.L.F., Sanz, E., Fernández, R.G., Vega, C.; A potential model for the study of ices and amorphous water: TIP4P/Ice, *J. Chem. Phys.*, **122**, 234511, **2005**
- [82] Mahoney, M.W., Jorgensen, W.L.; A five-site model for liquid water and the reproduction of the density anomaly by rigid, nonpolarizable potential functions, *J. Chem. Phys.*, **112**, 8910, **2000**
- [83] Nada, H., van der Eerden, J.P.J.M.; An intermolecular potential model for the simulation of ice and water near the melting point: A six-site model for H₂O, *J. Chem. Phys.*, **118**, (16), 7401, **2003**

- [84] Izvekov, S., Voth, G.A.; Multiscale coarse graining of liquid-state systems, *J. Chem. Phys.*, *123* (13), 134105, **2005**
- [85] Smith, R. S., Kay, B. D., The existence of supercooled liquid water at 150K, *Nature*, *398*, 788, **1999**
- [86] Daschbach, J. L., Gregory, K., Schenter, K., Ayotte, P., Smith, R. S., Kay, B. D., Helium Diffusion through H₂O and D₂O amorphous ices: Observation of a lattice inverse isotope effect, *Phys. Rev. Letters*, *92*, 198306, **2004**
- [87] Wikfeldt, K.T., Leetmaa, M., Ljungberg, M. P., Nilsson, A. and Pettersson, L.G.M., On the range of water structure models compatible with X-ray and neutron diffraction data, *J. Phys. Chem. B*, *113*, 6246-6255, **2009**
- [88] Pusztai, L., Pizio, O., and Sokolowski, S., Comparison of interaction potentials of liquid water with respect to their consistency with neutron diffraction data of pure heavy water, *J. Chem. Phys.*, *129*, 184103, **2008**
- [89] Paschek, D.; Ruppert, A.; and Geiger, A.; Thermodynamic and Structural Characterization of the Transformation from a Metastable Low-Density to a Very High-Density Form of Supercooled TIP4P-Ew Model Water, *Chem. Phys. Chem*, *9*, 2737 – 2741, **2008**
- [90] Abascal, J.L.F., Vega, C.; A general purpose model for the condensed phases of water: TIP4P/2005, *J. Chem. Phys.*, *123*, **2005**
- [91] Matar, E., Bergeron, H., Dulieu, F., Chaabouni, H., Accolla, M., Lemaire, J.L.; Gas temperature dependent sticking of hydrogen on cold amorphous water ice surfaces of interstellar interest, *J. Chem. Phys.*, *113*, **2010**
- [92] Essmann, U.; Geiger, A.; Molecular dynamics simulation of vapor deposited amorphous ice; *J. Chem. Phys.*, *103* (11), **1995**
- [93] Sceats, M.G.; Rice, S.A.; Water, A Comprehensive Treatise (textbook), *Plenum, New York*, *7*, **1982**
- [94] Horn, H.W.; Swope, W.C.; Pitara, J.W.; Madura, J.D.; Dick, T.J.; Hura, G.L.; Head-Gordon, T.; Development of an improved four-site water model for biomolecular simulations: TIP4P-Ew, *J. Chem. Phys.*, *120*, 9665, **2004**
- [95] Pi, H. L., Aragones, J. L., Vega, C., Noya, E. G., Abascal, J. L. F., Gonzales, M. A., McBride, C.; Anomalies in water as obtained from computer simulations of the TIP4P/2005 model; density maxima, and density, isothermal compressibility and heat capacity minima; *Mol. Phys.*, *107*, **2009**
- [96] Arasa, C., Andersson, S., Cuppen, H. M., van Dishoeck, E. F., Kroes, G. J.; Molecular dynamics simulations of the ice temperature dependence of water ice photodesorption; *J. Chem. Phys.*, *132*, 184510, **2010**
- [97] Narten, A.H., Thiessen, W.E., Blum, L.; Atom pair distribution functions of liquid water at 25°C from neutron diffraction, *Science* *217*, 1033-1034, **1982**
- [98] Narten, A.H., Danford, M.D., Levy H.A.; X-ray diffraction study of liquid water in the temperature range 4-200°C, *Faraday Discussions* *43*, 97-107, **1967**
- [99] Yang, J., Meng, S., Xu, L.F., Wang, E.G., Ice Tessellation on a Hydroxylated Silica Surface, *Phys. Rev. Letters*, *92* (14), **2004**
- [100] Humphrey, W., Dalke, A., Schulten, K.; VMD – Visual Molecular Dynamics; *J. Molec. Graphics*, *14.1*, 33-38, **1996**
- [101] Suga, H.; A facet of recent ice sciences; *ThermochimicaActa*, *300*, 117-126, **1997**

- [102] de Koning, M., Antonelli, A.; Modelling equilibrium concentrations of Bjerrum and molecular point defects and their complexes in ice Ih; *J. Chem. Phys.*, 126 (16), 164502, **2008**
- [103] Rahman, A., Stillinger, F.H., Proton Distribution in Ice and the Kirkwood Correlation Factor, *J. Chem. Phys.*, 57 (6), **1972**
- [104] Adams, D.J.; Monte Carlo calculations for the ice-rules model, with and without Bjerrum defects; *J. Phys. Chem., Solid State Phys.*, 17, 4063-4070 **1984**
- [105] Rick, S.W., Haymet, A.D.J., Dielectric constant proton order and disorder in ice Ih: Monte Carlo computer simulations *J. Chem. Phys.*, 118 (20), **2003**
- [106] Zhang, Y., Xu, Z.; Atomic radii of noble gas elements in condensed phases, *American Mineralogist*, (80), 670-675, **1995**
- [107] Truhlar, D. G., Cramer, C. J. et al; Improved Methods for Semiempirical Solvation Models, *J. Comp. Chem.*, 16, 4, **1995**
- [108] Cazaux, S., Bossa, J.-B., Linnartz, H., Tielens, A.G.G.M., Pore evolution in interstellar ice analogues, simulating the effects of temperature increase, *Astronomy & Astrophysics*, 573, **2015**
- [109] Isokoski, K., Bossa, J.B., Triemstra, T., Linnartz, H., Porosity and thermal collapse measurements of H₂O, CH₃OH, CO₂, and H₂O:CO₂ ices, *Physical Chemistry – Chemical Physics*, 16:8, **2014**
- [110] Koudriachova, M. V., Beckers, J. V. L., de Leeuw, S. W.; Computer simulation of the quartz surface: a combined ab initio and empirical potential approach, *Comp. Mat. Sci.*, 20, 381-386, **2001**
- [111] Gupta, R. P.; Lattice relaxation at a metal surface, *Phys. Rev. B*, (23), 6265-6271, **1981**
- [112] Soper, A. K.; The radial distribution function of water and ice from 220 to 673K and at pressures up to 400 MPa; *Chem. Phys.*, 258, 121-137, **2000**
- [113] Garrod, R.T., Three-dimensional off-lattice monte carlo kinetics simulations of interstellar grain chemistry and ice structure, *The Astrophysical Journal*, 778, **2013**
- [114] Mate, B., Rodriguez-Lazcano, Y., Herrero, V.J., Morphology and crystallization kinetics of compact (HGW) and porous (ASW) amorphous water ice, *Physical Chemistry – Chemical Physics*, 14(30), **2012**
- [115] Noble, J.A., Fraser, H.J., Aikawa, Y., Pontoppidan, K.M., Sakon, I., A survey of H₂O, CO₂, and CO ice features towards the background stars and low-mass young stellar objects using Akari, *The Astrophysical Journal*, 775:85, **2013**
- [116] Davies, J. K., Roush, T. I., Cruikshank, D. P., Bartholomew, M. J., Geballe, T. R., Owen, T., de Bergh, C.; The Detection of Water Ice in Comet Hale-Bopp; *Icarus*, 127, 238-245, **1997**
- [117] Delsemme, A. H., The deuterium enrichment observed in recent comets is consistent with the cometary origin of seawater. *Planetary and Space Science*, 47(1-2), 125-131, **1999**
- [118] Okabe I., Tanaka H., Nakanishi K.; Structures and Phase Transitions of Amorphous Ices, *Phys. Rev. E*, 53 (3), **1996**

- [119] Fraser, H. J.; Collings, M. P.; McCoustra, M. R. S.; Williams, D. A., Thermal desorption of water ice in the interstellar medium. *Monthly Notices of the Royal Astronomical Society*, 327(4), 1165-1172, **2001**
- [120] Chen, B; Xing, J.H.; Siepmann, J.I.; Development of polarizable water force fields for phase equilibrium calculations, *J. Phys. Chem. B*, 104(10), 2391, **2000**
- [121] Griebel, M, Knapek, S., Zumbusch, G.; Numerical Simulation in Molecular Dynamics (book), *Springer-Verlag*, **2007**

Appendices

These appendices contain the raw numerical information from each of the 90 simulations: ice structure heights, volumes, surface properties, and deposition bond orientations. As with the results *Sections 4.3* and *4.4*, they are divided up into static and dynamic results sections. All the information given here is displayed graphically in *Chapter 4* and discussed there; the base data is included here simply for completeness.

Appendix A - Static structure results

Tables 7.1 – 7.18: Static results for each individual simulation run. See Sections 4.5 – 4.8 for diagrams and discussion of these results.

7.1: Static Results for 10K deposition on 10K water substrate						
Run	Average Height (Å)	Median Height (Å)	Maximal Height (Å)	Substrate Relaxation (Å)	Volume Occupancy	Substrate Occlusion
1	24.845	21.647	61.138	0.088	0.250	0.666
2	54.879	61.085	100.598	0.078	0.162	0.661
3	34.899	28.611	74.952	0.846	0.195	0.800
4	50.515	50.752	92.204	0.080	0.176	0.651
5	29.206	33.659	65.335	0.093	0.269	0.682
Avr	38.869	39.151	78.845	0.085	0.211	0.692

7.2: Static Results for 10K deposition on 10K silica substrate						
Run	Average Height (Å)	Median Height (Å)	Maximal Height (Å)	Substrate Relaxation (Å)	Volume Occupancy	Substrate Occlusion
1	28.247	25.787	67.738	-0.011	0.254	0.801
2	48.656	51.591	87.196	0.016	0.214	0.747
3	27.518	25.836	61.370	0.001	0.281	0.768
4	35.326	31.543	75.516	0.007	0.241	0.772
5	21.782	17.397	55.007	-0.008	0.314	0.759
Avr	32.305	30.431	69.365	0.001	0.261	0.773

<i>7.3: Static Results for 150K deposition on 10K water substrate</i>						
Run	Average Height (Å)	Median Height (Å)	Maximal Height (Å)	Substrate Relaxation (Å)	Volume Occupancy	Substrate Occlusion
1	14.501	11.036	34.768	0.072	0.406	0.821
2	12.679	11.907	29.915	0.077	0.444	0.809
3	12.721	10.273	32.718	0.097	0.401	0.876
4	11.748	11.144	26.175	0.105	0.508	0.850
5	11.666	9.830	28.843	0.085	0.454	0.851
Avr	12.663	10.838	30.484	0.087	0.443	0.841

<i>7.4: Static Results for 150K deposition on 10K silica substrate</i>						
Run	Average Height (Å)	Median Height (Å)	Maximal Height (Å)	Substrate Relaxation (Å)	Volume Occupancy	Substrate Occlusion
1	21.931	22.752	42.426	0.000	0.389	0.724
2	21.644	18.127	52.518	-0.007	0.309	0.630
3	19.399	19.256	49.110	-0.001	0.339	0.755
4	22.639	23.309	50.907	-0.003	0.331	0.809
5	19.009	15.635	50.649	-0.012	0.324	0.788
Avr	20.924	19.816	49.122	-0.005	0.338	0.741

<i>7.5: Static Results for 300K deposition on 10K water substrate</i>						
Run	Average Height (Å)	Median Height (Å)	Maximal Height (Å)	Substrate Relaxation (Å)	Volume Occupancy	Substrate Occlusion
1	14.994	10.491	46.231	0.094	0.310	0.856
2	10.418	9.140	28.062	0.134	0.452	0.917
3	11.788	11.261	25.547	0.113	0.517	0.882
4	11.752	9.721	31.675	0.078	0.416	0.892
5	13.185	11.565	45.613	0.106	0.482	0.845
Avr	12.427	10.436	35.426	0.105	0.435	0.879

<i>7.6: Static Results for 300K deposition on 10K silica substrate</i>						
Run	Average Height (Å)	Median Height (Å)	Maximal Height (Å)	Substrate Relaxation (Å)	Volume Occupancy	Substrate Occlusion
1	17.039	15.325	39.675	-0.007	0.406	0.888
2	15.686	14.336	41.254	-0.016	0.392	0.862
3	11.835	9.598	31.788	-0.011	0.467	0.917
4	15.499	12.762	39.396	-0.004	0.391	0.726
5	14.519	10.730	40.501	-0.006	0.386	0.844
Avr	14.916	12.550	38.523	-0.009	0.408	0.848

<i>7.7: Static Results for 10K deposition on 60K water substrate</i>						
Run	Average Height (Å)	Median Height (Å)	Maximal Height (Å)	Substrate Relaxation (Å)	Volume Occupancy	Substrate Occlusion
1	25.338	24.587	57.563	0.106	0.267	0.682
2	24.861	20.841	69.662	0.123	0.215	0.712
3	15.357	15.521	35.642	0.135	0.387	0.819
4	17.721	15.697	42.045	0.100	0.342	0.789
5	28.435	28.266	63.995	0.119	0.232	0.508
Avr	22.435	20.982	53.781	0.116	0.288	0.702

<i>7.8: Static Results for 10K deposition on 60K silica substrate</i>						
Run	Average Height (Å)	Median Height (Å)	Maximal Height (Å)	Substrate Relaxation (Å)	Volume Occupancy	Substrate Occlusion
1	22.323	15.8676	60.309	0.051	0.283	0.873
2	24.028	20.364	59.483	0.034	0.285	0.668
3	27.291	24.539	68.731	0.030	0.255	0.663
4	20.409	18.255	49.891	0.049	0.337	0.849
5	16.220	12.000	44.655	0.038	0.366	0.800
Avr	22.054	18.205	56.614	0.041	0.305	0.771

<i>7.9: Static Results for 150K deposition on 60K water substrate</i>						
Run	Average Height (Å)	Median Height (Å)	Maximal Height (Å)	Substrate Relaxation (Å)	Volume Occupancy	Substrate Occlusion
1	17.106	15.292	40.007	0.121	0.361	0.787
2	11.731	9.887	29.898	0.093	0.443	0.877
3	10.358	9.116	27.080	0.125	0.481	0.896
4	11.855	9.558	33.831	0.129	0.404	0.873
5	11.201	9.144	32.268	0.139	0.423	0.918
Avr	12.450	10.599	32.617	0.121	0.423	0.870

<i>7.10: Static Results for 150K deposition on 60K silica substrate</i>						
Run	Average Height (Å)	Median Height (Å)	Maximal Height (Å)	Substrate Relaxation (Å)	Volume Occupancy	Substrate Occlusion
1	25.972	23.226	60.566	0.050	0.284	0.626
2	17.855	12.809	45.883	0.031	0.352	0.751
3	21.836	22.711	47.195	0.036	0.354	0.704
4	17.451	14.406	40.926	0.051	0.392	0.792
5	18.120	15.325	43.011	0.029	0.374	0.775
Avr	20.247	17.686	47.517	0.039	0.351	0.729

<i>7.11: Static Results for 300K deposition on 60K water substrate</i>						
Run	Average Height (Å)	Median Height (Å)	Maximal Height (Å)	Substrate Relaxation (Å)	Volume Occupancy	Substrate Occlusion
1	13.468	10.361	36.012	0.110	0.385	0.850
2	12.402	9.825	35.385	0.128	0.374	0.862
3	10.259	9.736	21.747	0.116	0.564	0.901
4	11.721	9.511	32.957	0.123	0.414	0.874
5	10.196	8.580	28.708	0.127	0.457	0.939
Avr	11.610	9.602	30.961	0.121	0.438	0.885

<i>7.12: Static Results for 300K deposition on 60K silica substrate</i>						
Run	Average Height (Å)	Median Height (Å)	Maximal Height (Å)	Substrate Relaxation (Å)	Volume Occupancy	Substrate Occlusion
1	9.843	9.097	21.887	0.024	0.672	0.965
2	11.965	10.965	29.353	0.036	0.510	0.876
3	15.725	13.533	37.428	0.029	0.404	0.775
4	15.030	13.773	35.355	0.028	0.448	0.814
5	15.884	14.609	44.572	0.021	0.356	0.765
Avr	13.689	12.395	33.719	0.027	0.478	0.839

<i>7.13: Static Results for 10K deposition on 130K water substrate</i>						
Run	Average Height (Å)	Median Height (Å)	Maximal Height (Å)	Substrate Relaxation (Å)	Volume Occupancy	Substrate Occlusion
1	17.426	16.114	40.779	0.211	0.349	0.732
2	29.639	29.521	64.069	0.212	0.239	0.499
3	23.285	23.132	56.512	0.174	0.272	0.725
4	15.587	14.111	38.120	0.189	0.373	0.804
5	22.735	23.265	47.967	0.161	0.303	0.675
Avr	21.735	21.229	49.489	0.189	0.307	0.687

<i>7.14: Static Results for 10K deposition on 130K silica substrate</i>						
Run	Average Height (Å)	Median Height (Å)	Maximal Height (Å)	Substrate Relaxation (Å)	Volume Occupancy	Substrate Occlusion
1	24.867	24.669	57.958	0.148	0.288	0.591
2	13.477	12.784	33.850	0.094	0.442	0.757
3	18.529	14.387	53.423	0.107	0.309	0.689
4	31.788	30.944	65.754	0.149	0.263	0.524
5	22.343	19.854	56.149	0.113	0.295	0.718
Avr	22.201	20.528	53.427	0.122	0.319	0.656

<i>7.15: Static Results for 150K deposition on 130K water substrate</i>						
Run	Average Height (Å)	Median Height (Å)	Maximal Height (Å)	Substrate Relaxation (Å)	Volume Occupancy	Substrate Occlusion
1	10.483	8.902	27.071	0.148	0.459	0.937
2	10.602	8.965	27.119	0.149	0.496	0.944
3	11.052	10.043	25.734	0.088	0.511	0.875
4	10.250	8.833	24.693	0.187	0.531	0.936
5	10.024	8.461	23.743	0.166	0.515	0.936
Avr	10.482	9.041	25.672	0.148	0.503	0.926

<i>7.16: Static Results for 150K deposition on 130K silica substrate</i>						
Run	Average Height (Å)	Median Height (Å)	Maximal Height (Å)	Substrate Relaxation (Å)	Volume Occupancy	Substrate Occlusion
1	13.436	11.414	34.829	0.104	0.443	0.771
2	16.788	13.656	42.114	0.104	0.387	0.741
3	12.551	11.259	31.004	0.072	0.496	0.859
4	11.856	9.849	30.244	0.117	0.491	0.861
5	11.507	10.207	27.400	0.093	0.545	0.828
Avr	13.228	11.277	33.118	0.098	0.473	0.812

<i>7.17: Static Results for 300K deposition on 130K water substrate</i>						
Run	Average Height (Å)	Median Height (Å)	Maximal Height (Å)	Substrate Relaxation (Å)	Volume Occupancy	Substrate Occlusion
1	9.489	9.061	20.627	0.195	0.576	0.959
2	9.189	8.659	21.512	0.196	0.546	0.967
3	10.213	8.652	26.087	0.169	0.482	0.941
4	8.950	8.641	17.729	0.171	0.664	0.968
5	8.954	8.335	19.255	0.195	0.611	0.966
Avr	9.359	8.669	21.042	0.185	0.576	0.961

<i>7.18: Static Results for 300K deposition on 130K silica substrate</i>						
Run	Average Height (Å)	Median Height (Å)	Maximal Height (Å)	Substrate Relaxation (Å)	Volume Occupancy	Substrate Occlusion
1	14.261	13.373	33.289	0.107	0.471	0.732
2	13.343	12.030	32.174	0.073	0.458	0.713
3	13.853	11.737	33.233	0.072	0.466	0.744
4	12.942	12.466	27.783	0.100	0.552	0.760
5	10.345	9.648	22.670	0.091	0.615	0.858
Avr	12.949	11.851	29.830	0.088	0.512	0.761

Appendix B – Dynamic structure results

Tables 7.19 – 7.36: Dynamic results for each individual simulation run. See Sections 4.5 – 4.8 for diagrams and discussion of these results. For all tables, structure height at 128 successful depositions given in Å, bond types listed as a fraction of total. Hydrogen bonding classes given according to the nomenclature of Figure 4.19, repeated here for convenience:

Type A: H@O, one hydrogen on the depositing molecule forms a bond with one oxygen in the structure

Type B: O@H, the oxygen on the depositing molecule forms a bond with one hydrogen in the structure

Type C: OH@HO, two H-bonds are formed by the depositing molecule, one on H and one on O

Type D: O@HH, the depositing oxygen forms two hydrogen-bonds while the hydrogen atoms are both ‘dangling’

Type E: HH@OO, both hydrogens form bonds with the structure while the oxygen is ‘dangling’

Type F: HOH@OHO, the depositing molecule forms three hydrogen bonds, one from each hydrogen and one from the oxygen

Type G: OH@HHO, the depositing molecule forms three hydrogen bonds, two from the oxygen and one from a hydrogen

<i>7.19: Dynamic Results for 10K deposition on 10K silica substrate</i>										
Run	Deposition Attempts	128 Height	Bonds A	Bonds B	Bonds C	Bonds D	Bonds E	Bonds F	Bonds G	Bonds Other
1	978	30.926	0.22	0.25	0.20	0.01	0.03	0.12	0.07	0.09
2	1225	11.036	0.19	0.17	0.32	0.06	0.05	0.09	0.08	0.03
3	1192	12.498	0.24	0.23	0.27	0.02	0.07	0.07	0.06	0.05
4	955	34.396	0.29	0.15	0.23	0.04	0.05	0.08	0.07	0.09
5	1108	12.740	0.23	0.22	0.27	0.05	0.04	0.05	0.05	0.09
Avr	1092	20.319	0.24	0.20	0.26	0.04	0.05	0.08	0.06	0.07

<i>7.20: Dynamic Results for 10K deposition on 10K water substrate</i>										
Run	Deposition Attempts	128 Height	Bonds A	Bonds B	Bonds C	Bonds D	Bonds E	Bonds F	Bonds G	Bonds Other
1	965	37.128	0.24	0.20	0.25	0.03	0.03	0.10	0.06	0.09
2	940	31.859	0.32	0.30	0.12	0.05	0.03	0.06	0.06	0.06
3	1055	12.287	0.27	0.25	0.21	0.05	0.03	0.09	0.04	0.05
4	1023	12.154	0.21	0.27	0.27	0.04	0.04	0.07	0.06	0.03
5	1012	15.139	0.27	0.22	0.26	0.03	0.05	0.08	0.05	0.03
Avr	999	21.713	0.26	0.25	0.22	0.04	0.04	0.08	0.06	0.05

<i>7.21: Dynamic Results for 10K deposition on 60K silica substrate</i>										
Run	Deposition Attempts	128 Height	Bonds A	Bonds B	Bonds C	Bonds D	Bonds E	Bonds F	Bonds G	Bonds Other
1	1078	11.629	0.26	0.23	0.24	0.05	0.04	0.06	0.05	0.08
2	1059	12.070	0.28	0.17	0.25	0.04	0.05	0.06	0.10	0.04
3	1130	11.457	0.20	0.29	0.26	0.04	0.07	0.07	0.04	0.04
4	1074	8.078	0.25	0.20	0.24	0.04	0.06	0.06	0.07	0.08
5	1102	10.139	0.28	0.23	0.25	0.04	0.06	0.05	0.05	0.03
Avr	1089	10.675	0.26	0.22	0.25	0.04	0.06	0.06	0.06	0.05

<i>7.22: Dynamic Results for 10K deposition on 60K water substrate</i>										
Run	Deposition Attempts	128 Height	Bonds A	Bonds B	Bonds C	Bonds D	Bonds E	Bonds F	Bonds G	Bonds Other
1	1022	10.544	0.21	0.25	0.24	0.05	0.04	0.10	0.04	0.06
2	1043	9.806	0.31	0.19	0.21	0.02	0.09	0.04	0.04	0.11
3	1098	8.771	0.27	0.21	0.30	0.02	0.03	0.07	0.07	0.03
4	949	21.697	0.27	0.29	0.26	0.02	0.02	0.06	0.04	0.04
5	1002	12.389	0.26	0.24	0.26	0.02	0.04	0.07	0.05	0.06
Avr	1023	12.641	0.26	0.23	0.25	0.03	0.04	0.07	0.05	0.06

<i>7.23: Dynamic Results for 10K deposition on 130K silica substrate</i>										
Run	Deposition Attempts	128 Height	Bonds A	Bonds B	Bonds C	Bonds D	Bonds E	Bonds F	Bonds G	Bonds Other
1	1134	11.353	0.23	0.23	0.27	0.03	0.06	0.05	0.06	0.05
2	1093	17.906	0.26	0.23	0.23	0.03	0.07	0.07	0.05	0.07
3	1079	8.915	0.26	0.20	0.23	0.05	0.06	0.08	0.05	0.07
4	1083	15.638	0.20	0.19	0.28	0.04	0.09	0.08	0.05	0.06
5	1115	10.651	0.25	0.18	0.28	0.02	0.08	0.08	0.04	0.07
Avr	1101	12.893	0.24	0.20	0.26	0.03	0.07	0.07	0.05	0.07

<i>7.24: Dynamic Results for 10K deposition on 130K water substrate</i>										
Run	Deposition Attempts	128 Height	Bonds A	Bonds B	Bonds C	Bonds D	Bonds E	Bonds F	Bonds G	Bonds Other
1	1028	11.901	0.23	0.20	0.25	0.03	0.08	0.09	0.06	0.06
2	1021	8.136	0.24	0.26	0.25	0.04	0.04	0.08	0.03	0.07
3	945	18.797	0.24	0.16	0.31	0.04	0.04	0.10	0.07	0.06
4	1000	12.238	0.30	0.15	0.27	0.03	0.05	0.10	0.04	0.05
5	995	13.981	0.27	0.19	0.27	0.04	0.05	0.09	0.03	0.06
Avr	998	13.011	0.26	0.19	0.27	0.04	0.05	0.09	0.05	0.06

<i>7.25: Dynamic Results for 150K deposition on 10K silica substrate</i>										
Run	Deposition Attempts	128 Height	Bonds A	Bonds B	Bonds C	Bonds D	Bonds E	Bonds F	Bonds G	Bonds Other
1	615	12.795	0.24	0.23	0.21	0.03	0.07	0.09	0.08	0.04
2	614	9.491	0.31	0.19	0.26	0.04	0.05	0.08	0.03	0.04
3	604	8.392	0.27	0.21	0.18	0.02	0.08	0.09	0.06	0.09
4	613	14.063	0.24	0.22	0.24	0.05	0.06	0.08	0.05	0.07
5	612	10.441	0.27	0.21	0.22	0.06	0.07	0.06	0.07	0.05
Avr	612	11.036	0.27	0.21	0.22	0.04	0.07	0.08	0.06	0.06

<i>7.26: Dynamic Results for 150K deposition on 10K water substrate</i>										
Run	Deposition Attempts	128 Height	Bonds A	Bonds B	Bonds C	Bonds D	Bonds E	Bonds F	Bonds G	Bonds Other
1	620	8.303	0.28	0.21	0.25	0.05	0.02	0.09	0.06	0.04
2	623	9.395	0.28	0.22	0.20	0.04	0.02	0.09	0.02	0.12
3	649	11.504	0.21	0.24	0.27	0.04	0.05	0.07	0.04	0.08
4	658	10.007	0.21	0.28	0.22	0.04	0.06	0.08	0.04	0.07
5	603	10.076	0.19	0.28	0.25	0.02	0.07	0.06	0.07	0.06
Avr	628	9.857	0.23	0.25	0.24	0.04	0.04	0.08	0.05	0.07

<i>7.27: Dynamic Results for 150K deposition on 60K silica substrate</i>										
Run	Deposition Attempts	128 Height	Bonds A	Bonds B	Bonds C	Bonds D	Bonds E	Bonds F	Bonds G	Bonds Other
1	596	11.384	0.20	0.17	0.30	0.02	0.06	0.07	0.09	0.08
2	619	11.887	0.24	0.20	0.25	0.05	0.04	0.09	0.08	0.06
3	629	8.915	0.25	0.23	0.24	0.04	0.03	0.09	0.06	0.07
4	607	11.708	0.16	0.28	0.27	0.03	0.05	0.10	0.05	0.05
5	602	10.994	0.27	0.15	0.30	0.04	0.05	0.07	0.07	0.04
Avr	611	10.978	0.23	0.21	0.27	0.03	0.05	0.08	0.07	0.06

<i>7.28: Dynamic Results for 150K deposition on 60K water substrate</i>										
Run	Deposition Attempts	128 Height	Bonds A	Bonds B	Bonds C	Bonds D	Bonds E	Bonds F	Bonds G	Bonds Other
1	644	7.255	0.22	0.25	0.23	0.03	0.03	0.12	0.07	0.06
2	630	7.438	0.30	0.12	0.30	0.00	0.07	0.07	0.07	0.06
3	625	6.637	0.25	0.27	0.20	0.03	0.07	0.09	0.04	0.05
4	641	7.311	0.31	0.14	0.24	0.04	0.06	0.13	0.05	0.05
5	629	6.906	0.24	0.28	0.23	0.01	0.04	0.09	0.05	0.06
Avr	634	7.109	0.26	0.21	0.24	0.02	0.05	0.10	0.05	0.06

<i>7.29: Dynamic Results for 150K deposition on 130K silica substrate</i>										
Run	Deposition Attempts	128 Height	Bonds A	Bonds B	Bonds C	Bonds D	Bonds E	Bonds F	Bonds G	Bonds Other
1	641	10.129	0.25	0.20	0.26	0.02	0.05	0.08	0.07	0.06
2	605	11.612	0.28	0.14	0.27	0.04	0.09	0.07	0.03	0.09
3	611	9.889	0.19	0.29	0.24	0.04	0.04	0.05	0.05	0.09
4	617	10.185	0.20	0.23	0.24	0.06	0.07	0.09	0.06	0.05
5	659	9.701	0.21	0.20	0.30	0.06	0.03	0.08	0.06	0.06
Avr	627	10.303	0.23	0.21	0.26	0.05	0.05	0.08	0.05	0.07

<i>7.30: Dynamic Results for 150K deposition on 130K water substrate</i>										
Run	Deposition Attempts	128 Height	Bonds A	Bonds B	Bonds C	Bonds D	Bonds E	Bonds F	Bonds G	Bonds Other
1	636	8.242	0.26	0.21	0.21	0.05	0.09	0.07	0.05	0.05
2	618	6.175	0.21	0.26	0.23	0.07	0.06	0.08	0.04	0.05
3	621	7.622	0.21	0.25	0.21	0.04	0.06	0.08	0.06	0.08
4	640	8.292	0.26	0.22	0.23	0.03	0.09	0.05	0.05	0.08
5	630	7.000	0.25	0.27	0.16	0.04	0.08	0.08	0.05	0.07
Avr	629	7.466	0.24	0.24	0.21	0.04	0.08	0.07	0.05	0.07

<i>7.31: Dynamic Results for 300K deposition on 10K silica substrate</i>										
Run	Deposition Attempts	128 Height	Bonds A	Bonds B	Bonds C	Bonds D	Bonds E	Bonds F	Bonds G	Bonds Other
1	588	9.586	0.23	0.25	0.26	0.02	0.05	0.06	0.05	0.07
2	604	8.860	0.22	0.22	0.25	0.04	0.06	0.08	0.06	0.08
3	560	6.556	0.22	0.22	0.25	0.04	0.06	0.08	0.06	0.08
4	568	11.784	0.23	0.28	0.24	0.06	0.04	0.05	0.04	0.05
5	574	10.069	0.25	0.23	0.22	0.03	0.06	0.09	0.06	0.07
Avr	579	9.371	0.23	0.24	0.25	0.04	0.05	0.07	0.06	0.07

<i>7.32: Dynamic Results for 300K deposition on 10K water substrate</i>										
Run	Deposition Attempts	128 Height	Bonds A	Bonds B	Bonds C	Bonds D	Bonds E	Bonds F	Bonds G	Bonds Other
1	590	8.068	0.25	0.22	0.20	0.03	0.06	0.10	0.04	0.10
2	581	8.630	0.19	0.27	0.26	0.04	0.08	0.06	0.05	0.04
3	579	6.288	0.30	0.22	0.22	0.02	0.05	0.09	0.05	0.06
4	574	7.912	0.24	0.21	0.27	0.04	0.06	0.06	0.04	0.09
5	590	7.610	0.27	0.23	0.22	0.03	0.08	0.09	0.04	0.06
Avr	583	7.702	0.25	0.23	0.23	0.03	0.06	0.08	0.04	0.07

7.33: Dynamic Results for 300K deposition on 60K silica substrate										
Run	Deposition Attempts	128 Height	Bonds A	Bonds B	Bonds C	Bonds D	Bonds E	Bonds F	Bonds G	Bonds Other
1	590	9.058	0.18	0.20	0.28	0.03	0.06	0.09	0.07	0.09
2	590	9.354	0.22	0.25	0.21	0.06	0.05	0.09	0.06	0.06
3	570	11.183	0.20	0.17	0.27	0.05	0.07	0.07	0.08	0.09
4	573	11.31	0.24	0.25	0.23	0.03	0.04	0.09	0.06	0.05
5	582	11.002	0.24	0.24	0.21	0.04	0.05	0.10	0.05	0.09
Avr	581	10.381	0.22	0.22	0.24	0.04	0.05	0.09	0.06	0.08

7.34: Dynamic Results for 300K deposition on 60K water substrate										
Run	Deposition Attempts	128 Height	Bonds A	Bonds B	Bonds C	Bonds D	Bonds E	Bonds F	Bonds G	Bonds Other
1	608	7.299	0.25	0.20	0.25	0.03	0.06	0.08	0.07	0.06
2	576	9.191	0.22	0.20	0.27	0.02	0.05	0.12	0.05	0.09
3	582	7.096	0.26	0.20	0.24	0.05	0.05	0.07	0.06	0.07
4	582	6.667	0.23	0.23	0.19	0.01	0.09	0.12	0.06	0.07
5	584	7.992	0.24	0.26	0.22	0.03	0.07	0.09	0.05	0.04
Avr	586	7.649	0.24	0.22	0.23	0.03	0.06	0.09	0.06	0.07

7.35: Dynamic Results for 300K deposition on 130K silica substrate										
Run	Deposition Attempts	128 Height	Bonds A	Bonds B	Bonds C	Bonds D	Bonds E	Bonds F	Bonds G	Bonds Other
1	569	12.629	0.28	0.23	0.19	0.04	0.08	0.07	0.06	0.04
2	587	10.824	0.18	0.24	0.27	0.02	0.05	0.10	0.07	0.08
3	580	11.241	0.23	0.21	0.27	0.03	0.07	0.10	0.05	0.04
4	587	9.749	0.24	0.23	0.22	0.04	0.06	0.09	0.07	0.06
5	595	8.951	0.24	0.23	0.23	0.03	0.07	0.08	0.04	0.07
Avr	584	10.679	0.23	0.23	0.24	0.03	0.07	0.09	0.06	0.06

7.36: Dynamic Results for 300K deposition on 130K water substrate										
Run	Deposition Attempts	128 Height	Bonds A	Bonds B	Bonds C	Bonds D	Bonds E	Bonds F	Bonds G	Bonds Other
1	592	7.880	0.23	0.28	0.19	0.04	0.04	0.08	0.07	0.07
2	609	6.449	0.21	0.25	0.25	0.04	0.09	0.06	0.04	0.06
3	593	7.139	0.23	0.22	0.24	0.05	0.05	0.10	0.05	0.06
4	593	6.488	0.23	0.23	0.25	0.04	0.06	0.10	0.07	0.03
5	604	7.419	0.25	0.22	0.23	0.05	0.08	0.05	0.06	0.06
Avr	598	7.075	0.23	0.24	0.23	0.04	0.06	0.08	0.06	0.06

